Photo and Electrochemical Investigations of Solution Processable Molecules and Materials for the Hydrogen Evolution Reaction

Danielle A. Henckel

A dissertation

submitted in partial fulfillment of the

requirements for the degree of

Doctor of Philosophy

University of Washington

2018

Reading Committee:

Brandi M. Cossairt, Chair

Daniel R. Gamelin

Cody W. Schlenker

Program Authorized to Offer Degree:

Chemistry

University of Washington

Abstract

Photo and Electrochemical Investigations of Solution Processable Molecules and Materials for the Hydrogen Evolution Reaction

Danielle A. Henckel

Chair of the Supervisory Committee:
Associate Professor Brandi M. Cossairt
Department of Chemistry

Sustainable hydrogen production photoelectrochemically or photocatalytically is a desirable process that has the potential to allow hydrogen to be utilized as a carbon free fuel. In order for this method to become commercially viable, scientific advances must be made on current technologies. Sustainable hydrogen production photocatalytically is projected to be more cost effective than hydrogen production photoelectrochemically, however significant scientific studies need to made and its future is uncertain. We envision a system of molecular electrocatalysts and colloidal photosensitizers for hydrogen production via photocatalysis. In Chapter 2, a library of molecular electrocatalysts are synthesized and their ability to perform hydrogen evolution electrocatalytically is explored. These molecules are found to be competent hydrogen evolution catalysts in nonaqueous solvents, albeit with high overpotentials. The parent metalloligand's ability to be a nucleophile toward a variety of cations lead us to study its interactions with CdSe in Chapter 3. In this Chapter, an electrochemical method for analyzing the equilibrium interactions between CdSe nanocrystals and small molecules is investigated. This technique

is demonstrated as a useful tool for analyzing catalyst-photosensitizer interactions which is an important qualification for understanding efficient photocatalysis. Preliminary data is shown to support oxidation state binding preference to CdSe nanocrystals for the molecules described in Chapter 3.

Non-precious metal hydrogen evolution catalysts that are durable and solution processable would help increase the cost effectiveness of photoelectrochemical hydrogen production. In Chapters 4 and 5, colloidally-synthesized WSe_2 in the 1T and 2H polytype forms respectively, are investigated as electrocatalysts for the hydrogen evolution reaction. In Chapter 4, in order to improve the activity of the 1T WSe_2, the effects of a ligand removing chemical agent, Meerwein's reagent, are investigated. In Chapter 5, the colloidally synthesized 2H WSe_2 is also investigated for the hydrogen evolution reaction. For this material, in addition to the ligand removal chemistry mentioned above, a facile electrochemical activation in aqueous conditions has been observed. This activation step increases the activity to be on par to the 1T WSe_2 discussed in Chapter 4.

Table of Contents

List of Figures

List of Schemes

List of Tables

Acknowledgments

To my family.

To my friends.

To the Cossairt lab community and to Brandi.

A special thanks to-

David Ung for his amazing echem knowledge and support,

Dr. Olivia Lenz for being an outstanding friend and without her work half of the thesis would not be possible,

Dr. Mike Norris and Dr. Ben Glassy for being an outstanding role models, and to

my two undergraduates for their hard-work and dedication- Noush Panahpour Eslami and Yuting Lin.

CHAPTER 1. INTRODUCTION TO UTILIZING ELECTROCHEMISTRY FOR THE BENCHMARKING OF SYSTEMS RELEVANT TO SUSTAINABLE HYDROGEN PRODUCTION

1.1. Motivation for photoelectrochemical and photocatalytic hydrogen production

Hydrogen is an energy-dense molecule with the potential to be used as a widespread carbon-free fuel source. The renewable production of hydrogen via photoelectrochemical splitting is a promising option (Figure 1.1).[1-4] By producing hydrogen via sunlight, we are able to transform solar energy into chemical energy. This chemical energy can then be released through combustion or through use in a fuel cell and converted into electrical energy. In this way hydrogen can be used as a storage device for solar energy to electrical energy conversion.

Studying all or parts of the photoelectrochemical production of hydrogen scheme is useful, not only for generation of hydrogen, but also for further expansion into other, more complicated systems in an attempt to promote green chemistry practices into other chemical syntheses. Hydrogen gas is also a major chemical commodity in industry. For example, hydrogen is used on a massive scale in the production of ammonia, methanol and in petroleum refining.[3] Currently, hydrogen production is currently dominated by steam reforming methane, producing 1 molecule of CO_2 for every four molecules of H_2 in the process.[5] An alternative, clean synthesis of hydrogen can involve the electrolysis of water using catalysts and photosensitizers made of earth-abundant materials by scalable syntheses.

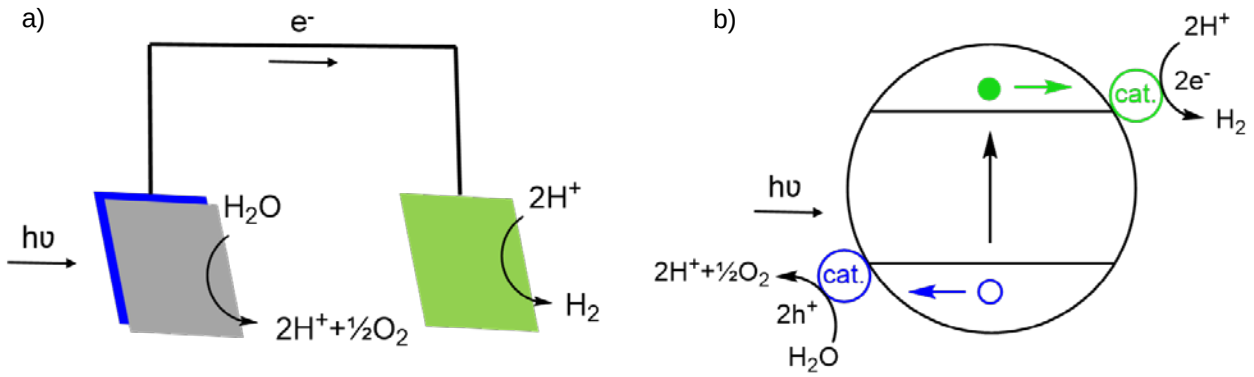

Figure 1.1. a) Water splitting on a photoanode and cathode surfaces deposited with catalysts b) Water splitting on a colloidal system involving soluble photosensitizers and catalysts

The economic viability of the different modules show in Figure 1.1 have been explored.[6-7] The first module (Figure 1.1a) depicts the water splitting process on photoanodes and photocathodes deposited with catalysts. The second module (Figure 1.1b) depicts a particle suspension that contains photosensitizers and catalysts that perform each half of the water splitting reaction. Depending on the exact configurations, the photoelectrochemical system would have a levelized cost of $4.10-$10.40 per kg H_2 and the photocatalytic system involving a particle suspension would have a levelized cost of $1.60-$3.20, per kg H_2.[6] While the photocatalytic model has the potential to be more cost effective, its technology is more uncertain and is farther from commercialization.

The problems addressed in this thesis involve the development of non-platinum group heterogeneous and homogenous electrocatalysts as well as the interactions of small molecules with a nanocrystal photosensitizer. All of these studies were performed to further the development of either module for sustainable hydrogen generation. In order to study the effectiveness of different electrocatalysts, proper benchmarking is necessary and will be discussed in this introduction chapter.

The basis of electrochemical techniques is to apply a potential and measure the resulting current. This can be done on different time scales by varying the rate at which the potential is changed (scan rate in linear sweep/cyclic voltammetry) or by varying the frequency at which the potential is applied in electrochemical impedance spectroscopy (EIS). The current response of the cyclic voltammogram (CV) or the linear sweep voltammogram (LSV) can be analyzed in a variety of ways to determine the overpotential and rates for electrocatalytic reactions.

1.2. Electrochemistry for benchmarking catalysts

1.2.1. Background of the Tafel slope and exchange current density

Electrochemical processes are usually analyzed using Butler-Volmer kinetics, which describes electrochemical rate in terms of potential. The Butler-Volmer expression originates from the Arrhenius equation, transition state theory and the Tafel equation.

$$\eta = a + b\ log i \qquad \text{Equation 1.1}$$

The Tafel equation, determined experimentally, (Equation 1.1) simply states that electrochemical reaction rate, measured by the current (i), has a logarithmic dependence on potential (η).[8-9] The slope of this equation, b, called the Tafel slope, is a measure of how much potential must be applied for the reaction rate (current) to increase x10. This value is used in much of the hydrogen evolution reaction literature on heterogeneous reactions to compare how efficient catalysts are. While the Tafel slope value can be a manifestation of the internal resistance of an electrode-catalyst system,[10] it is also correlated with rate-determining steps, with 120 mV/dec, 40 mV/dec and 30 mV/dec corresponding to a rate-determining step of Volmer, Heyrovsky and Tafel respectively (Figure 1.2).[11] These are the limits for the Tafel slope when operating according to these mechanisms and we do not expect any lower values.

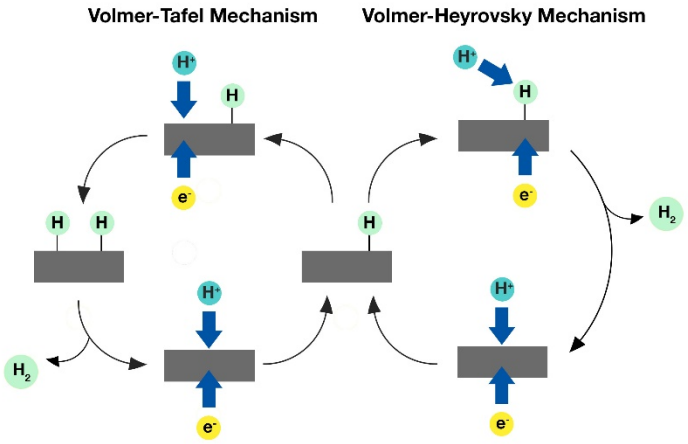

Figure 1.2. Possible mechanisms for H_2 generation involving first the Volmer step where a hydrogen atom is adsorbed (H_{ads}) onto the electrode surface and either 1) the Volmer-Tafel mechanism where two H_{ads} react, or 2) the Volmer-Heyrovsky mechanism where the H_{ads} reacts with a H^+ in solution with the extra electron provided by the electrode

We turn to transition state theory in order to describe how potential is related to the driving force (Gibbs free energy) of a reaction.[12] Figure 1.3 shows potential surfaces of products and reactants in a chemical reaction as a function of reaction coordinate and Gibbs free energy. Upon application of a reducing potential, the reactants' potential surface is destabilized, thus the transition to products becomes more favorable. This reactants' potential surface is changed until the driving force for the reaction (and possibly wasted energy in the form of an overpotential) is compensated for and the reactants can proceed to the products. The Gibbs free energy of activation when a potential is applied, $\overline{G_{act}}$, is changed proportionally to the magnitude of the potential. Equation 1.2 and Equation 1.3 describe the anodic and cathodic barriers respectively.

$$\overline{G_{act}} = \Delta G_{act} + \alpha F \Delta E_{act} \qquad \text{Equation 1.2}$$

$$\overline{G_{act}} = \Delta G_{act} - (1-\alpha) F \Delta E_{act} \qquad \text{Equation 1.3}$$

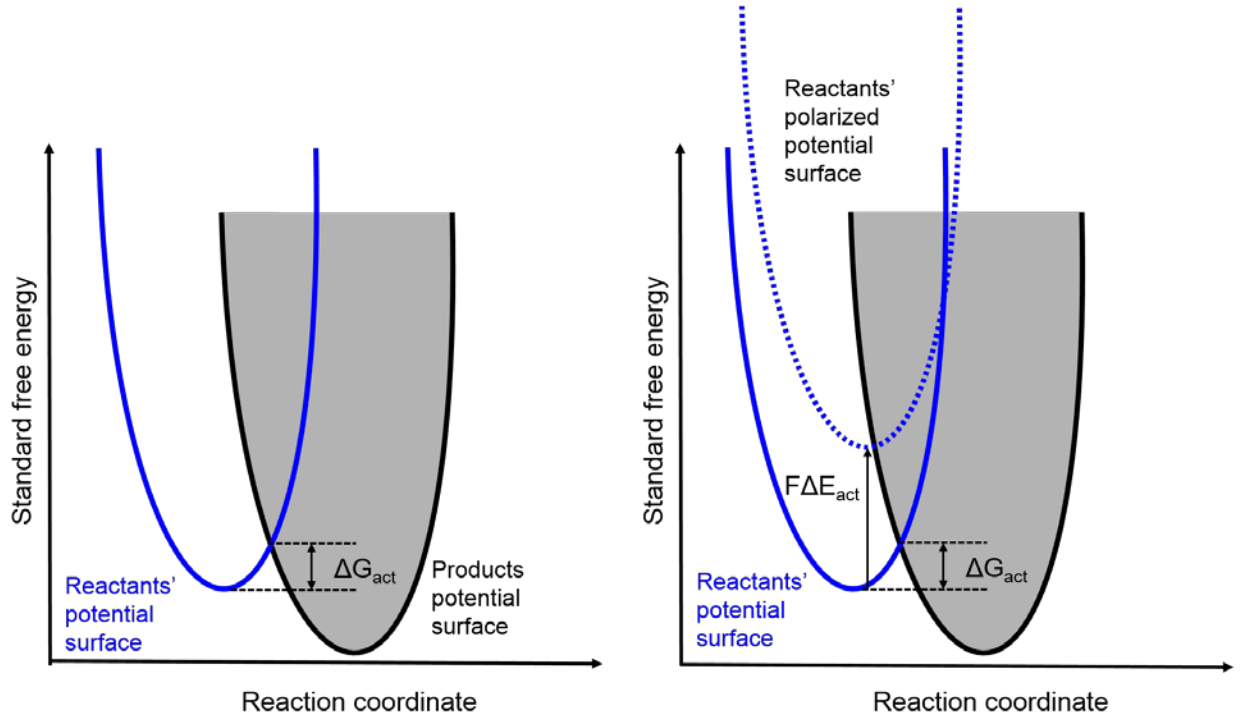

Figure 1.3. Transition state theory applied to electrochemical reactions illustrating the effect an applied potential has on the free energy of reactants

The Arrhenius equation relates the reaction rate, k, with activation free energy (Equation 1.4). Now we can provide rates for reactions based on the ΔG_{act}. Substituting in Equation 1.2 into Equation 1.4, we obtain Equation 1.5 where we now have related the rate of reaction to ΔG_{act}. Also accounting for anodic reactions we obtain Equation 1.6 (assuming a reduction reaction, where cathodic current will contribute to k_f (forward rate constant) and anodic current will contribute to k_b (backward rate constant)).

$$k = Aexp(-\frac{\Delta\overline{G_{act}}}{RT}) \qquad \text{Equation 1.4}$$

$$k_f = Aexp(-\frac{\Delta G_{act}+\alpha F\Delta E_{act}}{RT}) \qquad \text{Equation 1.5}$$

$$k_b = Aexp(-\frac{\Delta G_{act}+(1-\alpha)F\Delta E_{act}}{RT}) \qquad \text{Equation 1.6}$$

Reaction rate is directly proportional to the measured current. This is described by Equation 1.7 relating i- the current (A), r- reaction rate (or the rate at which electrons are leaving or entering the

electrode(s^{-1})), A- the electrode area (cm^2), F- Faraday's constant (C/mol), and n- the number of electrons.

$$i = nFAr \qquad \text{Equation 1.7}$$

Reaction rate, r can be written in terms of k_f and k_b (at equilibrium such that the concentration at the electrode surface of the oxidized and reduced products are equal)

$$r = k_f + k_b \qquad \text{Equation 1.8}$$

Now we combine equations 1.5, 1.6 and 1.7 to obtain Equation 1.9. Specifically we have chosen a situation when mass transport will not be a concern (at low overpotentials at the onset of reaction so that the concentration of the reactants and products do not need to be taken into account as they are not limiting).

$$i = FAk^0 \left[exp(-\frac{F\alpha(\Delta \text{Eact})}{RT})\text{-}exp(\frac{F(1-\alpha)(\Delta \text{Eact})}{RT})\right] \qquad \text{Equation 1.9}$$

In Equation 1.9 we have accessed a current potential relationship. This expression gives us a complete current potential relation. Our standard rate constant, k^0, also known as the intrinsic rate constant, is a measure of how facile the reaction of interest occurs.

1.2.2. Measuring rates of heterogeneous electrocatalysts

We can describe the rates of heterogeneous electrocatalysts by converting k^0 into i_0, the exchange current density, by utilizing Equation 1.10. Assuming the solution does not suffer from mass transfer effects, we can arrive at our final Butler-Volmer relation in Equation 1.11 ($\Delta E_{act.}=\eta$ and $f = F/RT$). We can obtain i_0 through the Tafel plot, wherein we plot potential versus log(i), Graphing only the linear portion of this slope, we can extrapolate to zero as seen in Figure 1.4.

$$i_0 = FAk^0C \qquad \text{Equation 1.10}$$

$$i = i_0\left[e^{-\alpha f \eta} - e^{(1-\alpha f \eta)}\right] \qquad \text{Equation 1.11}$$

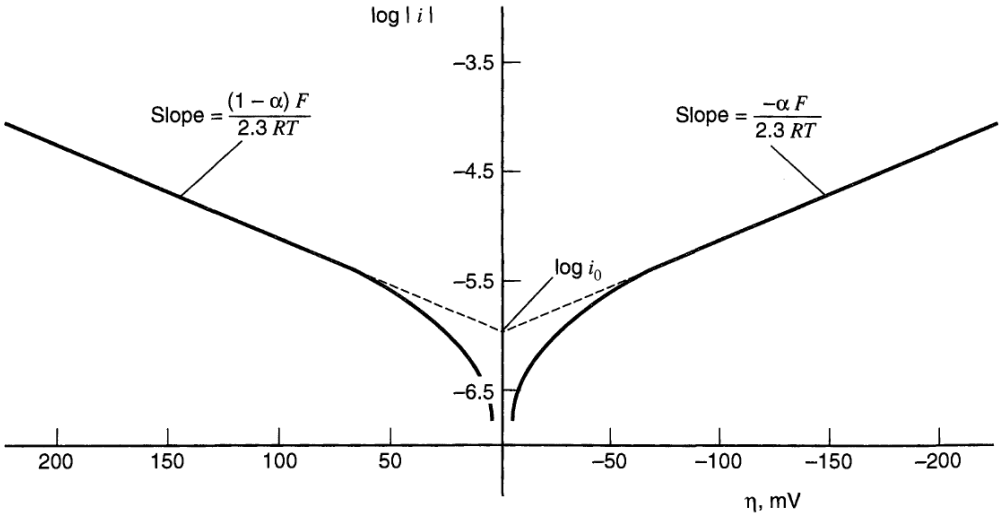

Figure 1.4. Tafel plots and exchange current density from current vs overpotential curves of an anodic and cathodic reaction. Source: Bard, A. J.; Faulkner, L. R.; Leddy, J.; Zoski, C. G., *Electrochemical methods: fundamentals and applications*. Wiley New York: 1980; Vol. 2.

In order to obtain a measure of rate per active site, the capacitance of the electrode (mF) is divided by the i_0 in order to benchmark heterogeneous catalysts. This value is an overestimate of rate as it takes into account all surface area and not just the active sites. More rigorous analysis of active sites can be performed in order to further correct for this value.[13]

Referencing back to Figure 1.1, we understand that the applied potential directly influences the ΔG_{act} and therefore the catalytic reaction to proceed. The major descriptor for overpotential and thereby rate, has been theorized to be the ΔG_H, which is the free energy of the H_{ads} intermediate. This is shown graphically in the volcano plot in Figure 1.4. According to this theory, if H_{ads} binds too weakly or too strongly, then the intrinsic catalytic activity, described here as j_0, will decrease. A thermoneutral ΔG_H will afford the most active catalysts and is thought to be why platinum and platinum group metals are the most active known hydrogen evolution catalysts at low overpotentials.[14]

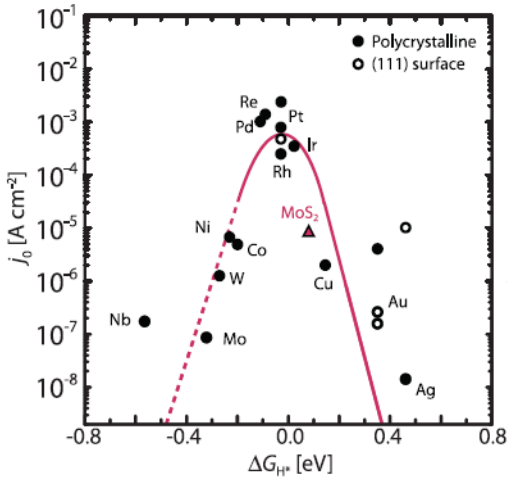

Figure 1.5. Volcano plot for metals and MoS_2. Source: Seh, Z. W.; Kibsgaard, J.; Dickens, C. F.; Chorkendorff, I.; Nørskov, J. K.; Jaramillo, T. F., Combining theory and experiment in electrocatalysis: Insights into materials design. *Science* **2017,** *355* (6321).

1.2.3. Measuring rates of homogenous electrocatalysts

As opposed to heterogeneous catalysts, where we can simply increase the driving force by changing the potential, molecular systems have well-defined active catalytic states that can be described as either on or off. In order to measure rates of molecular electrocatalysts, the mechanism for the specific system should be analyzed and then the appropriate electrochemical rate equation can be applied.[15-16] To eliminate the complications of diffusion, in some instances a scan rate independent regime can be accessed and thus the current response will be a plateau governed only by kinetics. From this plateau current and with knowledge of the mechanisms the appropriate equation can be applied.

Since stability can be an issue with molecular electrocatalysts and a high concentration of acid may be necessary to reach non-diffusion limited zones, a ratio of the catalytic current to the diffusion controlled redox couple, i_{cat}/i_p, can be used as a simple way to benchmark these catalysts. This method internally accounts for the diffusion coefficient, electrode area and concentration of catalyst.[16] The i_{cat}/i_p is proportional to the k_{obs} and can be used to make relative comparisons of catalytic activity.

1.2.4. Measuring overpotentials of heterogeneous electrocatalysts

In addition to rates, measurement of overpotentials are necessary to determine catalyst ability. The overpotential describes how much extra energy is needed to be put in a system, beyond that necessary for thermodynamics, for the reaction to proceed. Since the oxidation of hydrogen and the reduction of protons occurs on platinum at equilibrium, this is used as a reference for zero overpotential. Generally, a system specific reference is utilized where, under the experiment's specific solvent, the potential of a platinum electrode under saturated H_2 is used as zero overpotential. This reference system is referred to as the RHE (reference hydrogen electrode). In order to benchmark against other catalysts, the overpotential is taken at the current density, -10mA/cm^2. This particular value is chosen due to the fact this is a reasonable current density an integrated solar to fuel cell would draw from a 10% efficient photovoltaic. [17]

1.2.5. Measuring overpotentials of homogenous electrocatalysts

The potential at which overpotential is measured for molecular electrocatalysts is taken as the $E_{cat/2}$, or the halfway point in to maximum current in a catalytic wave. Referencing in nonaqueous systems can be challenging as the thermodynamics are based on acid strength, or the acid dissociation constant, in the specific solvent of choice and can be complicated with homoconjugation effects of acids. However, an experimental method to measure exact $E^0(H^+/H_2)$ for nonaqueous systems has been developed using an open circuit potential method.[18]

1.2.6. Important considerations

Experiment design is crucial in order to prevent contamination in both systems. In molecular electrocatalysis, electrode fouling from acid sources and silver contamination from the reference electrode are concerns.[15, 19] Furthermore, homogenous catalyst often degrade under HER conditions, so it is necessary to test for stability of the catalyst and especially ensure that nanoparticles formation is not convoluting catalytic results.[20] For heterogeneous systems, platinum leaching in aqueous acidic electrolyte can result in deposition of platinum on the catalyst of interest. This effect of platinum

deposition can be measured by electrochemistry under the detection limit of platinum by typical analytic measurements.[21] Other important consideration when benchmarking catalysts is their long-term stability and this can be studied through extended electrolysis.[17]

1.3. Outlook

Electrochemistry is a powerful tool that can be used to benchmark both heterogeneous and homogeneous electrocatalysts. In both systems, we can determine the rate of reaction through proper analysis. The overpotential for both systems can be measured in a facile manner simply by a single CV or LSV trace and knowledge of thermodynamic potentials for the H^+/H_2 couple in question.

Design of molecular electrocatalysts for hydrogen evolution require that attention is chosen to redox potentials. The target oxidation state, generally a very low oxidation state, must be more reductive than the thermodynamic potential of the H^+/H_2 couple of the particular acid in use. If this is not the case, then the molecule, if active, must be further reduced and this will necessarily increase the overpotentials. Also, this reduced state must be basic enough for its protonation by the acid source.[22]

For heterogeneous electrocatalysts, the current the design principles for increasing intrinsic activity are based on designing systems with a thermoneutral ΔG_H. This is proposed through a variety of strategies such as confinement of active sites, promoting adsorbates, synthesis of alloyed and core-shell materials and intercalation.[23]

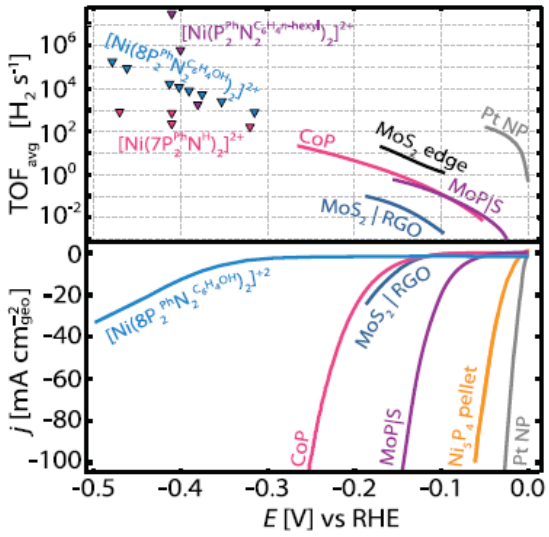

Figure 1.6. Benchmarking the best heterogeneous and homogeneous electrocatalysts. Source: Seh, Z. W.; Kibsgaard, J.; Dickens, C. F.; Chorkendorff, I.; Nørskov, J. K.; Jaramillo, T. F., Combining theory and experiment in electrocatalysis: Insights into materials design. Science 2017, 355 (6321).

There are advantages and disadvantages to each system. Among the disadvantages of molecular catalysts is diffusion, which increases reaction times, although their use in an integrated system would result in an overall decreased cost as mentioned above. Heterogeneous catalysts currently offer greater stability but are limited by scaling relations.[23-24] Unique solutions to overcome scaling relations will be necessary to find an earth abundant substitute for platinum. Homogenous system are more active per turnover site, however at greater overpotenials than heterogeneous catalysts (Figure 1.6).[23] Homogenous systems allow for the careful study of factors that may break scaling relations such as second coordination sphere effects and proton relays. Together, the two fields of homogenous and heterogeneous electrocatalysis can each offer unique advantages toward the goal of sustainable photoelectrochemical or photocatalytic hydrogen production.

1.4. References

1. Han, Z.; Qiu, F.; Eisenberg, R.; Holland, P. L.; Krauss, T. D., Robust Photogeneration of H2 in Water Using Semiconductor Nanocrystals and a Nickel Catalyst. *Science* **2012,** *338* (6112), 1321-1324.
2. Teets, T. S.; Nocera, D. G., Photocatalytic hydrogen production. *Chemical Communications* **2011,** *47* (33), 9268-9274.
3. Kothari, R.; Buddhi, D.; Sawhney, R. L., Comparison of environmental and economic aspects of various hydrogen production methods. *Renewable and Sustainable Energy Reviews* **2008,** *12* (2), 553-563.
4. Bard, A. J.; Fox, M. A., Artificial Photosynthesis: Solar Splitting of Water to Hydrogen and Oxygen. *Accounts of Chemical Research* **1995,** *28* (3), 141-145.
5. Udengaard, N. R., Hydrogen production by steam reforming of hydrocarbons. *Preprint Papers–American Chemical Society, Division of Fuel Chemistry* **2004,** *49* (2), 906-907.
6. Pinaud, B. A.; Benck, J. D.; Seitz, L. C.; Forman, A. J.; Chen, Z.; Deutsch, T. G.; James, B. D.; Baum, K. N.; Baum, G. N.; Ardo, S., Technical and economic feasibility of centralized facilities for solar hydrogen production via photocatalysis and photoelectrochemistry. *Energy & Environmental Science* **2013,** *6* (7), 1983-2002.
7. James, B. D.; Baum, G. N.; Perez, J.; Baum, K. N., Technoeconomic analysis of photoelectrochemical (PEC) hydrogen production. *DOE report* **2009**.
8. Tafel, J., Über die Polarisation bei kathodischer Wasserstoffentwicklung. *Zeitschrift für physikalische Chemie* **1905,** *50* (1), 641-712.
9. Fang, Y.-H.; Liu, Z.-P., Tafel kinetics of electrocatalytic reactions: from experiment to first-principles. *ACS Catalysis* **2014,** *4* (12), 4364-4376.
10. Vrubel, H.; Moehl, T.; Gratzel, M.; Hu, X., Revealing and accelerating slow electron transport in amorphous molybdenum sulphide particles for hydrogen evolution reaction. *Chemical Communications* **2013,** *49* (79), 8985-8987.
11. Shinagawa, T.; Garcia-Esparza, A. T.; Takanabe, K., Insight on Tafel slopes from a microkinetic analysis of aqueous electrocatalysis for energy conversion. *Scientific Reports* **2015,** *5*, 13801.
12. Bard, A. J.; Faulkner, L. R.; Leddy, J.; Zoski, C. G., *Electrochemical methods: fundamentals and applications*. wiley New York: 1980; Vol. 2.
13. Jaramillo, T. F.; Jørgensen, K. P.; Bonde, J.; Nielsen, J. H.; Horch, S.; Chorkendorff, I., Identification of active edge sites for electrochemical H2 evolution from MoS2 nanocatalysts. *Science* **2007,** *317* (5834), 100-102.
14. Tsai, C.; Chan, K.; Abild-Pedersen, F.; Norskov, J. K., Active edge sites in $MoSe_2$ and WSe_2 catalysts for the hydrogen evolution reaction: a density functional study. *Physical Chemistry Chemical Physics* **2014,** *16* (26), 13156-13164.
15. Rountree, E. S.; McCarthy, B. D.; Eisenhart, T. T.; Dempsey, J. L., Evaluation of Homogeneous Electrocatalysts by Cyclic Voltammetry. *Inorganic Chemistry* **2014,** *53* (19), 9983-10002.
16. Lee, K. J.; Elgrishi, N.; Kandemir, B.; Dempsey, J. L., Electrochemical and spectroscopic methods for evaluating molecular electrocatalysts. *Nature Reviews Chemistry* **2017,** *1* (5), 0039.
17. McCrory, C. C. L.; Jung, S.; Ferrer, I. M.; Chatman, S. M.; Peters, J. C.; Jaramillo, T. F., Benchmarking Hydrogen Evolving Reaction and Oxygen Evolving Reaction Electrocatalysts for Solar Water Splitting Devices. *Journal of the American Chemical Society* **2015,** *137* (13), 4347-4357.
18. Appel, A. M.; Helm, M. L., Determining the Overpotential for a Molecular Electrocatalyst. *ACS Catalysis* **2014,** *4* (2), 630-633.
19. McCarthy, B. D.; Martin, D. J.; Rountree, E. S.; Ullman, A. C.; Dempsey, J. L., Electrochemical Reduction of Brønsted Acids by Glassy Carbon in Acetonitrile- Implications for Electrocatalytic Hydrogen Evolution. *Inorganic chemistry* **2014,** *53* (16), 8350-8361.
20. Artero, V.; Fontecave, M., Solar fuels generation and molecular systems: is it homogeneous or heterogeneous catalysis? *Chemical Society Reviews* **2013,** *42* (6), 2338-2356.
21. Dong, G.; Fang, M.; Wang, H.; Yip, S.; Cheung, H.-Y.; Wang, F.; Wong, C.-Y.; Chu, S. T.; Ho, J. C., Insight into the electrochemical activation of carbon-based cathodes for hydrogen evolution reaction. *Journal of Materials Chemistry A* **2015,** *3* (24), 13080-13086.

22. Marinescu, S. C.; Winkler, J. R.; Gray, H. B., Molecular mechanisms of cobalt-catalyzed hydrogen evolution. *Proceedings of the National Academy of Sciences* **2012,** *109* (38), 15127-15131.
23. Seh, Z. W.; Kibsgaard, J.; Dickens, C. F.; Chorkendorff, I.; Nørskov, J. K.; Jaramillo, T. F., Combining theory and experiment in electrocatalysis: Insights into materials design. *Science* **2017,** *355* (6321), eaad4998.
24. Viswanathan, V.; Hansen, H. A.; Rossmeisl, J.; Nørskov, J. K., Universality in oxygen reduction electrocatalysis on metal surfaces. *ACS Catalysis* **2012,** *2* (8), 1654-1660.

CHAPTER 2. SYNTHESIS AND CHARACTERIZATION OF A COBALT DIIMINE DIOXIMATE METALLOLIGAND AND ITS MULTIMETALLIC DERIVATIVES AND THEIR USE AS PROTON REDUCTION CATALYSTS

Significant portions of the following have been previously published[1]

2.1. Introduction

The investigation of bimetallic complexes for catalytic applications has been driven by the ability of a second metal center to tune the properties of the primary catalyst.[2-5] The synthesis of bimetallic complexes, however, can be challenging owing to difficulties in ligand synthesis and site-specific metalation. A versatile monometallic precursor for the synthesis of bimetallic complexes would be useful in the synthesis and subsequent studies of the effects of the bimetallic motif on the reactivity of the resulting complexes.

A diverse family of metal diimine monoxime monoximate[6-8] and diglyoxime[9-16] complexes have been studied for use as proton reduction catalysts. The synthesis of bimetallic diimine monoxime monoximate complexes has been previously explored through *in situ* deprotonation of the oxime proton (Scheme 2.1).[17-20] This strategy has provided access to a variety of bimetallic complexes; however this strategy requires a unique set of conditions for each metal and therefore is not broadly generalizable.

We became interested in the idea of preparing an isolable, doubly deprotonated diimine dioximate complex to serve as a versatile ligand for the construction of multimetallic catalysts. Reports on the structure of a parent diimine monoxime monoximate cobalt complex containing an ethylene backbone have shown a long O-O interatomic distance, suggesting that no hydrogen bond exists between the two *cis*-oxime oxygens.[21] We have found that this proton is removed by addition of an imidazole base and the resulting *cis* doubly deprotonated dioximate species can be easily isolated.

An isolable metalloligand was also desirable in order to study binding interactions of the cobalt catalyst through cation binding sites on photosensitizers in a facile way. To this end we have investigated the binding of metal cations to this complex as a model system. We have found that the interactions and equilibrium of binding into the pocket of this metalloligand can be studied via a wide variety of different characterization methods such as ^{1}H NMR, electrochemistry and UV-vis spectroscopy. Later in the chapter, the electrochemical proton reduction catalyzed by these complexes will be explored.

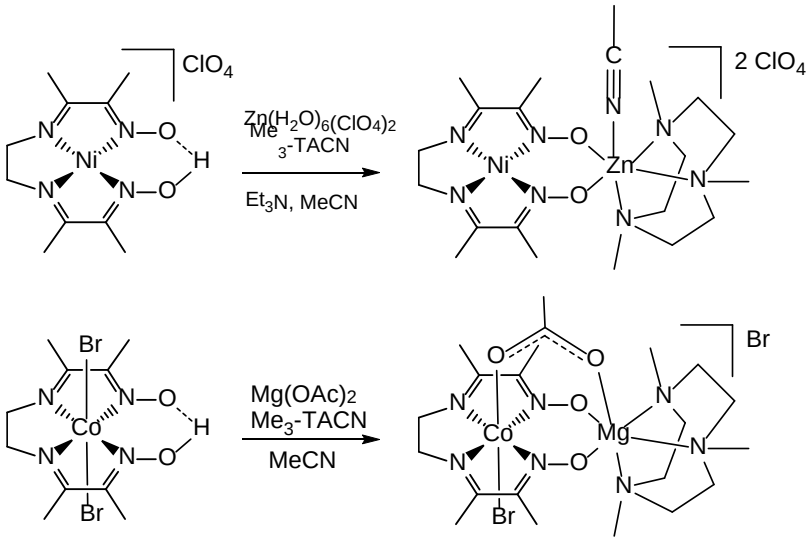

Scheme 2.1. Examples of bimetallic complexes synthesized via the *in situ* deprotonation of the oxime proton[18-19]

2.2. Results and discussion

2.2.1. Synthesis of cobalt diimine dioximate and bimetallic and tetrametallic derivatives

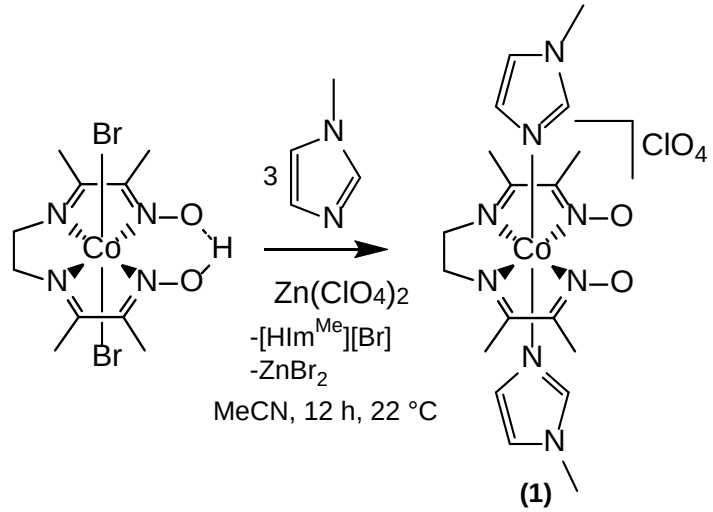

Scheme 2.2. Synthesis of complex 1, $[(DO)_2en(Im^{Me})_2Co]^+$

The doubly deprotonated cobalt(III) diimine dioximate cation ligated by two axial 1-methylimidazole groups, $[(DO)_2en(^{Im}Me)_2Co]^+$ (complex 1), is synthesized as the perchlorate salt by addition of excess 1-methyl imidazole and one equivalent of zinc perchlorate to the cobalt(III) diimine monooxime monooximate starting material, $(DO)(DOH)enCoBr_2$, in CH_3CN (Scheme 2.2). After stirring overnight, a golden solid precipitates out of the red-brown solution. The choice of zinc perchlorate is advantageous since the resulting zinc bromide and any zinc containing byproducts are very soluble in CH_3CN allowing

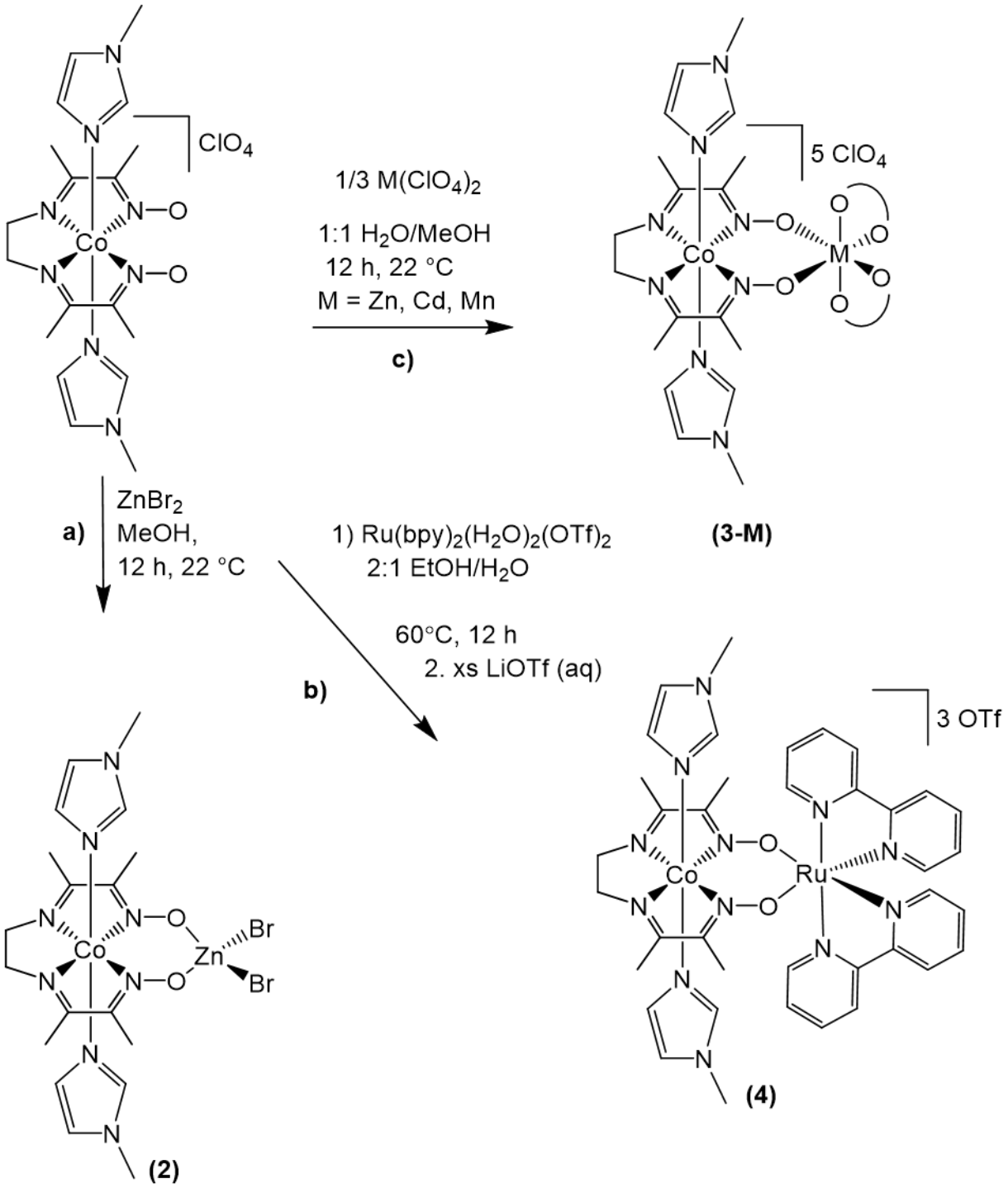

Scheme 2.3: Synthesis of bimetallic and tetrametallic complexes

for clean precipitation of 1 from solution. Complex 1 can be isolated using other counter anions, however care must be taken to avoid the use of unsequestered alkali metal salts for the anion exchange, as sodium binds readily in the O-O binding pocket. This is evidenced by our isolation of $[(DO)_2en(Im^{Me})_2CoNa][PF_6]_2$

and $[(DO)_2en(Im^{Me})_2CoNa\text{-}15crown5][BPh_4]_2$ (see Experimental Figure 2.9). Alternatively, no addition of a perchlorate salt will result in the bromide salt following the same conditions.

As anticipated, addition of zinc dibromide to 1 in methanol affords bimetallic $(DO)_2en(Im^{Me})_2CoZnBr_2$ (complex 2) after stirring overnight (Scheme 2.3a). Utilizing water as a solvent or co-solvent in this synthesis affords the tetrametallic species, $[((DO)_2en(Im^{Me})_2Co)_3Zn]^{5+}$ (complex 3-Zn) seen in Scheme 2.3c. Therefore, the stoichiometry in the CoZn system can be controlled by solvent choice. We have synthesized and characterized the tetrametallic species 3-M, M= Zn, Cd, Mn, from their corresponding perchlorate salts in 1:1 water/methanol with three equivalents of 1.

Attempts to synthesize the bimetallic manganese and cadmium complexes from their bromide salts were unsuccessful, leading to isolation of solely complexes 3-Mn and 3-Cd and excess MBr_2. To this end, we sought an alternate way to access bimetallic species using 1. We hypothesized that utilizing more strongly complexed starting materials with two *cis* open coordination sites, as in the case of $[Ru(bpy)_2(H_2O)_2]^{2+}$, would lead to facile formation of bimetallic complexes. Upon addition of complex 1 to $Ru(bpy)_2(H_2O)_2(OTf)_2$, in 2:1 ethanol/water overnight at 60 °C, $[(DO)_2en(Im^{Me})_2Co)Ru(bpy)_2]^{3+}$ (complex 4) crystallizes cleanly after addition of excess LiOTf (Scheme 2.3b).

In order to make structural and spectral comparisons to 1, as well as to perform pK_a studies, $[(DOH)(DO)en(Im^{Me})_2Co)]^+$ (complex 1-H^+), was independently synthesized from 1 by addition of [HDMF][OTf] in CH_3CN and subsequent crystallization from water with excess $NaPF_6$.

Complex 2 can be reduced from the starting Co(III) oxidation state to both Co(II) and Co(I) with $(C_6H_6)_2Cr$ (Scheme 2.4). This is achieved by controlling the stoichiometry of the reductant. Reacting complex 2 with stoichiometric $(C_6H_6)_2Cr$, the Co(II) oxidation state can be accessed. In the presence of a 10-fold excess of the reductant, the Co(I) oxidation state is isolated. According to the redox potentials of the $(C_6H_6)_2Cr$ reagent, it is not reducing enough at -1.22 vs $Fc^{0/+}$. However, the redox potential of the mono-imidazole version of complex 2 is significantly more oxidizing by ~0.480mV and capable of being reduced by $(C_6H_6)_2Cr$. In order the push the equilibrium toward Co(I), the concentration of $(C_6H_6)_2Cr$ is simply increased x10.

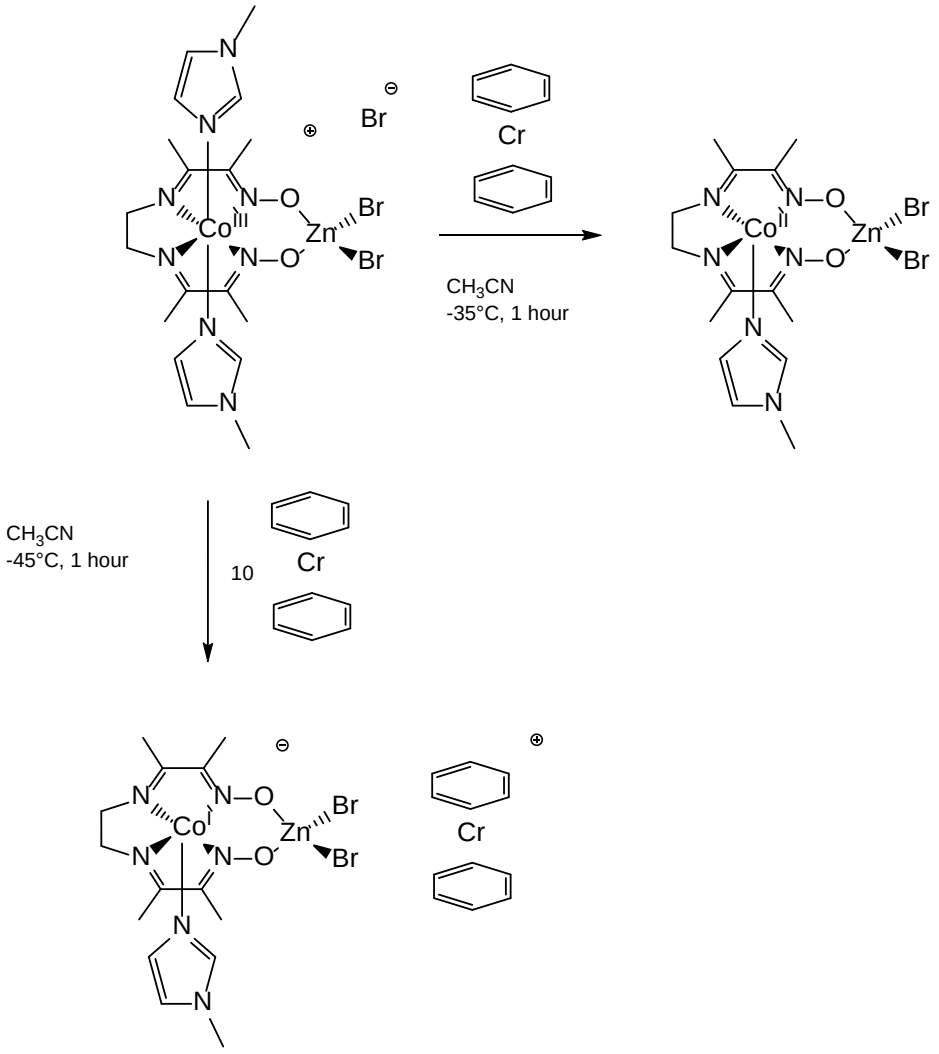

Scheme 2.4. Reduction of complex 2

2.2.2. X-ray Crystal Structures of Cobalt Diimine Dioximate and Derivatives

Complexes 1, 1-H$^+$, 2, 3-M (M= Mn, Cd, Zn), and 4 were all characterized by single crystal X-ray diffraction (Figure 2.1).[22] From the solid-state structures, the O-O interatomic distance gives further evidence for the lack of a bridging proton in 1 (3.128(4) Å vs 2.564(1) Å in 1-H$^+$). A demonstration of the flexibility of 1 as a metalloligand is provided by the O-O interatomic distances from the crystal structures, with this distance varying by almost 0.7 Å among the complexes studied here (Table 2.1). In the bimetallic species, the O-O interatomic distance lengthens to accommodate the coordinated Zn and Ru with distances of 3.197(3) and 3.24(1) Å, respectively, with the latter having the largest O-O interatomic distance observed

in this study. This compares to the smaller O-O interatomic distance of 3.122 Å for a similar CoMg complex previously studied using the same ethylene bridged diimine dioximate ligand framework on cobalt.[19] The O-O interatomic distances of the tetrametallic complexes correlate well with their atomic radii, in the order Cd>Mn>Zn with distances of 3.203(4), 3.071(3) and 3.061(4) Å respectively.

The single crystal X-ray structures of the Co(II) and Co(I) oxidation states of complex 2 can be seen in Figure 2.2. From the X-ray structures we can deduce that upon reduction of the complex, a 1-methyl imidazole ligand is no longer complexed in the solid state. This is due to electron occupation of a dz^2 orbital in this pseudo-octahedral geometry placing electron density in this orbital, thereby decreasing the attraction for the axial 1-methyl imidazole ligand.

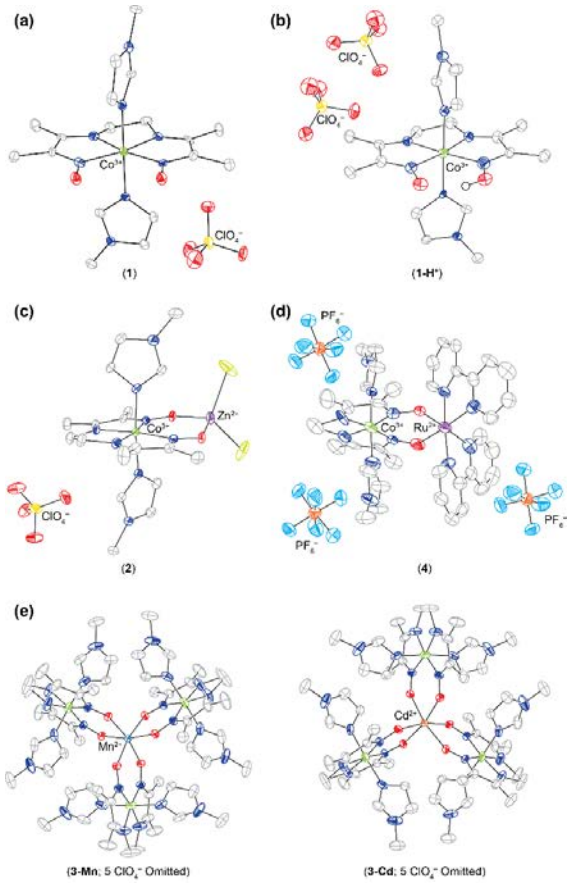

Figure 2.1. Single crystal X-ray diffraction structures of complexes 1 (a), 1-H^+ (b), 2 (c), 4 (d), and 3-M (M = Mn, Cd; e). Hydrogen atoms are omitted for clarity in (a-e) and ClO_4 anions are omitted for clarity in (e).

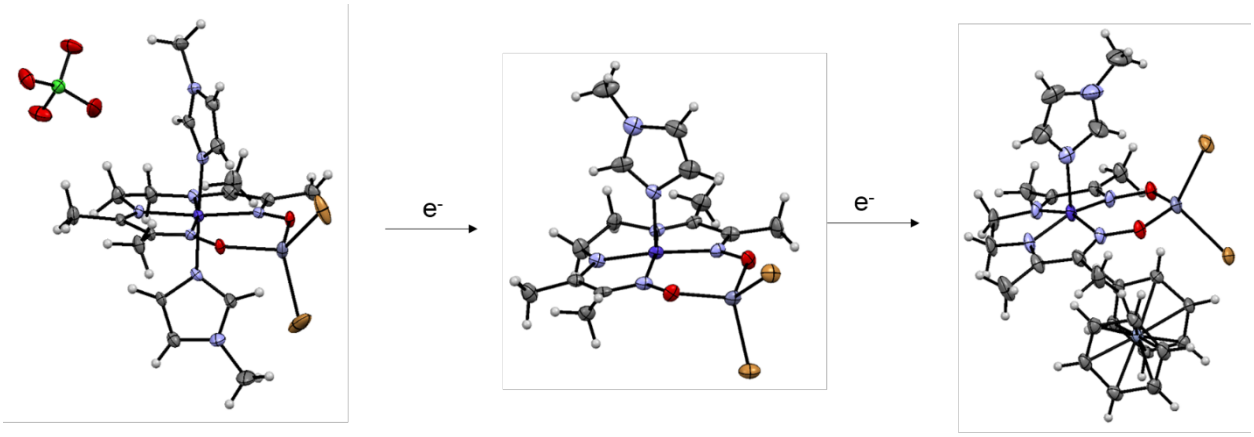

Figure 2.2. Single crystal X-ray diffraction structures of complex 2 and its reduced Co(II) and Co(I) forms. Hydrogen atoms are omitted for clarity.

Table 2.1. Interatomic distance between oximate oxygens

Complex	O-O interatomic distance (Å)	N-Co-N angle
CoRu	3.24(1)	108.9(4)˚
CoNa	3.205(4)	109.1(2)˚
Co_3Cd	3.203(4)	107.9(2)˚
CoZn	3.197(3)	108.9(1)˚
OO	3.128(4)	108.5(1)
Co_3Mn	3.071(3)	106.9(1)˚
Co_3Zn	3.061(4)	106.6(2)˚
OHO	2.564(1)	104.6(4)˚

2.2.3. UV-vis Spectroscopy of Cobalt Diimine Dioximate and Derivatives

The UV-vis absorption spectra of 1, 1-H^+, 2 and 4 in CH_3CN are shown in Figure 1.3. The transitions were assigned using time-dependent density functional theory calculations from the optimized ground state geometries using B3LYP level of theory with LAND2Z basis set for the Ru and 6-311+G(d) for all other

atoms on the Gaussian 09 suit of programs. Comparison of the calculated spectra with the experimental data showed good agreement (see Experimental Figure 2.10). Complex 1 exhibits major absorbance bands in the UV-vis region at 263, 300, 408 and 468 nm. This spectrum is dominated in the visible by the band at 408 nm, which is assigned as predominately interligand and MLCT transitions. Upon protonation to complex 1-H^+, the spectral intensity decreases, but peak positions remain relatively unchanged, leading to lower extinction coefficients across all wavelengths.

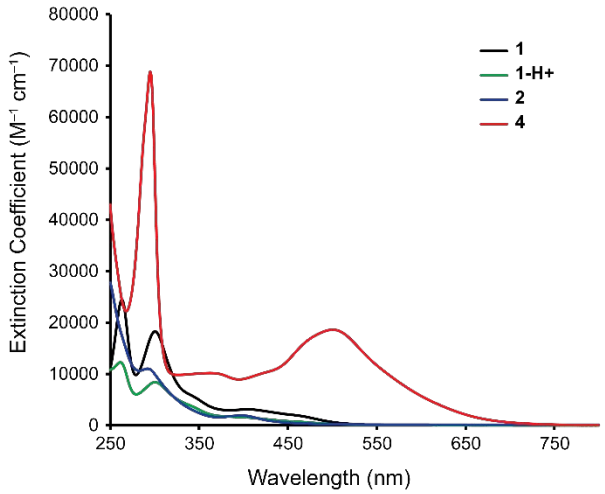

Figure 2.3 UV-vis spectra of complexes 1, 1-H^+, 2 and 4

The UV-vis spectrum of 2 is distinct from 1 even at concentrations as low as 1.0 x10^{-5} M in CH_3CN. Complex 2 exhibits major bands at 292 and 397 nm. The notable difference in the electronic spectra of 2 as compared to 1 is attributed to significant bromide character of the HOMO. The band at 397 nm is a result of interligand transitions.

The electronic spectrum of 4 is dominated by transitions at 295, 373, 420 and 502 nm. The major absorption peak in the visible at 502 nm corresponds to MLCT transitions from d-orbitals on ruthenium to orbitals of pi character on the diimine dioximate metalloligand. The second major absorption peak at 373 nm corresponds to MLCT transitions from ruthenium to bipyridine π* orbitals.

2.2.4. pK_a Determination of Cobalt Diimine Dioximate Complex

Exchange of the bridging proton between complex 1 and 1-H^+ was observed on the ^1H NMR time scale. When a mixture of complex 1 and 1-H^+ is in solution in CD_3CN the NMR resonances observed are mole-weighted fractions of the two components. Utilizing ^1H NMR, a titration was performed with a protonated phosphazene of known pK_a ([2-NO_2-4-CF_3-C_6H_3PH(pyrr)][PF_6]), pK_a=16.54,[23] giving a pK_a of 14.9 for 1-H^+ (See Experimental Figure 2.11). The doubly protonated complex, with both oxime oxygens protonated can be observed following addition of two equivalents of [HDMF][OTf]. This species was identified by UV-vis spectroscopy, which lacks any major absorbance features in the visible, in contrast to complexes 1 and 1-H^+. An estimated pK_a of complex 1-H^+ and the doubly protonated complex were measured by titration of 1 with HCl in water, giving pK_a values of ~6.5 and 2.3-2.5 respectively (See Experimental Figure 2.12).

2.2.5. Electrochemistry of Cobalt Diimine Dioximate and Derivatives

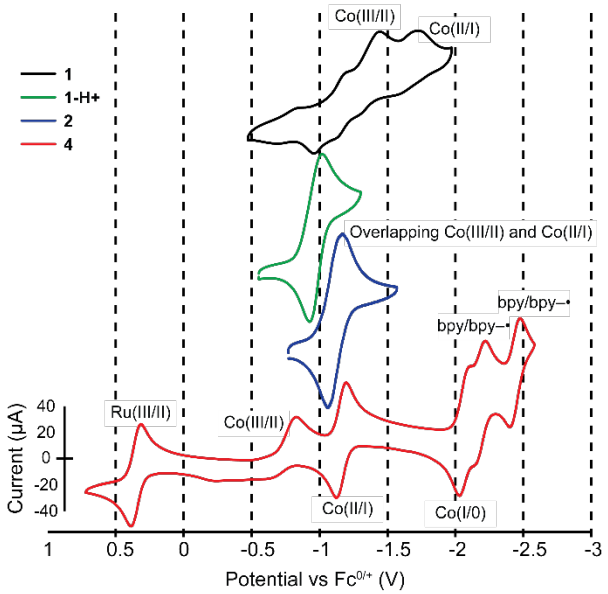

Figure 2.4. Cyclic voltammograms of 1.5mM 1, 1-H^+, 2 and 4 in 0.2 M [$^nBu_4N$][PF_6] /CH_3CN, 300 mV/s, glassy carbon working, Pt auxiliary, Ag pseudo reference and referenced to ferrocene

The cyclic voltammograms of 1, 1-H^+, 2 and 4 are shown in Figure 2.4 in 0.2 M [$^nBu_4N$][PF_6] in CH_3CN. For complex 1, the parent cobalt diimine dioximate, the Co(III/II) and Co(II/I) couples are irreversible with the reductions occurring at −1.46 and −1.69 vs $Fc^{+/0}$, respectively. Formation of a solvento species is observed following the first scan due to equilibrium binding of the Im^{Me} ligands with the solvent in an apparent ECE mechanism (See Experimental Figure 2.13).[9, 24] Upon complexation with cations, the electrochemistry of complexes 1-H^+, 2 and 4 shifts oxidatively as seen in Figure 2.4. Electrochemical analysis of 1-H^+ and 2 in CH_3CN show the Co(III/II) and Co(II/I) redox events overlap to form a peak with an ΔE_p at -0.97 and -1.11 V vs $Fc^{+/0}$, respectively. The large E_p of 82 and 94 mV for complexes 1-H^+ and 2 at a scan rate of 300 mV/s suggests these are overlapping one electron waves. Coulometry was performed to confirm that the Co(III/II) and Co(II/I) redox events are overlapping for complexes 1-H^+ and 2 (See Experimental Figure 2.14). After a 1 hour bulk electrolysis experiment at -1.51 V vs $Fc^{+/0}$ with complex 2, the amount of charge passed corresponds to 2.1 e^- per mole of complex. Following the first complete scan of 2 at 300 mV/s, a new reductive peak appears at -0.78 V, analogous to the solvento species observed for complex 1 ((See Experimental Figure 2.15).[25] The Co(III/II) redox potential for the monoimiadzole complex 2, [$(DO)_2$en(Im^{Me})$CoZnBr_2$], were found from the electrochemistry of the isolated reduced species with a value of -0.633V vs $Fc^{0/+}$ (See Experimental Figure 2.16).This suggests that the varying peak potentials of Co(III/II) of complex 2 is due to fast equilibrium of the bis 1-methyl imidazole and mono 1-methyl imidazole species in fast equilibrium.

In order to observe the electrochemical transition from complex 1 to 2, an electrochemical titration and UV-vis titration were performed (Figure 2.5 and Figure 2.6). The cyclic voltammograms of 3-M show resolved Co(III/II) and Co(II/I) redox couples, similar to CV titrations taken of 1 with 0.5 equivalents of $ZnBr_2$ and the intensities are approximately three times larger than the parent complex 1 (See Experimental Figure 2.17). The presence of multiple peaks in the voltammogram of 3-Zn suggests distinct redox couples for the 3 cobalt centers surrounding a central zinc cation. The $E_{1/2}$ of Co(III/II) and Co(II/I) are -1.06 and -1.17 V for 3-Zn. Scanning past these potentials reveal quasi-reversible reductions (See Experimental Figure 2.18) that are formally a reduction to Co(0). The cyclic voltammogram of the cobalt-ruthenium complex 4 is well resolved with distinct couples for the Ru(III)/(II), Co(III)/(II), Co(II)/(I), Co(I)/(0) and two bpy/bpy(•−) couples observed in CH_3CN (Figure 2.4). The larger difference in Co(III/II) and Co(II/I) peak separation for complex

4 may be attributed to the increased structural rigidity of this complex, as well as the close proximity of the redox active Ru^{2+} metal center. Electron transfer appears to be diffusion-controlled for all complexes since the cathodic and anodic currents vary linearly with the square root of the scan rate (See Experimental Figure 2.19-22).[26]

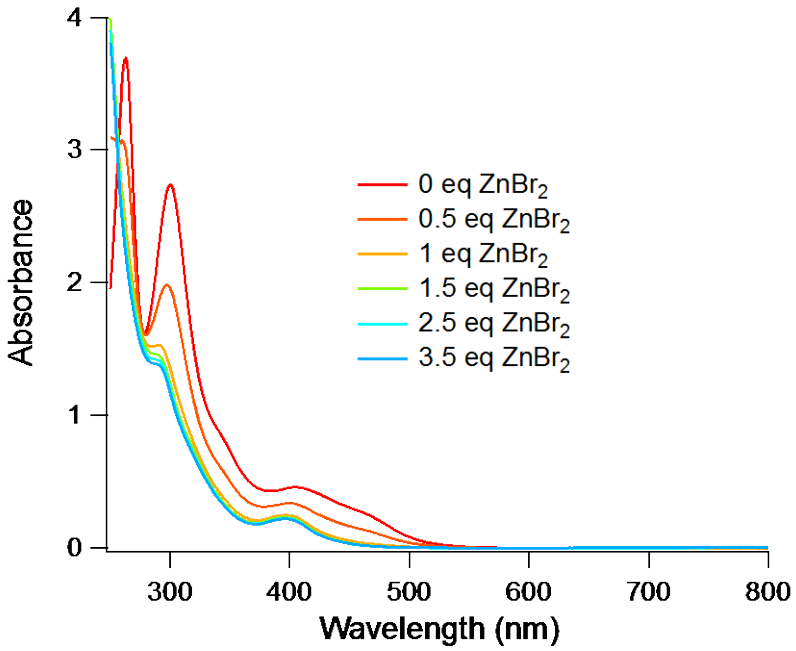

Figure 2.5. UV-vis titration of 1 with $ZnBr_2$ showing no changes after additional equivalents of $ZnBr_2$

The oxidative shift for the derivative complexes Co(III/II) and Co(II/I) redox couples suggest that the complexing cation (nucleophile) takes away electron density from the cobalt metalloligand (electrophile). The magnitude of this shift is directly related to the electronegativity of the cation as the Gibbs free energy of the binding event will be manifested in the change of the Co redox couples (this is convoluted to a degree due to ^{Me}Im equilibrium binding), with the following trend $H^+ > Zn^{2+} > Ru^{2+}$.

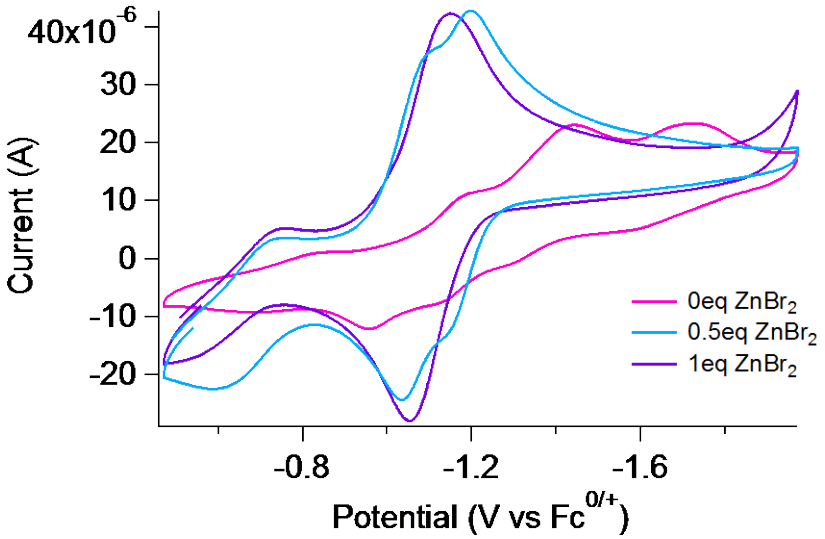

Figure 2.6. CV titration of 1.5mM 1 with $ZnBr_2$ showing complete conversion to 2 after addition of 1 equivalent of $ZnBr_2$ in 0.2M $[^nBu_4N][PF_6]$ in CH_3CN, glassy carbon working, Pt auxiliary, Ag pseudo reference and referenced to ferrocene

2.2.6 Electrochemical Proton Reduction Studies

To probe the catalytic response of 1, 1-H^+, 2 and 4 to proton reduction, these complexes were treated with increasing equivalents of acid and subjected to reducing conditions by cyclic voltammetry. We have found that in electrochemical experiments using acids such as [HDMF][OTf] (pk_a=6.1)[27] and

CF_3COOH (pK_a=12.65)[28] with complex 1 resulted in a catalytically-active film forming on the electrode surface.[29] This was monitored using the rinse test (Figure 2.7).[30]

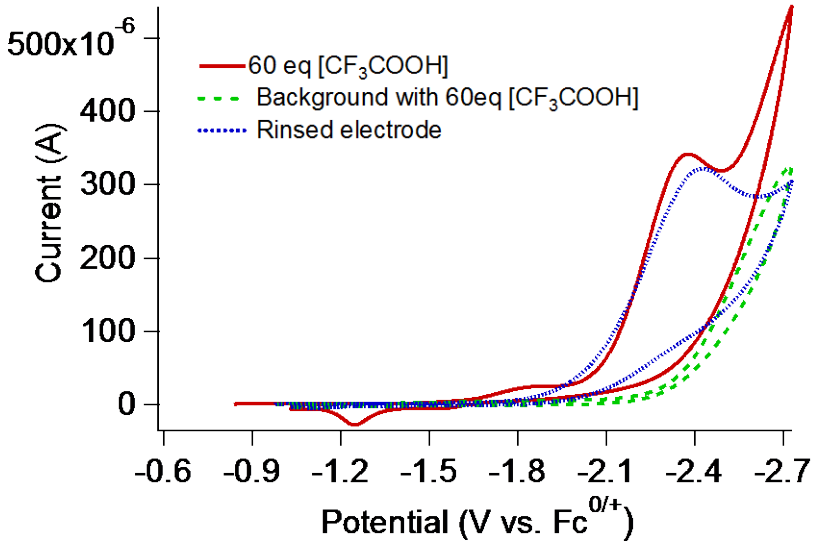

Figure 2.7. 0.35mM 1 with 60 eq (21mM) [CF_3COOH], scan rate 300mV/s, 0.1M [$^nBu_4N$][PF_6] in CH_3CN, glassy carbon working, Pt auxiliary, Ag pseudo reference and referenced to ferrocene. The rinsed electrode was placed in a solution of 21mM [CF_3COOH].

The acid stability of complex 1 was examined using ^1H NMR spectroscopy with no decomposition products appearing following addition of 60 equiv. CF_3COOH to complex 1 under non-reducing conditions (See Experimental Figure 2.23). Experiments utilizing a weaker acid, such as [NEt_3H][Cl] with a pK_a of 18.82,[23] resulted in a catalytic current response that is attributable to homogenous proton reduction catalysis yielding H_2, however chloride binding was found to deactivate the catalyst, leading to a cathodic drift of the catalytic response (See Experimental Figure 2.24).[12] To avoid this, [NEt_3H][BPh_4], was used and this resulted in catalytic current that was distinct from the background glassy carbon catalytic current (Figure 2.8 and Figure A4.25-A4.27). The homogeneous nature of the catalyst using [NEt_3H][BPh_4] as the acid source is supported by the rinse test and by evidence of a return oxidative molecular peak as seen in Figure 2.8.

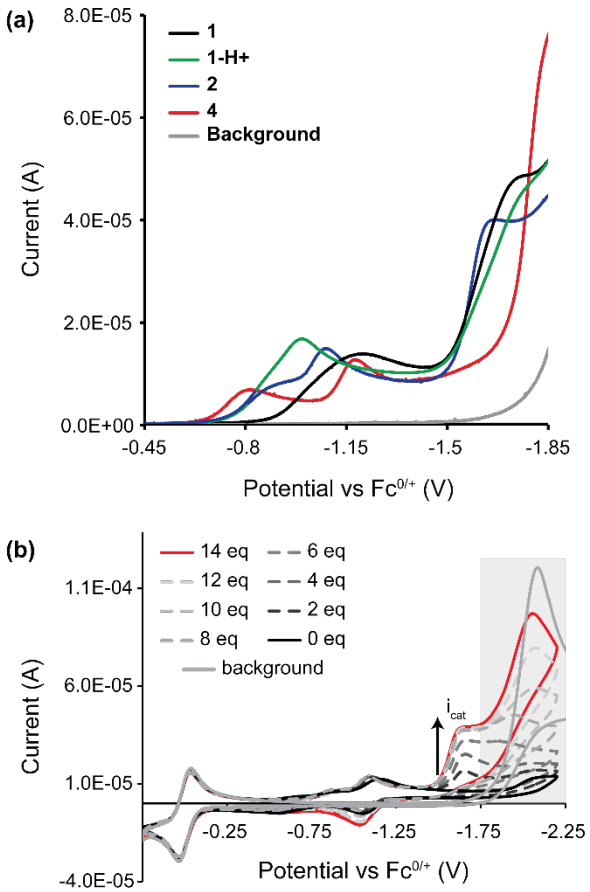

Figure 2.8. a) Electrocatalytic proton reduction for 0.75mM 1, 1-H$^+$, 2 and 4. At this scan rate, the current reaches limiting conditions at 8 eq of acid. Conditions: 7.5mM [NEt$_3$H][BPh$_4$], 0.2 M [^{n}Bu$_4$N][PF$_6$] in CH$_3$CN at 50 mV/s scan rate b) Electrocatalytic H$_2$ production for 0.75 mM 2 Conditions: 0-10.5 mM [NEt$_3$H][BPh$_4$], 0.2 M [^{n}Bu$_4$N][PF$_6$] in CH$_3$CN at 50 mV/s scan rate, glassy carbon working, Pt auxiliary, Ag pseudo reference and referenced to ferrocene. For a and b, the background scan is with 8 or 14 eq of acid, respectively, in the absence of added catalyst.

Addition of increasing equivalents of [NEt$_3$H][BPh$_4$] results in the appearance of a peak at -1.6 V vs Fc$^{0/+}$. This peak occurs at potentials more negative than the Co(II/I) couple and positive of the Co(I/"0"). Given the potential that this catalytic peak occurs, likely the Co^I species is not basic enough to be protonated and the complex must be reduced further to Co"0".[11] This is further supported by the fact that the Co(II/I) couple is more positive than the standard potential for the HA/A$^-$,H$_2$ couple of [NEt$_3$H][BPh$_4$] in CH$_3$CN.[31] This means this system needs a more reducing active species than Co(I) in order to reduce the H$^+$ of

[NEt_3H][BPh_4] to H_2. This Co"0" species is now basic enough to be protonated to form a Co^{II}-H (Scheme 2.5). Two pathways have been proposed in order to generate hydrogen from this initial protonation of a cobalt species. 1) In a heterolytic mechanism, reduction of this Co^{II}-H to Co^{I}-H, the catalytic species occurs and this species is protonated to regenerate Co^{I}. 2) Two Co^{II}-H react in a bimetallic fashion to generate H_2.[11, 13] Given new findings of recent literature on mechanistic studies on cobaloximes suggesting only the heterolytic mechanism is operative, we assume the same of our system. [32]

At 50mV/s, the peak reaches a plateau current at 12-14 eq of acid added. The presence of a plateau denotes that the electrochemical process is not limited by diffusion, allowing the assumption that the concentration of the analyte and substrate are the same in the bulk as well as on the surface of the electrode. This plateau is indicative of the observed rate constant of the regeneration of Co^{I} and its value reflects the rate determining step in this process. Inherent in our assumptions is that the electron transfers are fast compared to the time scale of the experiment and therefore would not be rate determining. The first protonation step from Co"0" to Co^{II}-H, is likely fast given an oxidative shift in the catalytic peak upon subsequent additions of acid.[32] Given the very weak acidity of the [NEt_3H][BPh_4], it is likely the rate-determining step is the protonation of the Co^{I}-H. The presence of a plateau current at slow scan rates is indicative of a slow k_e according to the kinetic zone diagrams of Savèant and coworkers.[33]

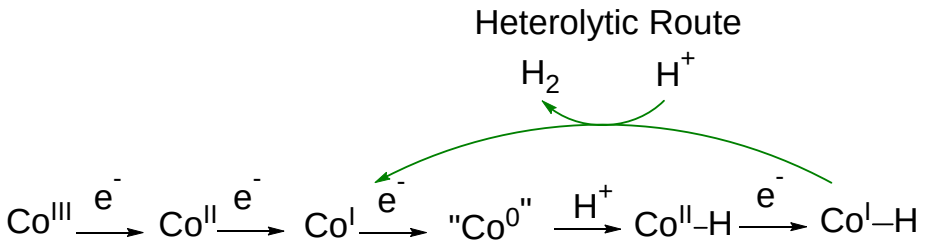

Scheme 2.5. Proposed catalytic cycle for electrochemical proton reduction

The ratio of the catalytic current to the peak current for the molecular redox couple of interest, i_{cat}/i_p, is a metric that can be utilized to compare catalyst performance. This method internally accounts for the diffusion coefficient, electrode area and concentration of catalyst.[34] The i_{cat}/i_p is proportional to the k_{obs} and can be used to make relative comparisons of catalytic activity. The i_{cat}/i_p presented here compare favorably

with other cobalt catalysts. Complex 4 affords an i_{cat}/i_p of 6.4 at 50 mV/s[24], which can be compared to other complexes that catalyze proton reduction in CH_3CN,[17, 29, 35] though these complexes have lower rates than some diglyoxime counterparts ($Co[(dmgBF_2)_2(MeCN)_2$) (i_{cat}/i_p of ~40 at 100 mV/s).[13]

The overpotentials for complexes 1, 1-H^+, 2 and 4 were determined according to the $E_{cat/2}$[10] at 10 eq $[NEt_3H][BPh_4]$ at a scan rate of 50 mV/s (Table 2.2). Similar overpotential values and i_{cat}/i_p values are found for complex 1, 1-H^+ and 2. The lowest overpotential was found for 2 (320 mV) and the highest for complex 4 with 480 mV overpotential. Like many molecular catalysts, the complexes with the highest overpotential also have the highest rates.[36]

A greater difference in proton reduction rate would be expected given the drastic change in redox potentials afforded upon complexation of H^+ or Zn^{2+}, however very distinct overpotentials and rates were most evident for complex 4. We hypothesized this was due to protonation of the complex upon reduction, since this reduced complex is likely more basic. Our hypothesis is supported by the use of a stronger acid, ^{Me}ImH, in which complexes 1, 1-H^+ and 2 have essentially identical overpotentials, while complex 4 still remains distinct (See Experimental Figure 2.28) This suggests that protonation of the O-O binding pocket can be prevented through appropriate choice of the bound cation.

Table 2.2. Overpotentials, i_c/i_p and Faradaic efficiencies for proton reduction listed for Complexes 1, 1-H^+, 2 and 4 using $[NEt_3H][BPh_4]$, as an acid source. The ratios i_c/i_p were calculated from i_{pl}[37] using 7.5 mM $[NEt_3H][BPh_4]$, and 0.75 mM [cat] at 50 mV/s (Figure 2.25-2.27 and Figure 2.8), with diffusion coefficients calculated from ^{1}H DOSY NMR. Faradaic efficiencies were computed from hydrogen measured by GC-TCD following bulk electrolysis using a graphite rod as the working electrode.

	1	**1-H^+**	**2**	**4**
i_c/i_p	3.7	3.7	3.4	6.4
Overpotential (V)	0.36	0.38	0.32	0.48
Faradaic Efficiency (%)	63	72	21	80

Bulk electrolysis experiments confirm hydrogen production for all catalysts (See Experimental Table 2.3-2.4). Experiments were run using 0.25 mM catalyst and 25 mM $[NEt_3H][BPh_4]$, and H_2 was measured using a gas chromatograph equipped with a thermal conductivity detector. Each catalyst was held at its overpotential value for the controlled potential electrolysis. Background proton reduction from the electrode in the presence of acid was determined in each case and subtracted from the total amount of hydrogen produced in the presence of catalyst in order to calculate the reported Faradaic efficiencies provided in Table 2.2. However, at potentials necessary to observe hydrogen production, a catalytically active film forms during the course of the bulk electrolyses. This was confirmed to be a complication in the bulk electrolysis experiments using a graphite as shown by the rinsed electrode traces (See Experimental Figures 2.29-32).

2.3 Conclusions

The presented work has demonstrated that the ethylene bridged diimine monoxime monoximate cobalt complex can be cleanly deprotonated and the resulting complex can function as a metalloligand to create a family of multimetallic proton reduction catalysts. These complexes are stable to dissociation at low concentrations in CH_3CN and the acid stability of the complexes can be controlled by the identity of the bound cation. The coordination of the doubly deprotonated metalloligand (complex 1) with a proton or metal complex, results in a shift of Co(III/II) and Co(II/I) to more positive potentials, with overlapping Co(III/II) and (II/I) waves observed for 3 and 1-H^+. Importantly, this allows the study the association of complex 1 as a nucleophile via a variety of spectroscopic methods. Complex 2 can be reduced to its Co(II) and Co(I) derivatives and these complexes are both mono-imidazole species in the solid state confirming an open site necessary for proton reduction. While these complexes appear stable under typical catalytic conditions using cyclic voltammetry, these complexes decompose under extended electrolysis conditions resulting in catalytically active films.

We demonstrate the use of this cobalt diimine dioximate complex as a bidentate metalloligand for a variety of metal ions, allowing the isolation of new bimetallic and multimetallic complexes. The versatility of this diimine dioximate metalloligand can be seen in its ability to bind a range of cations, including H^+,

$Zn^{2+,}$ Cd2+, Mn2+, and Ru2+ with a variety of ancillary ligands, making this approach generalizable to the synthesis of multimetallic complexes.

2.4 Experimental Section

2.4.1 General Considerations

(DO)(DOH)enCoBr$_2$[21], [NEt$_3$H][BPh$_4$][38] ([^{Me}ImH][BPh$_4$] was synthesized analogously; both were recrystallized once from acetone), [HDMF][OTf][39] and RuCl$_2$(bpy)$_2$[40] were synthesized according to published procedures. The phosphazene acid, [2-NO$_2$-4-CF$_3$-C$_6$H$_3$P$_1$H(pyrr)][PF$_6$], was synthesized by Prof. Caroline Saouma from published procedures.[23] NMR solvents were purchased from Cambridge Isotope Labs and used as received. Neat phosphoric and trifluroracetic acid were used as internal standards for ^{31}P and ^{19}F NMR experiments, respectively. ^{1}H NMR is reported referenced to internal proteo solvent resonances. All other reagents and solvents not highlighted below were bought from Sigma Aldrich and used as received. UV-Vis spectra were acquired on a Cary 5000 spectrophotometer from Agilent Technologies.

The electrolyte [^{n}Bu$_4$N][PF$_6$] used in cyclic voltammetry experiments was either recrystallized two times in EtOH and dried overnight under vacuum at 100 °C or electrochemical grade ≥ 99% was purchased from Sigma-Aldrich. All CV experiments were taken in a N_2 filled glove box. Glassy carbon working electrodes (CH Instruments and BASi), platinum auxiliary electrode (BASi) and a Ag wire pseudo reference electrode in a Vycor-fritted compartment (BASi) filled with [^{n}Bu$_4$N][PF$_6$] and CH_3CN were used. Glassy carbon electrodes with a diameter of 3.0 mm were polished using 0.05, 0.3 and 1.0 micron polishing powder (CHI instruments) followed by 5 minute sonication cycles in deionized water after every CV that was run for electrocatalytic experiments. All experiments were referenced to an internal ferrocene standard added after the experiment unless otherwise noted, Ultra-high purity acetonitrile used in cyclic voltammetry (Burdick and Johnson) was dried over alumina overnight, subjected to 3 freeze pump thaw cycles, brought in the glove box, filtered and stored over 3 Å molecular sieves. For bulk electrolysis experiments a custom cell was constructed using a curly platinum wire as the auxiliary electrode, a silver wire as the reference

electrode, and a graphite rod (Pine Instruments) as the working electrode. For visualizing catalyst decomposition, FTO-coated glass slides were used as the working electrode. In all cases the cell potential was referenced to ferrocene as an internal standard. Hydrogen was detected using a SRI gas chromatograph equipped with a TCD detector using argon carrier gas and a 6' MS-13X column. Hydrogen was quantified using a calibration curve created by injecting a known amount of hydrogen into the bulk electrolysis cell (Figure S37) and allowing the cell to equilibrate for 10 min with stirring. Aliquots from the headspace of these cells were injected into the GC and the peak for hydrogen was integrated. Rinse test traces were performed by rinsing the used electrode from the given experiment and then using this same electrode in a new solution of the same acid concentration at the same scan rate and potential.

Caution! Perchlorate salts of metal complexes with organic ligands are potentially explosive and should only be handled in small quantities in dry form.

2.4.2 Synthesis of Complex 1, $[(DO)_2enCo(Im^{Me})_2][ClO_4]$.

3.438 g (7.74 mmol, 1 eq) of (DOH)(DO)enCoBr_2 was suspended in 250 mL of CH_3CN. To this solution, 3.06 mL (38.7 mmol, 5 eq) of 1-methyl imidazole was added. The solution became dark red and homogeneous. To this solution 2.884 g (7.74 mmol, 1 eq) of zinc perchlorate hydrate was added. The reaction was stirred overnight and a golden solid crashed out of solution during that time. The reaction mixture was filtered and the solids were washed with acetonitrile. The isolated solids were recrystallized from MeOH. Yield = 2.611 g (4.77 mmol, 63%).

^{1}H NMR (300 MHz, DMSO-d_6) 1.87 (6H, s), 2.36 (6H, s), 3.60 (6H, s), 4.66 (4H, s), 6.71 (2H, s), 7.07 (2H, s), 7.52 (2H, s) ppm

^{1}H NMR (499 mHz, CD_3CN) 1.93 (6H, s), 2.34 (6H, s), 3.57 (6H, s), 4.55 (4H, s), 6.63 (2H, t), 6.83 (2H, t), 7.28 (2H, s) ppm

^{13}C NMR (75 MHz, DMSO-d_6) 12.6, 16.9, 34.4, 51.9, 122.1, 127.0, 137.9, 150.4, 176.3 ppm

ε (L mol^{-1} cm^{-1})= 25,000 +/- 240 at 263 nm, ε= 1,800 +/- 120 at 300 nm, ε= 5,000 +/- 60 at 345 nm, ε= 3,000 +/- 20 at 408 nm, ε= 1,700 +/- 30 at 468 nm

Elemental Analysis Calculated for **1** ($C_{18}H_{28}ClCoN_8O_6$): C, 39.53; H, 5.16; N, 20.49. Found: C, 39.47; H, 4.75; N, 20.24.

2.4.3 Synthesis of Complex 1-H^+, $[(DOH)(DO)enCo(Im^{Me})_2][PF_6]_2$.

0.682 g (1.25 mmol, 1 eq.) of **1** was suspended in 75 mL of CH_3CN. To this suspension 0.278 g (1.25 mmol, 1 eq) of [HDMF][OTf] was added. The solution became light yellow and homogeneous on stirring. The CH_3CN was removed by vacuum and the remaining residue was dissolved in water. To this solution, an aqueous solution of excess $[NH_4][PF_6]$ was added and the solid product began to crystallize from solution. After cooling to 3 °C, the solid was filtered and washed with water. Yield = 0.756 g (1.02 mmol, 82%). Alternatively, this complex can by protonated by CF_3COOH and recrystallized from warm MeOH containing excess $NaClO_4$ (yields the perchlorate salt).

^1H NMR (500 MHz, CD_3CN) 2.32(6H, s), 2.52(6 H, s), 3.63(6H, s), 4.79(4H, s), 5.57(1H, br), 6.51(2H, t), 7.01(2H, st), 7.20(2H, t) ppm

^{13}C NMR (125.7 MHz, CD_3CN) 14.1, 19.6, 35.8, 55.0, 124.3, 127.0, 139.2, 162.0, 181.1 ppm

^{19}F NMR (282.4 MHz, CD_3CN) -68.52 (d) ppm; $^1J_{F\text{-}P}$ 705.5 Hz

^{31}P NMR (202.4 MHz, CD_3CN) -143.15 (sep) ppm; $^1J_{P\text{-}F}$ 707.2 Hz

Elemental Analysis Calculated for **1-H^+** ($C_{18}H_{29}CoF_{12}N_8O_2P_2$): C, 29.28; H, 3.96; N, 15.18. Found: C, 29.52; H, 3.83 ;N, 15.01.

2.4.4 Synthesis of Complex 2, $(DO)_2enCo(Im^{Me})_2ClO_4ZnBr_2$.

0.117 g (0.21 mmol, 1eq) of **1** and 0.043 g (0.19 mmol, 1 eq) of $ZnBr_2$ were suspended in 5 mL of MeOH and stirred overnight. A light yellow precipitate formed and was isolated by filtration and dried under vacuum. These solids were recrystallized from acetonitrile. Yield = 0.078 g (0.101 mmol, 47%).

^{1}H NMR (499 MHz, DMSO-d_6) 2.01 (6H, s), 2.45 (6H, s), 3.60 (6H, s), 4.66 (4H, s), 6.68 (2H, s), 7.14 (2H, s), 7.53 (2H, s) ppm

^{1}H NMR (499 mHz, CD_3CN) 2.26 (6H, s), 2.51 (6H, s), 3.64 (6H, s), 4.58 (4H, s), 6.57 (2H, s), 6.99 (2H, s), 7.39 (2H, s) ppm

^{13}C NMR (126MHz, CD_3CN) 14.21, 19.40, 35.81, 54.53, 123.94, 127.44, 140.40, 161.46, 181.20 ppm

ε (L mol^{-1} cm^{-1})= 11,000 +/- 500 at 292 nm, ε= 1,700 +/- 290 at 397 nm

Elemental Analysis Calculated for **2** ($C_{18}H_{28}Br_2ClCoN_8O_6Zn$): C, 28.00; H, 3.66; N, 14.51. Found: C, 27.63; H, 3.67; N, 14.17.

2.4.5 Synthesis of Complex 3-Zn, $[(DO)_2enCo(Im^{Me})_2ClO_4]_3Zn(ClO_4)_2$.

0.150g (0.92 mmol, 3 eq) of **1** was suspended in 50 mL of a 1:1 MeOH:H_2O mixture along with 0.114 g (0.31 mmol, 1 eq) of $Zn(ClO_4)_2$•$6H_2O$ and stirred overnight. Upon evaporation of MeOH and cooling of the solution to 3 °C, a yellow solid crashed out. The supernatant was decanted and the solids were dried under vacuum to yield a yellow-orange powder. Crystals were grown from a 1:1 H_2O:MeOH solution. Yield = 0.428 g (0.22 mmol, 73%).

^{1}H NMR (499 mHz, CD_3CN) 2.23 (18H, s), 2.50 (18H, s), 3.46 (18H, s), 4.64 (12H, s), 6.68 (6H, s), 6.80 (6H, s), 7.32 (6H, s) ppm

^{13}C NMR (126MHz, CD_3CN) 13.81, 19.00, 35.58, 54.07, 123.54, 127.89, 139.32, 159.71, 180.61 ppm

ε (L mol^{-1} cm^{-1}) = 33,000 +/- 1,000 at 296 nm, ε = 5,700 +/- 300 at 392 nm, ε = 2,000 +/- 100 at 465 nm

Elemental Analysis Calculated for **3-Zn·5H_2O** ($C_{54}H_{96}Cl_5Co_3N_{24}O_{32}Zn$): C, 32.22; H, 4.81; N, 16.70. Found: C, 32.63; H, 4.58; N, 16.73.

2.4.6 Synthesis of Complex 3-Mn, $[(DO)_2enCo(Im^{Me})_2ClO_4]_3Mn(ClO_4)_2$.

0.080 g (0.15 mmol, 3 eq) of **1** and 0.014 g (0.049 mmol, 1 eq) of $Mn(ClO_4)_2 \cdot 6H_2O$ were suspended in 50 mL of a 1:1 MeOH:H_2O mixture and stirred overnight. The mixture was then decanted and the solids were dried under vacuum. The solids collected were recrystallized from a 1:1 MeOH and H_2O mixture by slow cooling from a 60 °C solution to room temperature overnight. The crystallized solids were collected and dried under vacuum giving a 50% yield (0.048 g, 0.025 mmol).

ε (L mol^{-1} cm^{-1})= 44,000 +/- 2,700 at 300 nm, ε = 7,700 +/- 300 at 401 nm, ε = 3,100 +/- 240 at 461 nm

Elemental Analysis Calculated for **3-Mn·5H_2O** ($C_{54}H_{96}Cl_5Co_3N_{24}O_{32}Mn$): C, 32.39; H, 4.83; N, 16.79. Found: C, 32.89; H, 4.58; N, 16.77.

2.4.7 Synthesis of Complex 3-Cd, $[(DO)_2enCo(Im^{Me})_2ClO_4]_3Cd(ClO_4)_2$.

This complex was synthesized using the same prep as **3-Mn**, using 0.311 g (0.57 mmol, 3 eq) of **1** and 0.062 g (0.19 mmol, 1 eq) of $Cd(ClO_4)_2 \cdot 6H_2O$. The product was collected with a 42% yield (0.155 g, 0.079 mmol).

^{1}H NMR (499 mHz, CD_3CN) 2.23 (18H, s), 2.47 (18H, s), 3.26 (18H, s), 4.54 (12H, broad s), 4.78 (12H, broad s), 6.53 (6H, s), 6.80 (6H, s), 7.35 (6H, s) ppm

^{13}C NMR (126 MHz, CD_3CN) 13.69, 18.88, 35.34, 53.73, 122.89, 128.51, 139.27, 159.10, 180.47 ppm

ε (L mol^{-1} cm^{-1}) = 68,000 +/- 1,500 at 259 nm, ε = 40,000 +/- 670 at 297 nm, ε = 7,000 +/- 450 at 404 nm

Elemental Analysis Calculated for **3-Cd·5H_2O** ($C_{54}H_{96}Cl_5Co_3N_{24}O_{32}Cd$): C, 31.49; H, 4.70; N, 16.32. Found: C, 31.82; H, 4.47; N, 16.35.

2.4.8 Synthesis of Complex 4, $(DO)_2enCo(Im^{Me})_2Ru(bpy)_2(OTf)_3$.

0.500 g (1.03 mmol, 1 eq) of $RuCl_2(bpy)_2$ was suspended in 20 mL of a 2:1 EtOH:H_2O mixture. To this suspension, 0.531 g (2.06 mmol, 1 eq) of AgOTf was added and the mixture was stirred for 30 min at 60

°C. This solution was filtered through Celite to remove AgCl and the solvent was then removed under vacuum. To this red solid, 4 mL of 2:1 ethanol:water was added. 0.565 g (1.03 mmol, 1 eq) of **1** was added and the reaction mixture was stirred overnight at 60 °C (refluxing the reaction or heating to higher temperatures will favor the formation of $Ru(bpy)_2(Im^{Me})_2(OTf)_2$). The solvent was again evaporated and the resulting purple solid was suspended in 4-6 mL of H_2O. This suspension was filtered and washed sparingly with water. Yield= 0.467 g (0.40 mmol, 38.5%). The ClO_4 anion was exchanged for OTf by dissolving the product in water (~250 mL for 0.5 g), adding an aqueous solution of excess LiOTf, and cooling to 3 °C. From this solution a fine powder crystallizes.

^{1}H NMR (499 mHz, CD_3CN) 2.20 (18H, s), 2.48 (18H, s), 3.44 (18H, s), 3.79 (12H, d), 4.23 (12H, d), 5.97 (6H, s), 6.54 (6H, s), 6.85 (6H, s), 7.18-7.21 (4H, m), 7.57 (2H, d), 7.86 (2H, t), 7.99-8.03 (4H, m), 8.36 (2H, d), 8.43 (2H, d) ppm

^{13}C NMR (499MHz, CD_3CN) 14.40, 19.21, 36.01, 54.55, 120.85, 123.41. 124.11, 124.34, 124.62, 126.41, 126.76, 137.10, 138.90, 151.53, 154.30, 159.28, 160.96, 161.75, 179.00 ppm

^{19}F NMR (499MHz, CD_3CN) -77.25 ppm

ε ($L\ mol^{-1}\ cm^{-1}$) = 70,000 +/- 1,000 at 295 nm, ε= 11,000 +/- 28 at 373 nm, ε= 10,000 +/- 50 at 420 nm, ε= 19,000 +/- 300 at 502 nm

Elemental Analysis Calculated for **4** ($C_{42}H_{48}CoF_9N_{12}O_{11}RuS_3$): C, 38.10; H, 3.65; N, 12.69. Found: (average of 3 trials of 2 separate syntheses with standard deviation) C, 35.52 ± 0.389; H, 3.62 ± 0.14; N, 12.11 ± 0.18.

2.4.9 Synthesis of $(DO)_2enCo(Im^{Me})ZnBr_2$

0.050 g (0.066 mmol, 1 eq) of complex 2 was dissolved in 5 mL of CH_3CN and cooled to -35 degrees C. 0.0138 g (0.066 mmol, 1 eq) of $Cr(bn)_2$ was also dissolved in CH_3CN and cooled to -35 °C. The solution of $Cr(bn)_2$ was added to the solution of complex 2. The reaction was allowed to stir and thaw to room temperature and was reacted for one hour. The solvents were removed by vacuum and 10-20 mL of THF was added. This was stirred and filtered to remove the soluble, yellow byproduct. The solids were dissolved

in a mixture of minimal solvent (90/10 ratio of CH_3CN/THF) and cooled to -35 °C. Crystals were grown in this manner.

2.4.10 Synthesis of $(DO)_2enCo(Im^{Me})ZnBr_2$ ($Cr(bn)_2$)

0.119 g (0.16 mmol, 1 eq) of complex 2 was dissolved in 10 mL of CH_3CN and cooled to -35 degrees C. 0.329 g (1.58 mmol, 10 eq) of $Cr(bn)_2$ was also dissolved in CH_3CN and cooled to -35 °C. The solution of $Cr(bn)_2$ was added to the solution of complex 2. The reaction was allowed to stir and thaw to room temperature and was reacted for one hour. The solvents were removed by vacuum and 20 mL of THF was added. This was stirred and filtered to remove the soluble, yellow byproduct. The solids were dissolved in a mixture of minimal solvent (90/10 ratio of CH_3CN/THF) and cooled to -35 °C. Crystals were grown in this manner.

2.4.11 Supplementary crystal structures

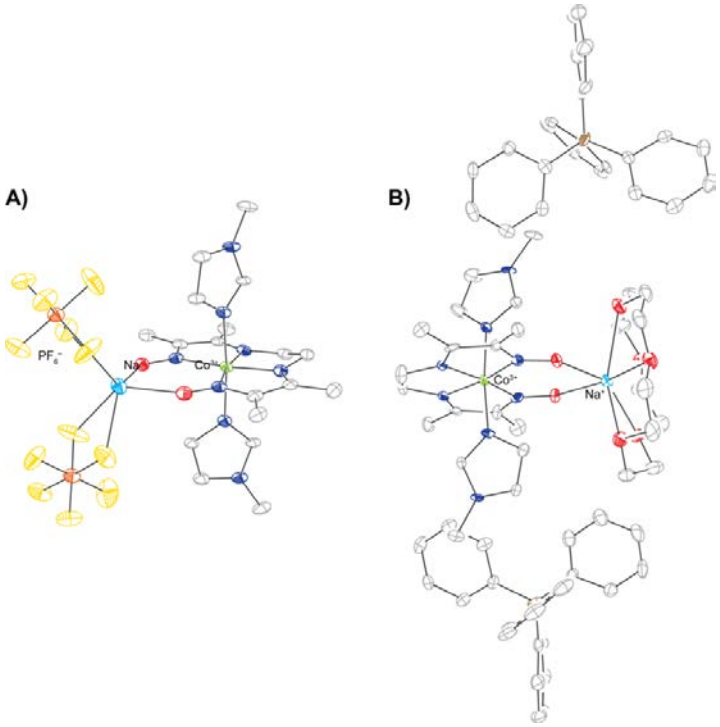

Figure 2.9 A) Single crystal X-ray diffraction structure of $[(DO)_2en(Im^{Me})_2CoNa][PF_6]_2$ and B) $[(DO)_2en(Im^{Me})2CoNa\text{-}15crown5][BPh_4]_2$ isolated from treatment of 1 with $NaPF_6$ and $NaBPh_4$ and 15-crown-5, respectively.

2.4.12 Theoretical versus experimental UV-vis spectra

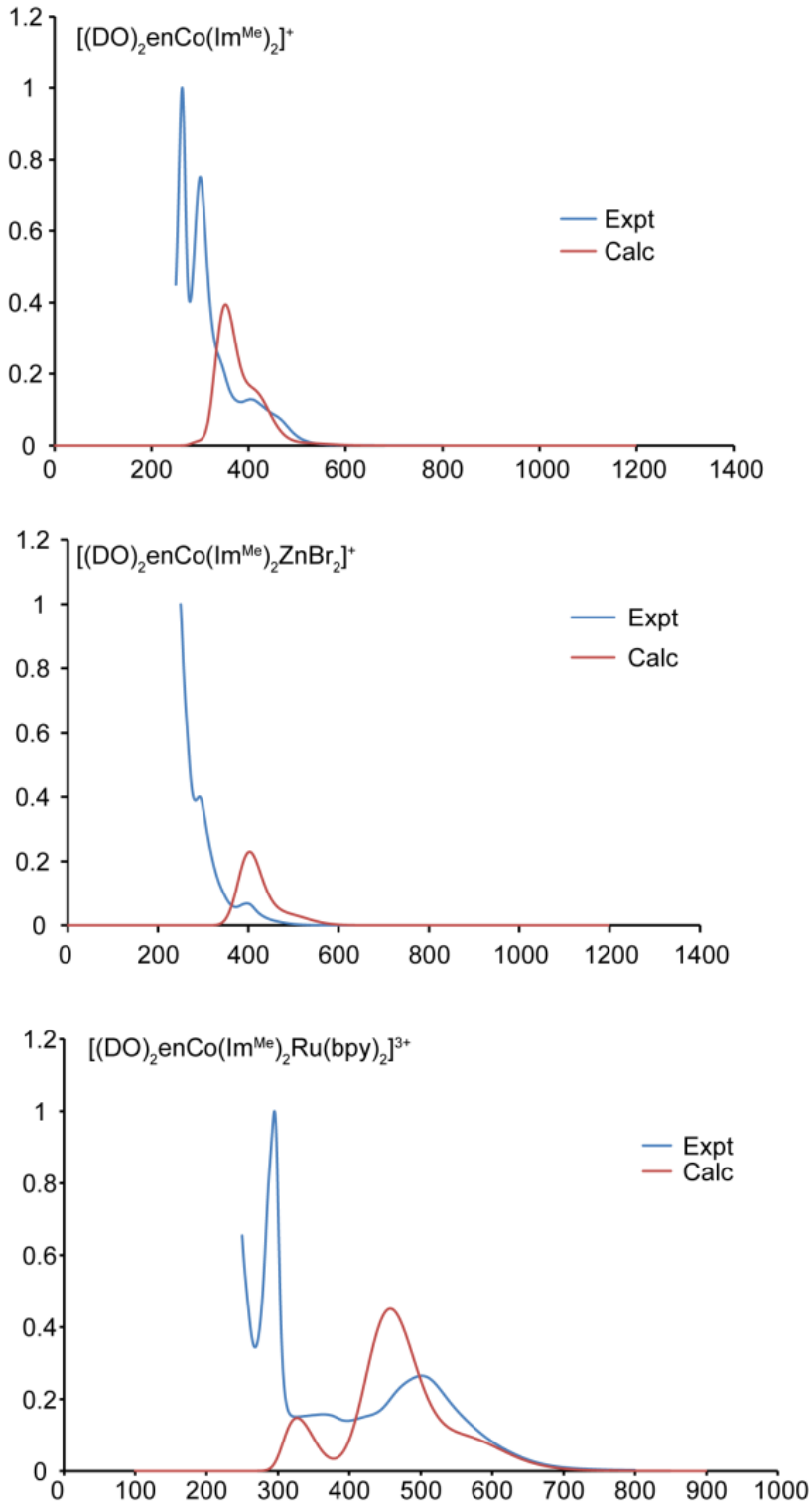

Figure 2.10. Calculated versus experimental UV-vis spectra for 1, 2, and 4.

2.4.13 Determination of pK_a and pH for complex 1

The pK_a for Complex 1-H^+ was found using ^1H NMR spectroscopy. The exchange between Complex 1 and 1-H^+ was fast on the NMR time scale. Complex 1 was titrated with 2-NO_2-4-CF_3-$C_6H_3P_1H$ (pyrr) PF_6, which has a pK_a of 16.54.[41]

$$1 + HB \rightleftarrows 2 + B$$

The chemical shift was a mole-fraction weighted average of 1 and 1-H^+,

$$\delta_{obs(1)} = N_1\delta_1 + N_{1-H+}\delta_{1-H+}$$

In this expression N represents the mole fraction of Complex 1 or 1-H^+. Expressing this equation in molarity units leads to the following expression. Adapting the method from Drago (Chapter 8)[42], leads to the following expression for $[2]_t$.

$$[2]_t = \frac{(\delta_{obs} - \delta_1)}{(\delta_2 - \delta_1)}[1]_0$$

The following terms, $[1]_t$, $[BH]_t$ and $[B]_t$ can be found from the following expressions,

$$[1]_t = [1]_0 - [2]_t$$

$$[BH]_t = [B]_x - [2]_t$$

$$[B]_t = [2]_t$$

The following equilibrium expression can be plotted to yield the equilibrium constant.

$$K = \frac{[1][BH]}{[B][2]}$$

From the K value determined from Figure S1 below, the pK_a was calculated from the following expression, where pK_a(BH) is the pK_a of the titrated acid, 2-NO_2-4-CF_3-$C_6H_3P_1H$ (pyrr) PF_6.

$$pK_a(2) = pK_a(BH) - \log K$$

A pK_a of 14.9 was found experimentally for Complex 1-H^+.

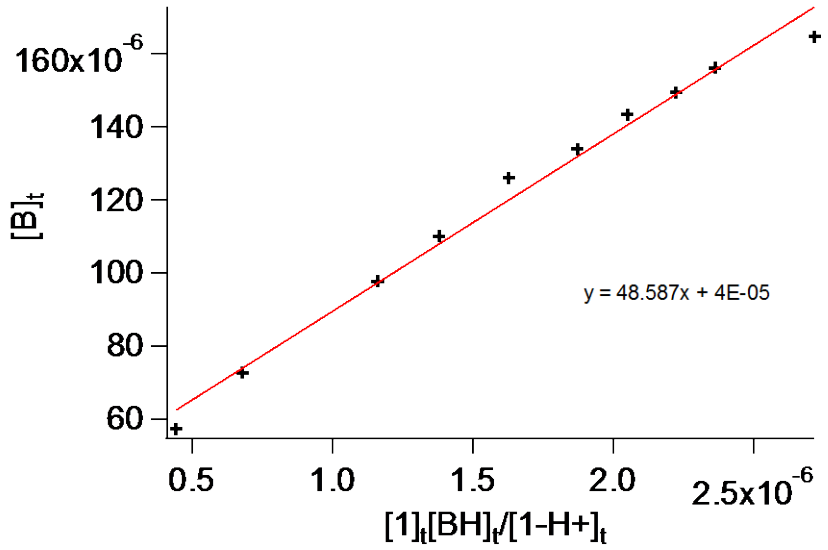

Figure 2.11. Graph with the necessary parameters to determine pK_a of Complex 1-H^+ by ^1H NMR titration, where the slope is the equilibrium constant, K.

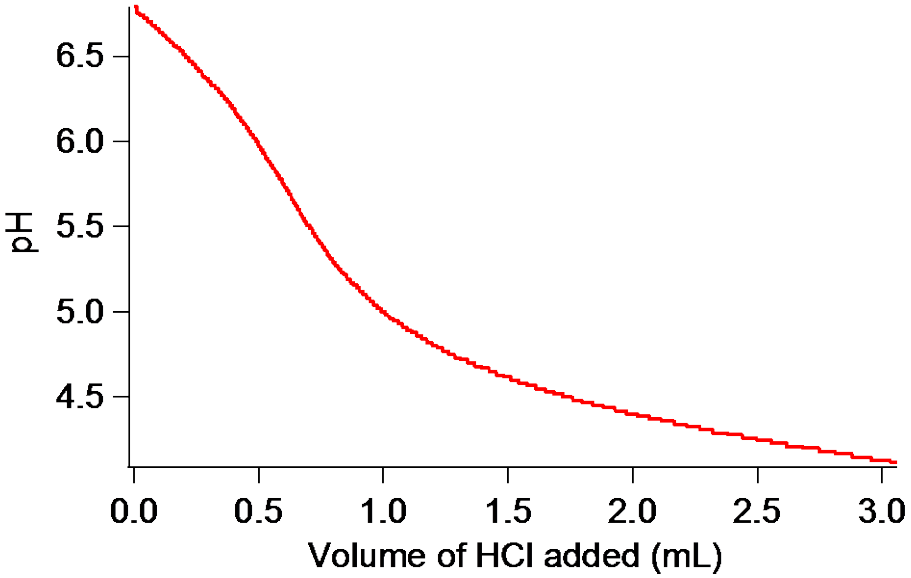

Figure 2.12. Titration of Complex 1 by HCl in water. Midpoint analysis where $pH=pK_a$ leads to a pK_a for complex 1-H^+ ~6.5. This was determined by approximation of the midpoint.

2.4.14 Electrochemical investigations of complexes 1, 1-H^+, 2, 3-M (M=Cd, Mn, Zn) and 4

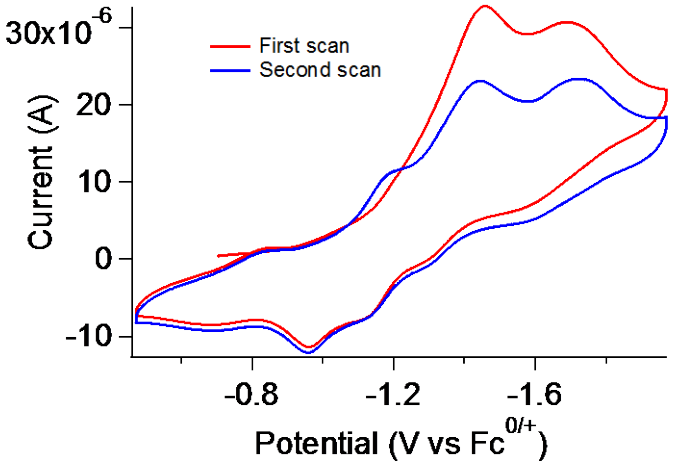

Figure 2.13 First and second scans at 300mV/s of 1.5mM 1 in 0.2M [^{n}Bu$_4$N][PF$_6$] in CH$_3$CN.

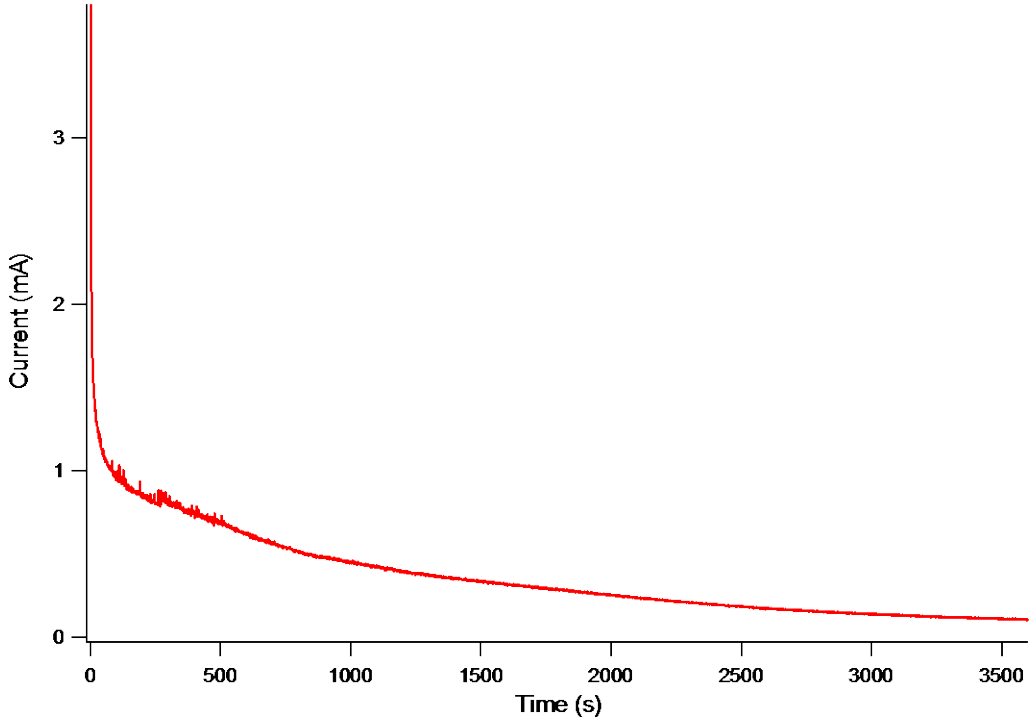

Figure 2.14. Bulk electrolysis of 0.26 mM Complex 2 in 0.15M [^{n}Bu$_4$N][PF$_6$] in CH$_3$CN. 1.323 C were passed in this hour experiment.

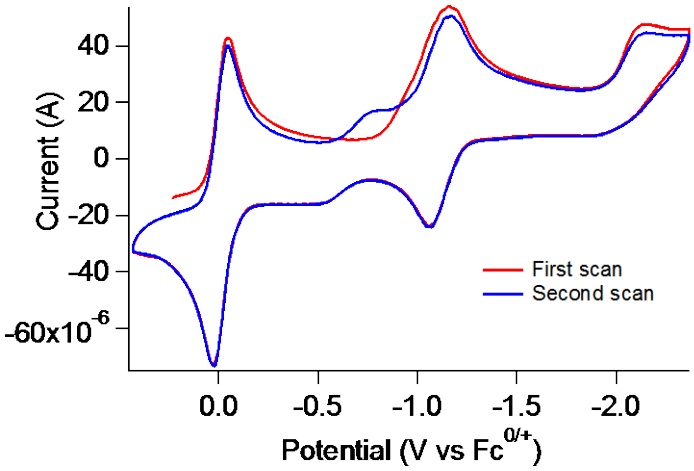

Figure 2.15. First and second scans at 300mV/s of 1.5mM **2** in 0.2M [^{n}Bu$_4$N][PF$_6$] in CH$_3$CN.

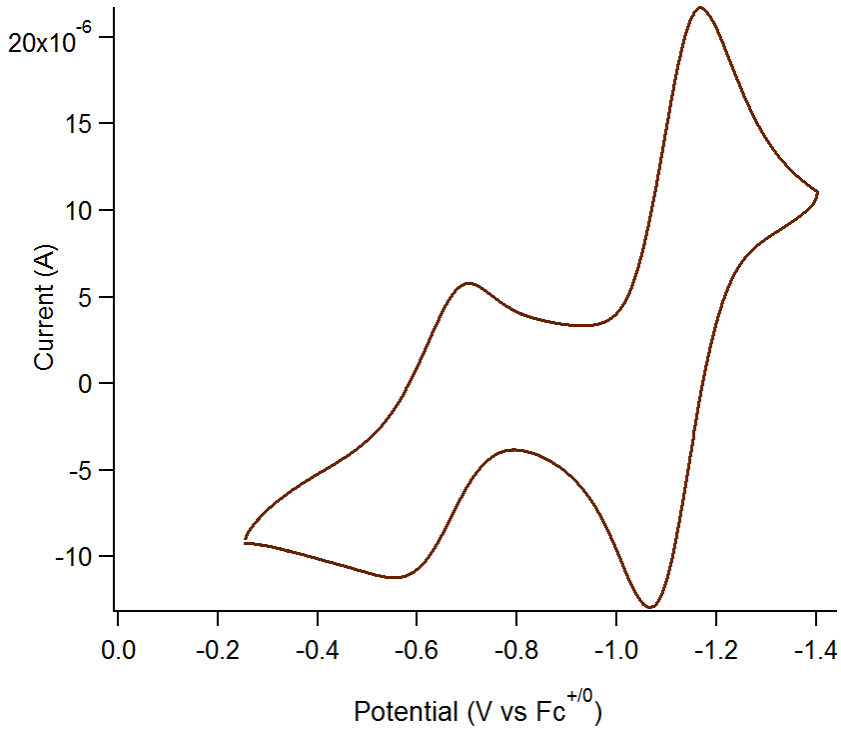

Figure 2.16. CV of [(DO)$_2$en(Im^{Me})CoZnBr$_2$] in 0.2M [^{n}Bu$_4$N][PF$_6$] in CH$_3$CN, 100mV/s

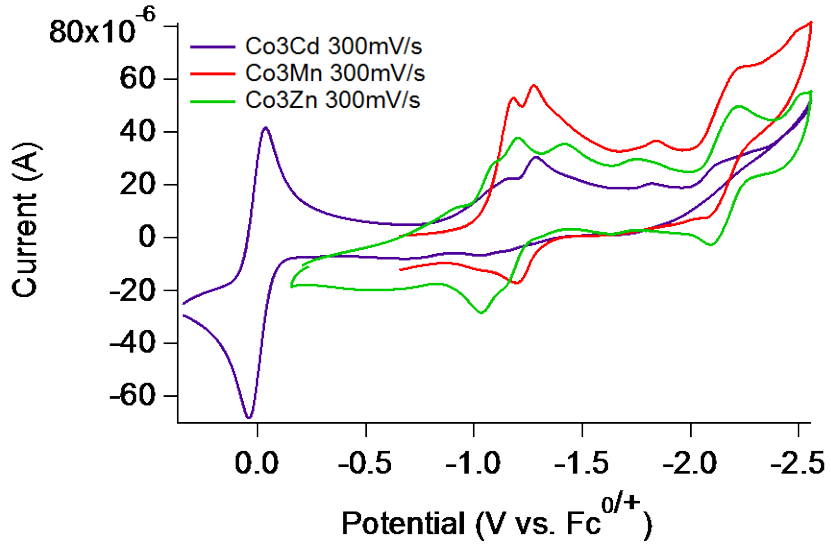

Figure 2.17: CVs of 0.7mM 3-Mn, 3-Zn and 3-Cd in 0.2M [$^{n}Bu_4N$][PF_6] in CH_3CN.

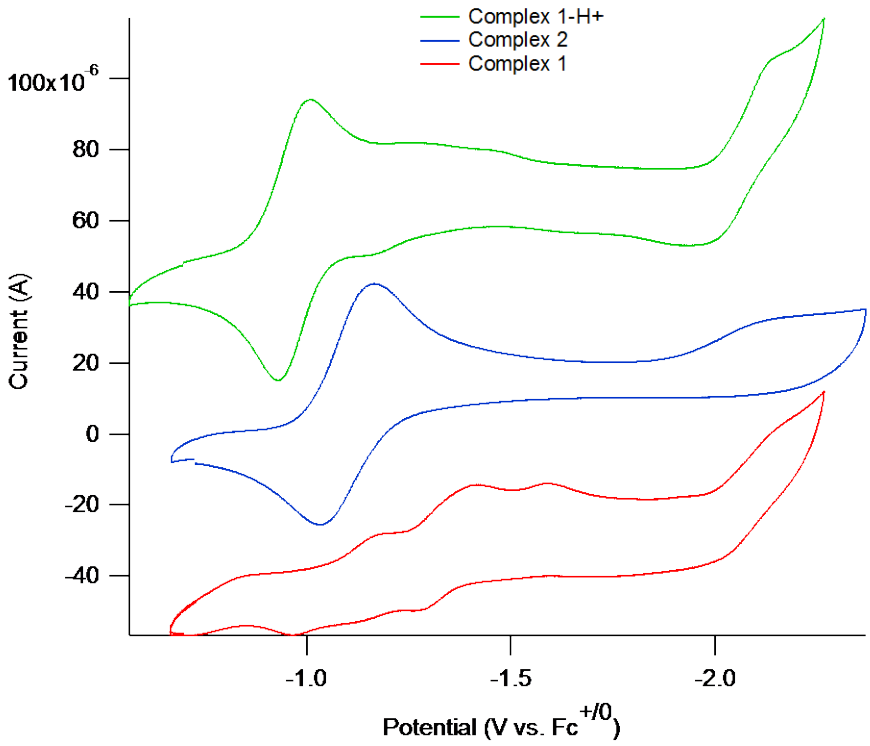

Figure 2.18 Complexes 1, 1-H^+ and 2 scanned to more negative potentials (presumably revealing the Co(I/0) couple; 100mV/s; 0.2 M [$^{n}Bu_4N$][PF_6] in CH_3CN.

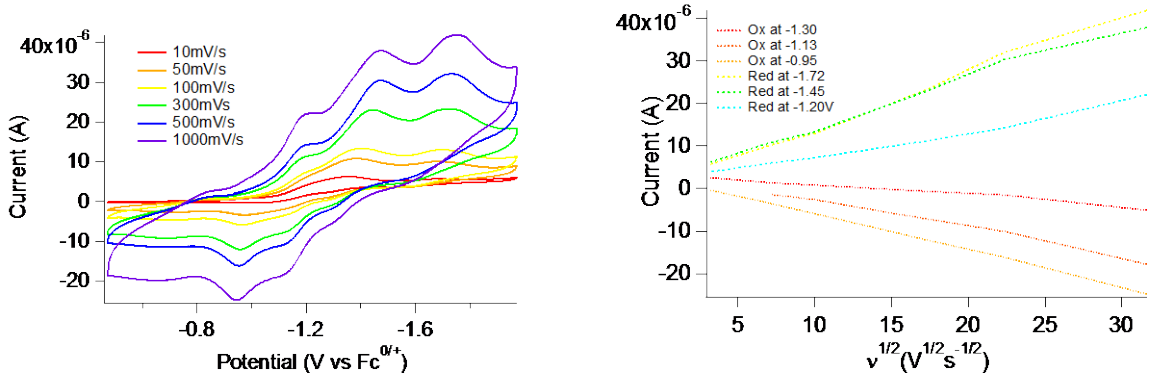

Figure 2.19. Scan rate dependence (second scan shown) of 1.5mM complex 1 in 0.2M [^{n}Bu$_4$N][PF$_6$] in CH$_3$CN.

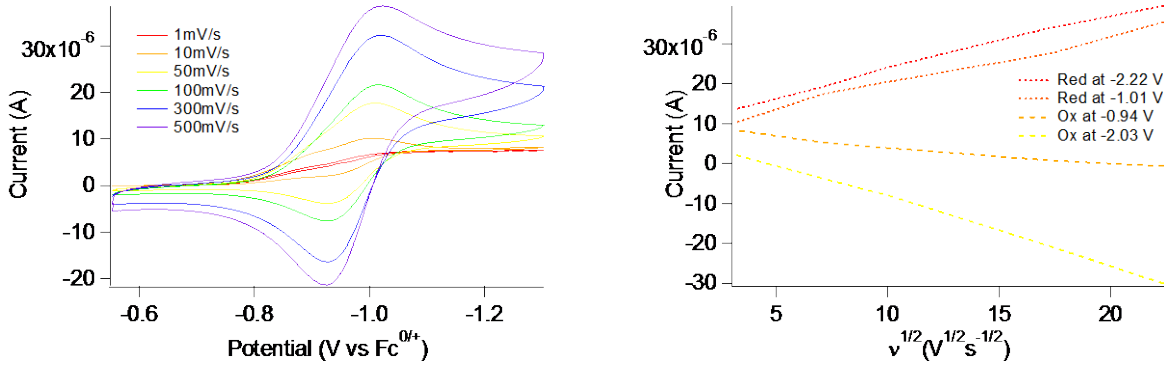

Figure 2.20. Scan rate dependence of 1.5mM 1-H$^+$ in 0.2M [^{n}Bu$_4$N][PF$_6$] in CH$_3$CN.

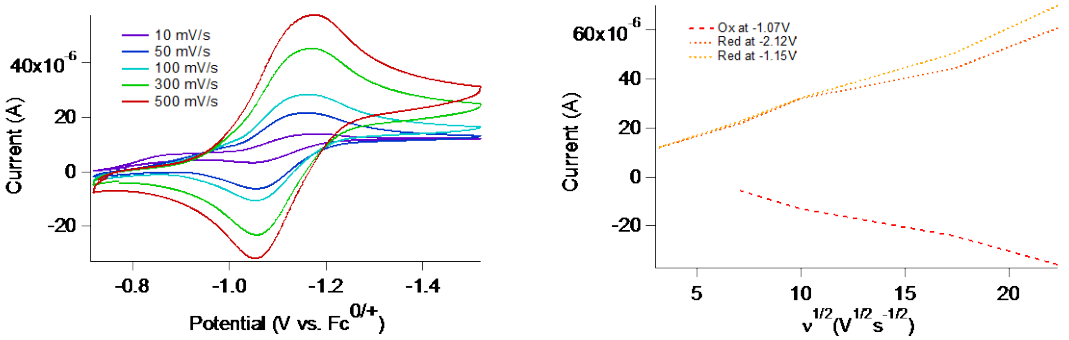

Figure 2.21: Scan rate dependence of 1.5mM 2 in 0.2M [^{n}Bu$_4$N][PF$_6$] in CH$_3$CN.

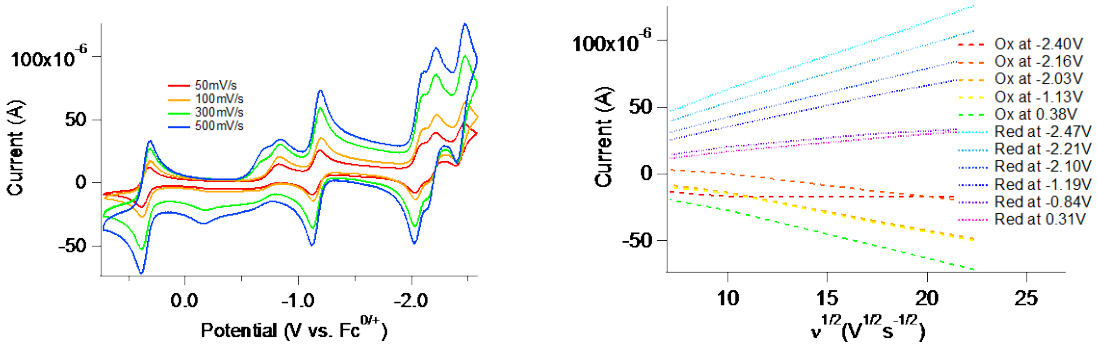

Figure 2.22. Scan rate dependence of 1.0mM 4 in 0.2M [$^{n}Bu_4N$][PF_6] in CH_3CN.

2.4.15 Stability of complex 1 in CF_3COOH by ^1H NMR

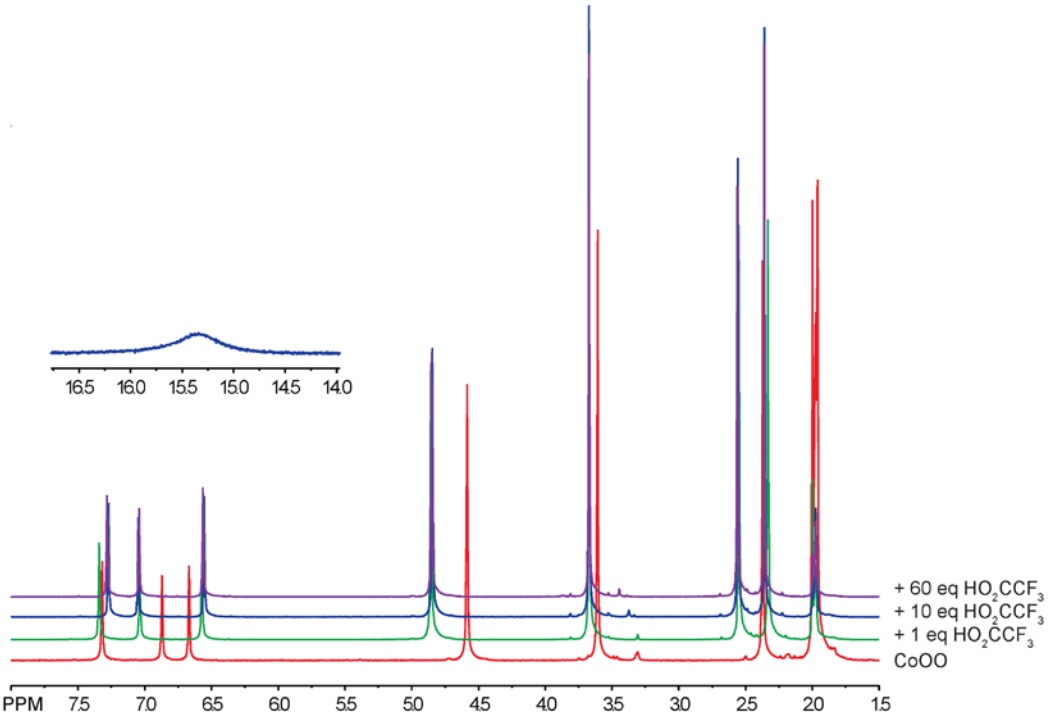

Figure 2.23: ^1H NMR of Complex 1 with equivalents of CF_3COOH in CD_3CN (499MHz)

2.4.16 Investigations of proton reduction by complexes 1,2, and 4 by $TEAH^+$ and $^{Me}ImH^+$

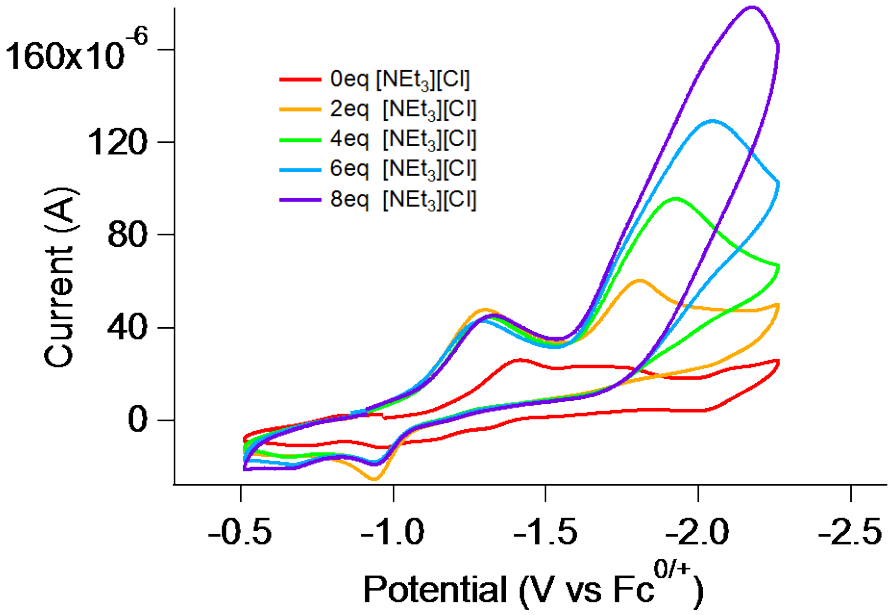

Figure 2.24: 1.0mM complex 1 with increasing equivalents of $[NEt_3H][Cl]$ (4.0mM to 16mM) at 300mV/s in 0.2M $[^nBu_4N][PF_6]$ in CH_3CN; a shift in the i_{cat} is observed upon additional acid equivalents.

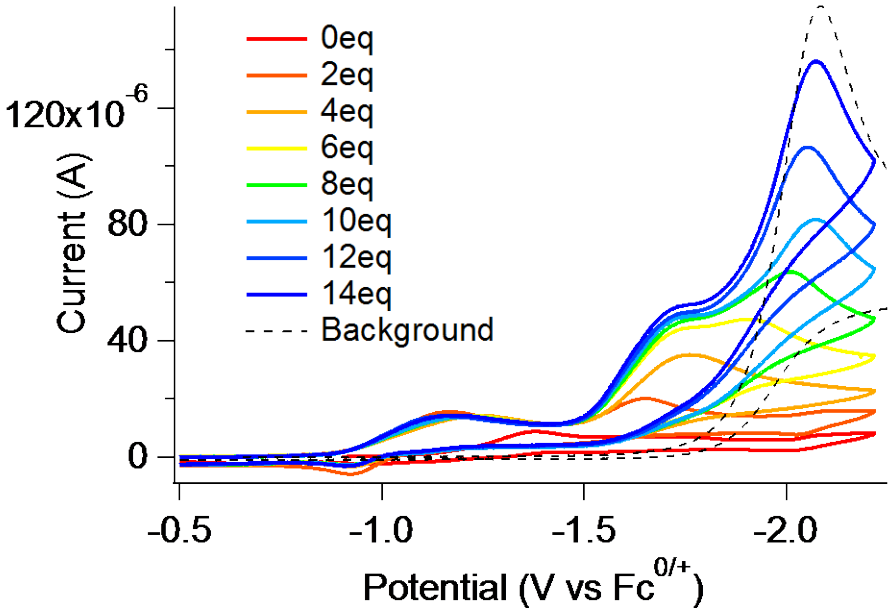

Figure 2.25. 0.75mM complex 1 with increasing equivalents of $[NEt_3H][BPh_4]$ (2-14 eq or 1.5-10.5mM) at 50mV/s in 0.2M $[^nBu_4N][PF_6]$ in CH_3CN; background with acid at 10.5mM $[NEt_3H][BPh_4]$.

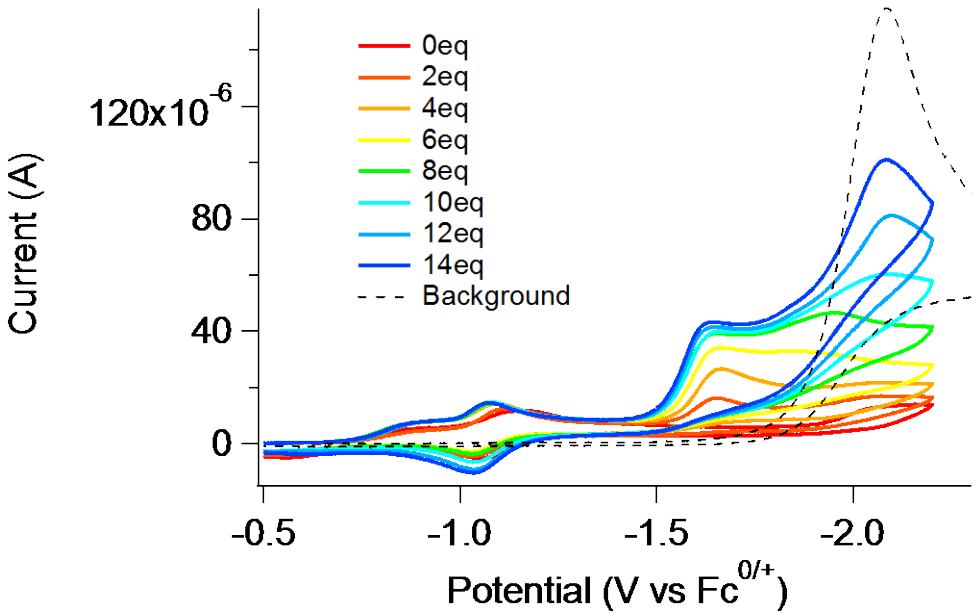

Figure 2.26. 0.75mM complex 2 with increasing equivalents of $[NEt_3H][BPh_4]$ (2-14 eq or 1.5-10.5mM) at 50mV/s in 0.2M $[^nBu_4N][PF_6]$ in CH_3CN; background with acid at 10.5mM $[NEt_3H][BPh_4]$.

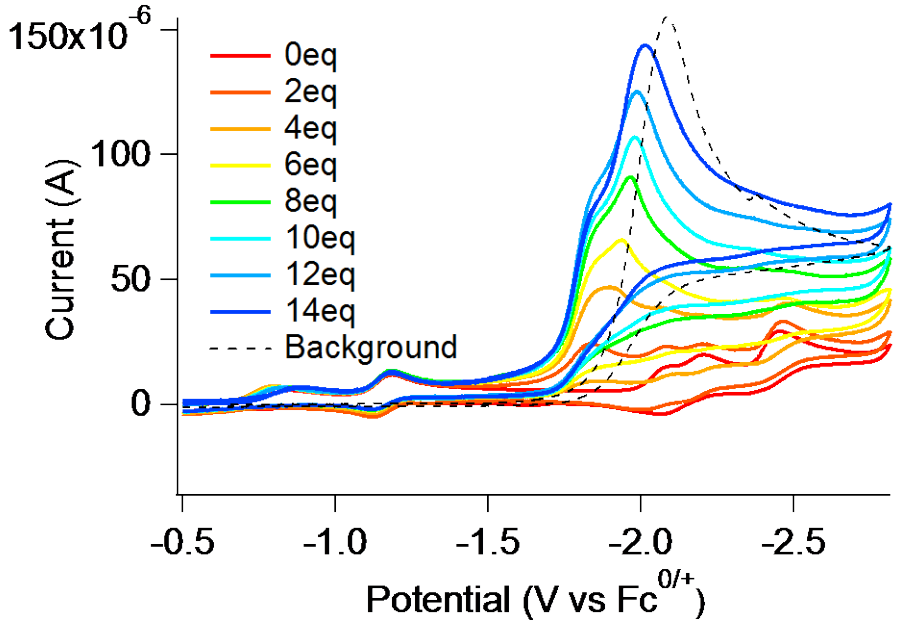

Figure 2.27. 0.75mM complex 4 with increasing equivalents of $[NEt_3H][BPh_4]$ (2-14 eq or 1.5-10.5mM) at 50mV/s in 0.2M $[^nBu_4N][PF_6]$ in CH_3CN; background with acid at 10.5mM $[NEt_3H][BPh_4]$.

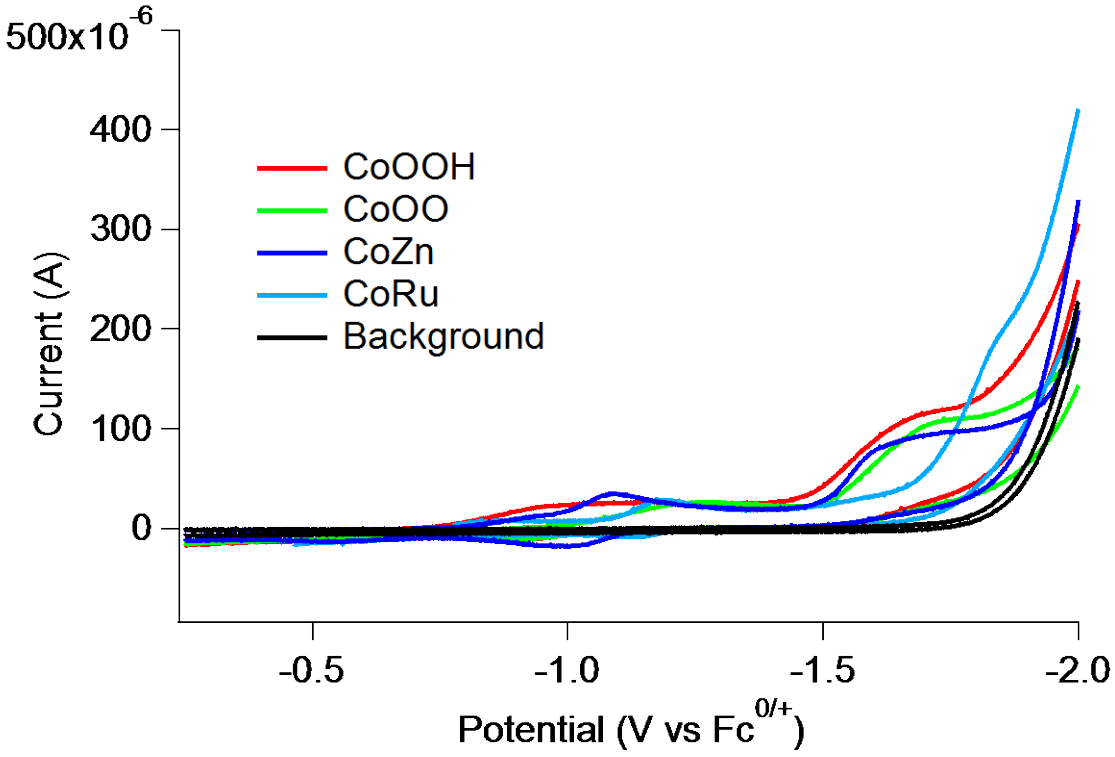

Figure 2.28. Comparison of 0.75 mM catalyst with 60 equivalents of $[NEt_3H][BPh_4]$ at 300 mV/s in 0.2M $[^nBu_4N][PF_6]$ in CH_3CN.

2.4.16 Electrolyses and calculation of Faradic efficiencies of complexes 1, 1-H^+,2, and 4

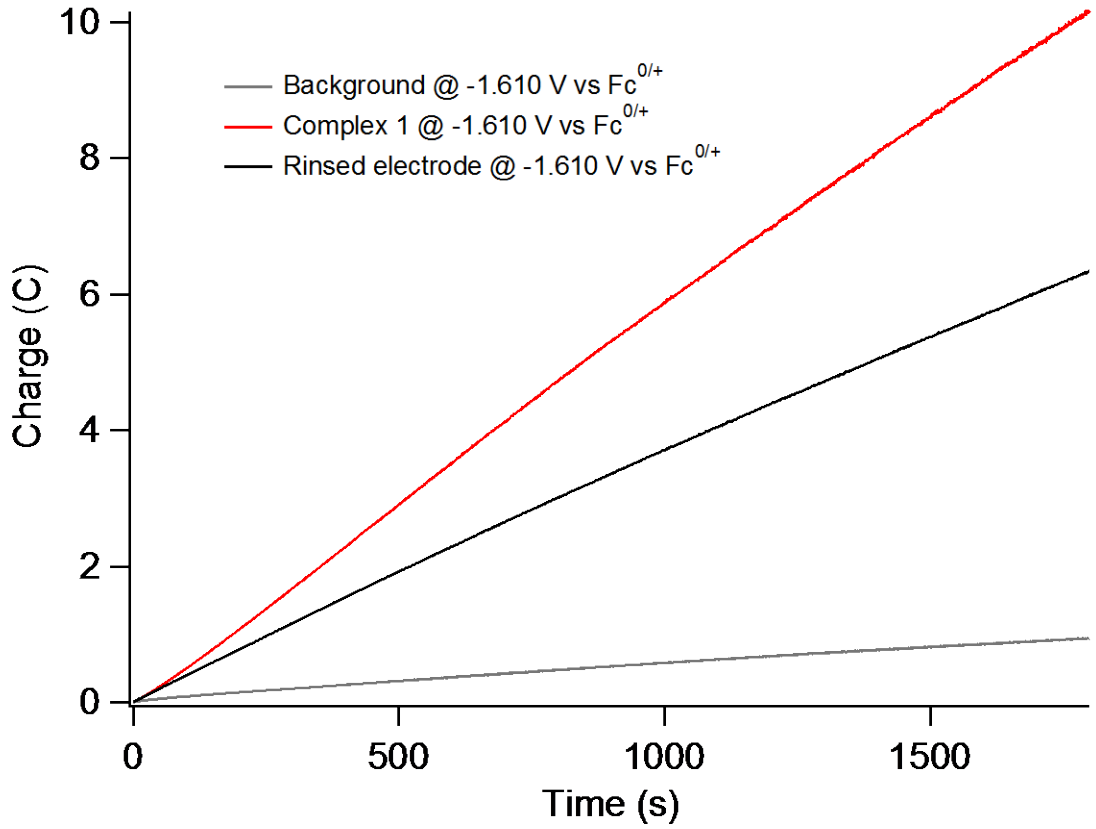

Figure 2.29. Current versus time from a 30 min electrolysis with 0.25 mM complex 1, 25 mM $[NEt_3H][BPh_4]$ in 0.1 M $[^nBu_4N][PF_6]$ in CH_3CN.

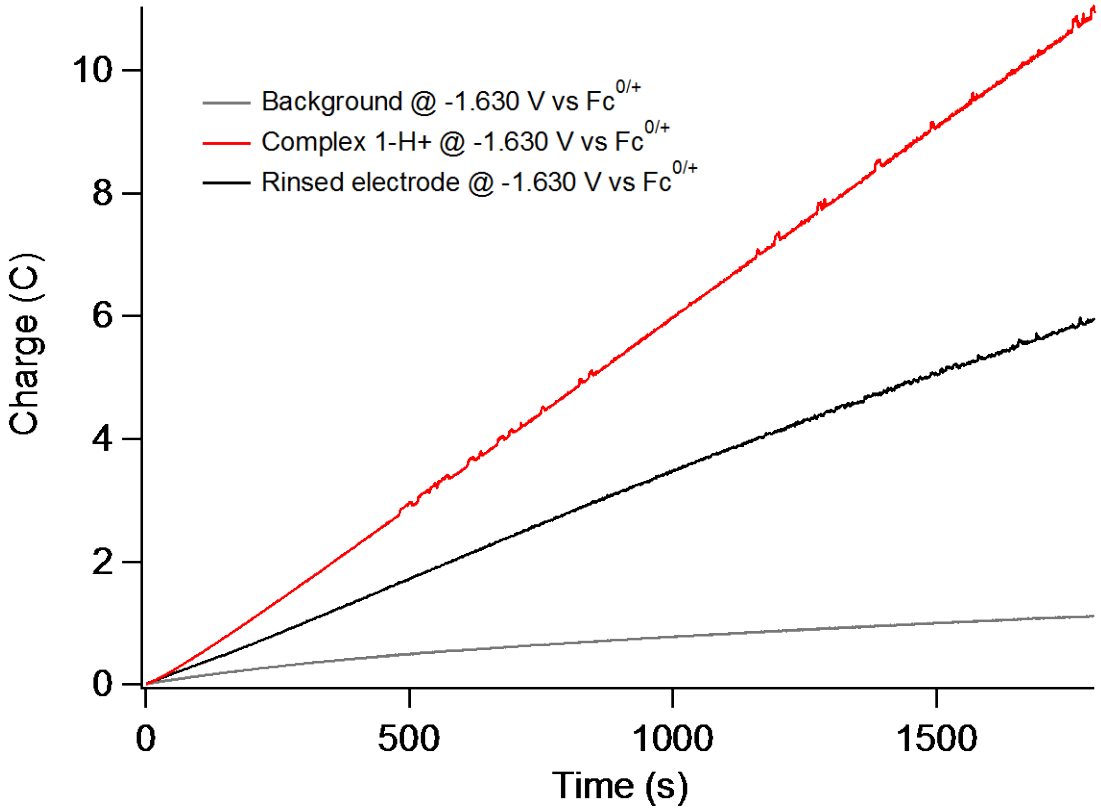

Figure 2.30. Current versus time from a 30 min electrolysis with 0.25 mM complex **1-H$^+$**, 25 mM [NEt_3H][BPh_4] in 0.1 M [$^nBu_4N$][PF_6] in CH_3CN.

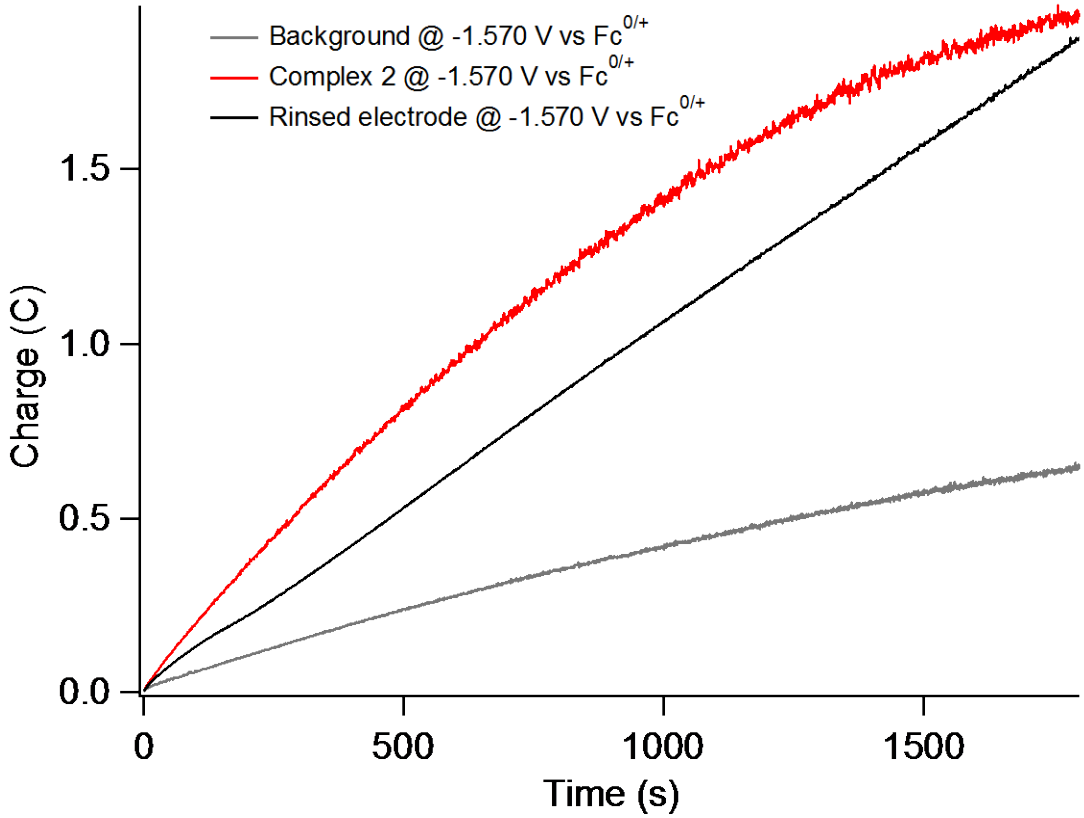

Figure 2.31. Current versus time from a 30 min electrolysis with 0.25 mM complex 2, 25 mM $[NEt_3H][BPh_4]$ in 0.1 M $[^nBu_4N][PF_6]$ in CH_3CN.

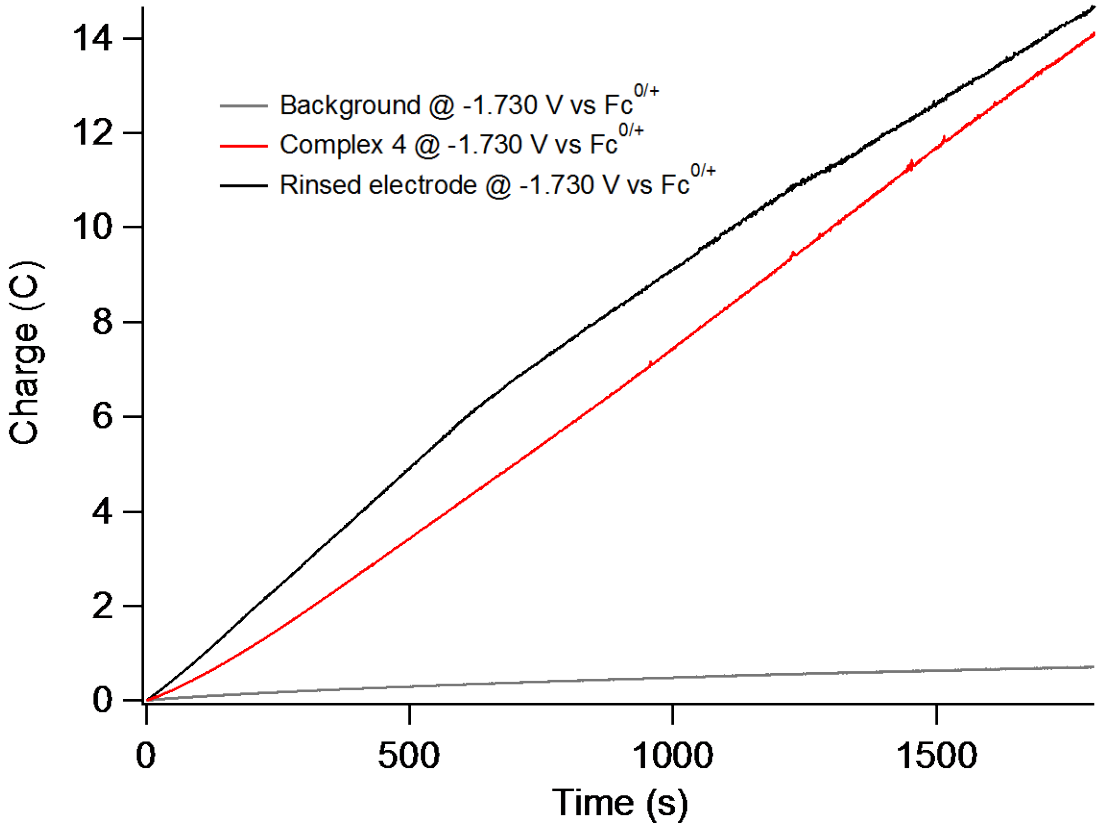

Figure 2.32. Current versus time from a 30 min electrolysis with 0.25 mM complex 4, 25 mM $[NEt_3H][BPh_4]$ in 0.1 M $[^nBu_4N][PF_6]$ in CH_3CN.

Table 2.3.: Moles of hydrogen and charge passed from background with acid, catalysts and rinsed electrode tests from bulk electrolysis experiments. The same electrode was used for the data in each row, however in each row was used a different electrode.

Complex	Charge (C) passed by background with acid	Charge (C) passed by electrolysis with catalyst	Charge (C) passed by rinsed electrode	Moles of hydrogen from background with acid	Moles of hydrogen from catalyst run	Moles of hydrogen from rinsed electrode	Potential(V vs $Fc^{0/+}$)
4	1.04	12.67	16.34	4.5E-6	5.3E-5	7.2E-5	-1.73
1	1.15	10.2	6.70	3.7E-6	3.3E-5	2.9E-5	-1.61
2	0.86	2.7	2.00	1.8E-6	3.8E-6	8.3E-6	-1.57
1-H$^+$	1.61	10.4	6.2	6.3E-6	3.9E-5	1.6E-5	-1.63

Faradaic efficiency was calculated from the following equation:

$$FE = \left[\frac{(moles\ H_2\ from\ catalyst\ run - moles\ of\ H_2\ from\ background) * 2 * 96485}{charge\ passed\ by\ electrolysis\ with\ acid - charge\ passed\ by\ background\ acid\ reduction} \right] * 100$$

2.4.17 X-ray crystallography tables

Table 2.4. Crystal data and structure refinement for Complex 1

Identification code	dh_152b_0ma	
Empirical formula	C20 H34 Cl Co N8 O7 S	
Formula weight	624.99	
Temperature	100(2) K	
Wavelength	0.71073 Å	
Crystal system	Monoclinic	
Space group	P n	
Unit cell dimensions	a = 6.8158(16) Å	α = 90°.
	b = 12.780(3) Å	β = 92.125(14)°.
	c = 15.038(3) Å	γ = 90°.
Volume	1309.0(5) $Å^3$	
Z	2	
Density (calculated)	1.586 Mg/m^3	
Absorption coefficient	0.895 mm^{-1}	
F(000)	652	
Crystal size	0.12 x 0.08 x 0.01 mm^3	
Theta range for data collection	1.59 to 25.42°.	
Index ranges	-8<=h<=8, -15<=k<=15, -18<=l<=18	
Reflections collected	32970	
Independent reflections	4775 [R(int) = 0.1065]	
Completeness to theta = 25.00°	100.0 %	
Max. and min. transmission	0.9911 and 0.9002	
Refinement method	Full-matrix least-squares on F^2	
Data / restraints / parameters	4775 / 2 / 351	
Goodness-of-fit on F^2	1.007	

Final R indices [I>2sigma(I)]	R1 = 0.0434, wR2 = 0.0611
R indices (all data)	R1 = 0.0762, wR2 = 0.0691
Absolute structure parameter	0.005(15)
Largest diff. peak and hole	0.350 and -0.415 e.Å^{-3}

Table 2.5. Crystal data and structure refinement for Complex 1-H^{+}

Identification code	twin5	
Empirical formula	C18 H29 Cl2 Co N8 O10	
Formula weight	647.32	
Temperature	100 K	
Wavelength	0.71073 Å	
Crystal system	Monoclinic	
Space group	P 21/n	
Unit cell dimensions	a = 14.714(2) Å	α = 90°.
	b = 11.4270(18) Å	β = 92.610(11)°.
	c = 15.237(3) Å	γ = 90°.
Volume	2559.2(8) Å^3	
Z	4	
Density (calculated)	1.680 Mg/m^3	
Absorption coefficient	0.949 mm^{-1}	
F(000)	1336	
Crystal size	0.20 x 0.10 x 0.07 mm^3	
Theta range for data collection	2.23 to 25.70°.	
Index ranges	-17<=h<=17, -13<=k<=13, 0<=l<=18	
Reflections collected	8597	
Independent reflections	9118 [R(int) = 0.1198]	
Completeness to theta = 25.00°	96.6 %	
Max. and min. transmission	0.9365 and 0.8329	
Refinement method	Full-matrix least-squares on F^2	
Data / restraints / parameters	9118 / 235 / 378	
Goodness-of-fit on F^2	1.094	
Final R indices [I>2sigma(I)]	R1 = 0.1287, wR2 = 0.3120	
R indices (all data)	R1 = 0.1723, wR2 = 0.3501	
Largest diff. peak and hole	2.270 and -1.410 e.Å^{-3}	

Table 2.6. Crystal data and structure refinement for Complex 2

Identification code	dh_160_0ma	
Empirical formula	C18 H28 Br2 Cl Co N8 O6 Zn	
Formula weight	772.05	
Temperature	100(2) K	
Wavelength	0.71073 Å	
Crystal system	Monoclinic	
Space group	P c	
Unit cell dimensions	a = 17.567(3) Å	α = 90°.
	b = 10.0243(16) Å	β = 102.334(9)°.
	c = 15.749(3) Å	γ = 90°.
Volume	2709.3(8) $Å^3$	
Z	4	
Density (calculated)	1.893 Mg/m^3	
Absorption coefficient	4.595 mm^{-1}	
F(000)	1536	
Crystal size	0.10 x 0.05 x 0.02 mm^3	
Theta range for data collection	2.03 to 28.39°.	
Index ranges	-23<=h<=23, -13<=k<=13, -21<=l<=21	
Reflections collected	123719	
Independent reflections	13533 [R(int) = 0.0536]	
Completeness to theta = 25.00°	100.0 %	
Max. and min. transmission	0.9137 and 0.6565	
Refinement method	Full-matrix least-squares on F^2	
Data / restraints / parameters	13533 / 83 / 741	
Goodness-of-fit on F^2	1.013	
Final R indices [I>2sigma(I)]	R1 = 0.0337, wR2 = 0.0621	
R indices (all data)	R1 = 0.0468, wR2 = 0.0666	
Absolute structure parameter	0.102(5)	
Largest diff. peak and hole	1.256 and -1.103 $e.Å^{-3}$	

Table 2.7. Crystal data and structure refinement for Complex 3-Zn

Identification code	dh_177_0ma	
Empirical formula	C54 H96 Cl5 Co3 N24 O32 Zn	
Formula weight	2012.96	
Temperature	292(2) K	
Wavelength	0.71073 Å	
Crystal system	Trigonal	
Space group	R -3 c	
Unit cell dimensions	a = 28.732(3) Å	α = 90°.
	b = 28.732(3) Å	β = 90°.
	c = 17.5558(16) Å	γ = 120°.
Volume	12551.0(19) $Å^3$	
Z	6	
Density (calculated)	1.598 Mg/m^3	
Absorption coefficient	1.122 mm^{-1}	
F(000)	6240	
Crystal size	0.10 x 0.10 x 0.02 mm^3	
Theta range for data collection	2.46 to 25.57°.	
Index ranges	-34<=h<=34, -34<=k<=34, -21<=l<=21	
Reflections collected	133666	
Independent reflections	2588 [R(int) = 0.1365]	
Completeness to theta = 25.00°	98.9 %	
Max. and min. transmission	0.9779 and 0.8961	
Refinement method	Full-matrix least-squares on F^2	
Data / restraints / parameters	2588 / 90 / 260	
Goodness-of-fit on F^2	1.054	
Final R indices [I>2sigma(I)]	R1 = 0.0442, wR2 = 0.1081	
R indices (all data)	R1 = 0.0847, wR2 = 0.1394	
Largest diff. peak and hole	0.338 and -0.349 $e.Å^{-3}$	

Table 2.8. Crystal data and structure refinement for Complex 3-Mn

Identification code	dh_183_0ma	
Empirical formula	C54 H96 Cl5 Co3 Mn N24 O32	
Formula weight	2002.53	
Temperature	100(2) K	
Wavelength	0.71073 Å	
Crystal system	Trigonal	
Space group	R -3 c	
Unit cell dimensions	a = 28.810(3) Å	α = 90°.
	b = 28.810(3) Å	β = 90°.
	c = 16.9308(19) Å	γ = 120°.
Volume	12170(2) $Å^3$	
Z	6	
Density (calculated)	1.639 Mg/m^3	
Absorption coefficient	1.017 mm^{-1}	
F(000)	6210	
Crystal size	0.10 x 0.10 x 0.02 mm^3	
Theta range for data collection	2.45 to 28.40°.	
Index ranges	-38<=h<=38, -38<=k<=38, -22<=l<=22	
Reflections collected	141055	
Independent reflections	3409 [R(int) = 0.1074]	
Completeness to theta = 25.00°	100.0 %	
Max. and min. transmission	0.9799 and 0.9051	
Refinement method	Full-matrix least-squares on F^2	
Data / restraints / parameters	3409 / 83 / 261	
Goodness-of-fit on F^2	1.065	
Final R indices [I>2sigma(I)]	R1 = 0.0529, wR2 = 0.1252	
R indices (all data)	R1 = 0.0851, wR2 = 0.1417	
Largest diff. peak and hole	0.424 and -0.483 $e.Å^{-3}$	

Table 2.9. Crystal data and structure refinement for Complex 3-Cd

Identification code	twin4a	
Empirical formula	C54 H96 Cd Cl5 Co3 N24 O32	
Formula weight	2059.99	
Temperature	100(2) K	
Wavelength	0.71073 Å	
Crystal system	Trigonal	
Space group	R -3 c	
Unit cell dimensions	a = 28.981(3) Å	α = 90°.
	b = 28.981(3) Å	β = 90°.
	c = 16.838(4) Å	γ = 120°.
Volume	12247(3) $Å^3$	
Z	6	
Density (calculated)	1.676 Mg/m^3	
Absorption coefficient	1.117 mm^{-1}	
F(000)	6348	
Crystal size	0.10 x 0.10 x 0.02 mm^3	
Theta range for data collection	2.43 to 28.46°.	
Index ranges	-38<=h<=0, -10<=k<=38, -22<=l<=20	
Reflections collected	9984	
Independent reflections	3421 [R(int) = 0.0746]	
Completeness to theta = 25.00°	100.0 %	
Max. and min. transmission	0.9780 and 0.8965	
Refinement method	Full-matrix least-squares on F^2	
Data / restraints / parameters	3421 / 83 / 261	
Goodness-of-fit on F^2	1.190	
Final R indices [I>2sigma(I)]	R1 = 0.0789, wR2 = 0.1311	
R indices (all data)	R1 = 0.1306, wR2 = 0.1474	
Largest diff. peak and hole	0.505 and -0.430 $e.Å^{-3}$	

Table 2.10. Crystal data and structure refinement for Complex 4

Identification code	dh2_135c_0ma	
Empirical formula	C616 H716 Co16 F288 N196 O32 P48 Ru16	
Formula weight	20896.41	
Temperature	100(2) K	
Wavelength	0.71073 Å	
Crystal system	Tetragonal	
Space group	I 4_1/a	
Unit cell dimensions	a = 40.556(5) Å	α = 90.000°.
	b = 40.556(5) Å	β = 90.000°.
	c = 12.276(5) Å	γ = 90.000°.
Volume	20191(9) $Å^3$	
Z	1	
Density (calculated)	1.719 Mg/m^3	
Absorption coefficient	0.839 mm^{-1}	
F(000)	10488	
Crystal size	0.10 x 0.03 x 0.03 mm^3	
Theta range for data collection	2.00 to 25.49°.	
Index ranges	-48<=h<=49, -49<=k<=45, -14<=l<=14	
Reflections collected	90430	
Independent reflections	9314 [R(int) = 0.3615]	
Completeness to theta = 25.00°	99.4 %	
Max. and min. transmission	0.9753 and 0.9208	
Refinement method	Full-matrix least-squares on F^2	
Data / restraints / parameters	9314 / 546 / 791	
Goodness-of-fit on F^2	0.991	
Final R indices [I>2sigma(I)]	R1 = 0.0861, wR2 = 0.1621	
R indices (all data)	R1 = 0.2700, wR2 = 0.2331	
Largest diff. peak and hole	1.144 and -0.868 $e.Å^{-3}$	

Table 2.11. Crystal data and structure refinement for $[(DO)_2en(Im^{Me})_2CoNa][PF_6]_2$

Identification code	dh2_73_0ma	
Empirical formula	C18 H28 Co F12 N8 Na O2 P2	
Formula weight	760.34	
Temperature	100(2) K	
Wavelength	0.71073 Å	
Crystal system	Orthorhombic	
Space group	P b c n	
Unit cell dimensions	a = 8.6942(9) Å	α = 90°.
	b = 22.063(2) Å	β = 90°.
	c = 14.9541(15) Å	γ = 90°.
Volume	2868.4(5) $Å^3$	
Z	4	
Density (calculated)	1.761 Mg/m^3	
Absorption coefficient	0.838 mm^{-1}	
F(000)	1536	
Crystal size	0.20 x 0.09 x 0.05 mm^3	
Theta range for data collection	2.29 to 28.51°.	
Index ranges	-11<=h<=11, -29<=k<=29, -20<=l<=19	
Reflections collected	110617	
Independent reflections	3538 [R(int) = 0.1143]	
Completeness to theta = 25.00°	97.3 %	
Max. and min. transmission	0.9593 and 0.8503	
Refinement method	Full-matrix least-squares on F^2	
Data / restraints / parameters	3538 / 0 / 204	
Goodness-of-fit on F^2	1.129	
Final R indices [I>2sigma(I)]	R1 = 0.0692, wR2 = 0.1719	
R indices (all data)	R1 = 0.0859, wR2 = 0.1849	
Extinction coefficient	0.0022(5)	
Largest diff. peak and hole	1.183 and -1.206 $e.Å^{-3}$	

Table 2.12. Crystal data and structure refinement for $[(DO)_2en(Im^{Me})_2CoNa\text{-}15crown5][BPh_4]_2$

Identification code	twin5	
Empirical formula	C76 H88 B2 Co N8 Na O7	
Formula weight	1329.08	
Temperature	100(2) K	
Wavelength	0.71073 Å	
Crystal system	Triclinic	
Space group	P 1	
Unit cell dimensions	a = 11.8905(14) Å	α = 72.344(5)°.
	b = 12.4560(16) Å	β = 66.193(4)°.
	c = 13.6113(17) Å	γ = 73.679(4)°.
Volume	1728.2(4) $Å^3$	
Z	1	
Density (calculated)	1.277 Mg/m^3	
Absorption coefficient	0.315 mm^{-1}	
F(000)	704	
Crystal size	0.08 x 0.03 x 0.03 mm^3	
Theta range for data collection	2.05 to 28.37°.	
Index ranges	-15<=h<=15, -16<=k<=16, -18<=l<=18	
Reflections collected	33862	
Independent reflections	33863 [R(int) = 0.1023]	
Completeness to theta = 25.00°	100.0 %	
Max. and min. transmission	0.9906 and 0.9752	
Refinement method	Full-matrix least-squares on F^2	
Data / restraints / parameters	33863 / 21 / 865	
Goodness-of-fit on F^2	0.994	
Final R indices [I>2sigma(I)]	R1 = 0.0677, wR2 = 0.1102	
R indices (all data)	R1 = 0.1308, wR2 = 0.1303	
Absolute structure parameter	0.036(12)	
Largest diff. peak and hole	0.520 and -0.521 $e.Å^{-3}$	

Table 2.13. Crystal data and structure refinement for $[((DO)_2en(Im^{Me})_2Co)_2Zn(HOMe)][ClO_4]_4$

Identification code	dh_177b_0m	
Empirical formula	C37 H62 Cl4 Co2 N16 O22 Zn	
Formula weight	1408.06	
Temperature	100(2) K	
Wavelength	0.71073 Å	
Crystal system	Triclinic	
Space group	P -1	
Unit cell dimensions	a = 13.3205(16) Å	α = 70.715(6)°.
	b = 15.0242(18) Å	β = 76.405(7)°.
	c = 17.218(2) Å	γ = 67.308(6)°.
Volume	2977.7(6) $Å^3$	
Z	2	
Density (calculated)	1.570 Mg/m^3	
Absorption coefficient	1.215 mm^{-1}	
F(000)	1448	
Crystal size	0.22 x 0.12 x 0.05 mm^3	
Theta range for data collection	1.84 to 28.62°.	
Index ranges	-17<=h<=17, -20<=k<=19, -23<=l<=23	
Reflections collected	125072	
Independent reflections	14926 [R(int) = 0.0424]	
Completeness to theta = 25.00°	99.9 %	
Max. and min. transmission	0.9418 and 0.7759	
Refinement method	Full-matrix least-squares on F^2	
Data / restraints / parameters	14926 / 87 / 822	
Goodness-of-fit on F^2	1.041	
Final R indices [I>2sigma(I)]	R1 = 0.0473, wR2 = 0.1069	
R indices (all data)	R1 = 0.0649, wR2 = 0.1138	
Largest diff. peak and hole	2.104 and -0.946 e.$Å^{-3}$	

Table 2.14. Crystal data and structure refinement for $(DO)_2enCo(Im^{Me})ZnBr_2$ $(Cr(bn)_2)$

Empirical formula	C30 H42 Br2 Co Cr N6 O3 Zn	
Formula weight	870.82	
Temperature	100(2) K	
Wavelength	0.71073 Å	
Crystal system	Monoclinic	
Space group	P 2_1/a	
Unit cell dimensions	a = 16.8819(12) Å	α = 90°.
	b = 13.0386(10) Å	β = 118.699(5)°.
	c = 17.5538(16) Å	γ = 90°.
Volume	3389.2(5) $Å^3$	
Z	4	
Density (calculated)	1.707 Mg/m^3	
Absorption coefficient	3.899 mm^{-1}	
F(000)	1756	
Crystal size	0.02 x 0.01 x 0.01 mm^3	
Theta range for data collection	1.32 to 25.49°.	
Index ranges	-20<=h<=20, -15<=k<=15, -21<=l<=21	
Reflections collected	62702	
Independent reflections	6240 [R(int) = 0.2299]	
Completeness to theta = 25.00°	99.9 %	
Max. and min. transmission	0.9621 and 0.9261	
Refinement method	Full-matrix least-squares on F^2	
Data / restraints / parameters	6240 / 223 / 402	
Goodness-of-fit on F^2	1.031	
Final R indices [I>2sigma(I)]	R1 = 0.0801, wR2 = 0.1777	
R indices (all data)	R1 = 0.1731, wR2 = 0.2221	
Largest diff. peak and hole	1.366 and -1.557 $e.Å^{-3}$	

Table 2.15. Crystal data and structure refinement for $(DO)_2enCo(Im^{Me})ZnBr_2$

Empirical formula	C18 H28 Br2 Co N8 O2 Zn	
Formula weight	672.60	
Temperature	100(2) K	
Wavelength	0.71073 Å	
Crystal system	Monoclinic	
Space group	P 2_1/n	
Unit cell dimensions	a = 10.5472(6) Å	α = 90°.
	b = 12.2166(6) Å	β = 100.534(4)°.
	c = 19.9895(14) Å	γ = 90°.
Volume	2532.3(3) $Å^3$	
Z	4	
Density (calculated)	1.764 Mg/m^3	
Absorption coefficient	4.789 mm^{-1}	
F(000)	1340	
Crystal size	0.05 x 0.01 x 0.01 mm^3	
Theta range for data collection	1.96 to 25.37°.	
Index ranges	-12<=h<=12, -14<=k<=14, -24<=l<=24	
Reflections collected	36574	
Independent reflections	4638 [R(int) = 0.0752]	
Completeness to theta = 25.00°	100.0 %	
Max. and min. transmission	0.9537 and 0.7957	
Refinement method	Full-matrix least-squares on F^2	
Data / restraints / parameters	4638 / 15 / 312	
Goodness-of-fit on F^2	1.001	
Final R indices [I>2sigma(I)]	R1 = 0.0396, wR2 = 0.0712	
R indices (all data)	R1 = 0.0751, wR2 = 0.0809	
Largest diff. peak and hole	0.906 and -0.752 $e.Å^{-3}$	

2.5 References

1. Henckel, D. A.; Lin, Y. F.; McCormick, T. M.; Kaminsky, W.; Cossairt, B. M., A doubly deprotonated diimine dioximate metalloligand as a synthon for multimetallic complex assembly. *Dalton Transactions* **2016,** *45* (24), 10068-10075.
2. Ceccon, A.; Santi, S.; Orian, L.; Bisello, A., Electronic communication in heterobinuclear organometallic complexes through unsaturated hydrocarbon bridges. *Coord. Chem. Rev.* **2004,** *248*, 683-724.
3. Wheatley, N.; Kalck, P., Structure and Reactivity of Early−Late Heterobimetallic Complexes. *Chem. Rev.* **1999,** *99*, 3379-3420.
4. Stephan, D. W., Early-late heterobimetallics. *Coord. Chem. Rev.* **1989,** *95* (1), 41-107.
5. van den Beuken, E. K.; Feringa, B. L., Bimetallic catalysis by late transition metal complexes. *Tetrahedron* **1998,** *54* (43), 12985-13011.
6. Berben, L.; Peters, J., Hydrogen evolution by cobalt tetraimine catalysts adsorbed on electrode surfaces. *Chem. Commun.* **2009,** *46* (3), 398-400.
7. McCrory, C.; Uyeda, C.; Peters, J., Electrocatalytic Hydrogen Evolution in Acidic Water with Molecular Cobalt Tetraazamacrocycles. *J. Am. Chem. Soc.* **2012,** *134* (6), 3164-3170.
8. Jacques, P.-A.; Artero, V.; Pecaut, J.; Fontecave, M., Cobalt and nickel diimine-dioxime complexes as molecular electrocatalysts for hydrogen evolution with low over voltages. *Proc. Natl. Acad. Sci.* **2009,** *106* (49), 20627-20632.
9. Razavet, M.; Artero, V.; Fontecave, M., Proton Electroreduction Catalyzed by Cobaloximes: Functional Models for Hydrogenases. *Inorg. Chem.* **2005,** *44* (13), 4786-4795.
10. Fourmond, V.; Jacques, P.-A.; Fontecave, M.; Artero, V., H2 Evolution and Molecular Electrocatalysts: Determination of Overpotentials and Effect of Homoconjugation. *Inorg. Chem.* **2010,** *49* (22), 10338-10347.
11. Baffert, C.; Artero, V.; Fontecave, M., Cobaloximes as Functional Models for Hydrogenases. 2. Proton Electroreduction Catalyzed by Difluoroborylbis(dimethylglyoximato)cobalt(II) Complexes in Organic Media. *Inorganic Chemistry* **2007,** *46* (5), 1817-1824.
12. Hu, X.; Cossairt, B. M.; Brunschwig, B. S.; Lewis, N. S.; Peters, J. C., Electrocatalytic hydrogen evolution by cobalt difluoroboryl-diglyoximate complexes. *Chem. Commun.* **2005,** (37), 4723-4725.
13. Hu, X.; Brunschwig, B. S.; Peters, J. C., Electrocatalytic Hydrogen Evolution at Low Overpotentials by Cobalt Macrocyclic Glyoxime and Tetraimine Complexes. *J. Am. Chem. Soc.* **2007,** *129* (29), 8988-8998.
14. Connolly, P.; Espenson, J. H., Cobalt-catalyzed evolution of molecular hydrogen. *Inorg. Chem.* **1986,** *25* (16), 2684-2688.
15. Chao, T.-H.; Espenson, J. H., Mechanism of hydrogen evolution from hydridocobaloxime. *J. Am. Chem. Soc.* **1978,** *100* (1), 129-133.
16. Valdez, C. N.; Dempsey, J. L.; Brunschwig, B. S.; Winkler, J. R.; Gray, H. B., Catalytic hydrogen evolution from a covalently linked dicobaloxime. *Proc. Natl. Acad. Sci.* **2012,** *109* (39), 15589-15593, S15589/1-S15589/3.
17. Kelley, P.; Radlauer, M.; Yanez, A.; Day, M.; Agapie, T., Metallomacrocycles as ligands: synthesis and characterisation of aluminium-bridged bisglyoximato complexes of palladium and iron. *Dalton Trans.* **2012,** *41* (26), 8086-8.
18. Uyeda, C.; Peters, J. C., Access to formally Ni(i) states in a heterobimetallic NiZn system. *Chem. Sci.* **2013,** *4* (1), 157-163.
19. Uyeda, C.; Peters, J. C., Selective Nitrite Reduction at Heterobimetallic CoMg Complexes. *J. Am. Chem. Soc.* **2013,** *135* (32), 12023-12031.
20. Birkelbach, F.; Winter, M.; Floerke, U.; Haupt, H.-J.; Butzlaff, C.; Lengen, M.; Bill, E.; Trautwein, A.; Wieghardt, K.; Chaudhuri, P., Exchange Coupling in Homo- and Heterodinuclear Complexes CuIIM [M = Cr(III), Mn(III), Mn(II), Fe(III), Co(III), Co(II), Ni(II), Cu(II), Zn(II)]. Synthesis, Structures, and Spectroscopic Properties. *Inorg. Chem.* **1994,** *33*, 3990-4001.
21. Kitiphaisalnont, P.; Thohinung, S.; Hanmungtum, P.; Chaichit, N.; Patrarakorn, S.; Siripaisarnpipat, S., Effect of metal ions and length of alkylene bridge on the strength of hydrogen bonds in diiminedioxime cobalt(III) and nickel(II) complexes. *Polyhedron* **2006,** *25* (14), 2710-2716.

22. Pellow, M. A.; Emmott, C. J. M.; Barnhart, C. J.; Benson, S. M., Hydrogen or batteries for grid storage? A net energy analysis. *Energy & Environmental Science* **2015,** *8* (7), 1938-1952.
23. Kaljurand, I.; Kütt, A.; Sooväli, L.; Rodima, T.; Mäemets, V.; Leito, I.; Koppel, I. A., Extension of the Self-Consistent Spectrophotometric Basicity Scale in Acetonitrile to a Full Span of 28 pKa Units: Unification of Different Basicity Scales. *J. Org. Chem.* **2005,** *70* (3), 1019-1028.
24. Rose, M. J.; Gray, H. B.; Winkler, J. R., Hydrogen Generation Catalyzed by Fluorinated Diglyoxime–Iron Complexes at Low Overpotentials. *J. Am. Chem. Soc.* **2012,** *134* (20), 8310-8313.
25. Savéant, J.-M., *Elements of molecular and biomolecular electrochemistry*. John Wiley and Sons Inc.: Hoboken, New Jersey, 2006.
26. Bard, A. J.; Faulkner, L. R., *Electrochemical Methods Fundamentals and Applications*. 2nd ed.; Wiley: Hoboken, NJ, 2001.
27. Kolthoff, I. M.; Chantooni, M. K.; Bhowmik, S., Titration of bases in acetonitrile. *Anal. Chem.* **1967,** *39* (13), 1627-1633.
28. Izutsu, K., *Acid-Base Dissociation Constants in Dipolar Aprotic Solvents; IUPAC Chemical Data Series*. Blackwell Science: Oxford, UK, 1990.
29. Ahn, H. S.; Davenport, T. C.; Tilley, T. D., Molecular cobalt electrocatalyst for proton reduction at low overpotential. *Chem. Commun.* **2014,** *50* (29), 3834-3837.
30. Artero, V.; Fontecave, M., Solar fuels generation and molecular systems: is it homogeneous or heterogeneous catalysis? *Chemical Society Reviews* **2013,** *42* (6), 2338-2356.
31. Felton, G. A.; Glass, R. S.; Lichtenberger, D. L.; Evans, D. H., Iron-only hydrogenase mimics. Thermodynamic aspects of the use of electrochemistry to evaluate catalytic efficiency for hydrogen generation. *Inorganic chemistry* **2006,** *45* (23), 9181-9184.
32. Rountree, E. S.; Martin, D. J.; McCarthy, B. D.; Dempsey, J. L., Linear Free Energy Relationships in the Hydrogen Evolution Reaction: Kinetic Analysis of a Cobaloxime Catalyst. *ACS Catalysis* **2016,** *6* (5), 3326-3335.
33. Savéant, J.; Su, K., Homogeneous redox catalysis of electrochemical reaction: Part VI. Zone diagram representation of the kinetic regimes. *Journal of electroanalytical chemistry and interfacial electrochemistry* **1984,** *171* (1-2), 341-349.
34. Lee, K. J.; Elgrishi, N.; Kandemir, B.; Dempsey, J. L., Electrochemical and spectroscopic methods for evaluating molecular electrocatalysts. *Nature Reviews Chemistry* **2017,** *1* (5), 0039.
35. Kal, S.; Filatov, A. S.; Dinolfo, P. H., Electrocatalytic Proton Reduction by a Dicobalt Tetrakis-Schiff Base Macrocycle in Nonaqueous Electrolyte. *Inorg. Chem.* **2014,** *53* (14), 7137-7145.
36. Costentin, C.; Drouet, S.; Robert, M.; Savéant, J.-M., Turnover numbers, turnover frequencies, and overpotential in molecular catalysis of electrochemical reactions. Cyclic voltammetry and preparative-scale electrolysis. *Journal of the American Chemical Society* **2012,** *134* (27), 11235-11242.
37. icat equation.
38. Casely, I. J.; Ziller, J. W.; Mincher, B. J.; Evans, W. J., Bismuth Coordination Chemistry with Allyl, Alkoxide, Aryloxide, and Tetraphenylborate Ligands and the $\{[2,6\text{-}(Me_2NCH_2)_2C_6H_3]_2Bi\}^+$ Cation. *Inorg. Chem.* **2010,** *50* (4), 1513-1520.
39. Favier, I.; Duñach, E., New protic salts of aprotic polar solvents. *Tetrahedron Lett.* **2004,** *45* (17), 3393-3395.
40. Norris, M. R.; Concepcion, J. J.; Glasson, C. R. K.; Fang, Z.; Lapides, A. M.; Ashford, D. L.; Templeton, J. L.; Meyer, T. J., Synthesis of Phosphonic Acid Derivatized Bipyridine Ligands and Their Ruthenium Complexes. *Inorg. Chem.* **2013,** *52* (21), 12492-12501.
41. Kaljurand, I.; Kütt, A.; Sooväli, L.; Rodima, T.; Mäemets, V.; Leito, I.; Koppel, I. A., Extension of the Self-Consistent Spectrophotometric Basicity Scale in Acetonitrile to a Full Span of 28 pKa Units: Unification of Different Basicity Scales. *The Journal of Organic Chemistry* **2005,** *70* (3), 1019-1028.
42. Drago, R. S., *Physical Methods for Chemists*. 2nd ed.; Surfside Scientific Publishers: Gainesville, Fl, 1992.

CHAPTER 3. MEASURING EQUILIBRIUM BINDING RATES AND ELECTRONIC CHANGES BETWEEN SMALL MOLECULES AND CDSE QUANTUM DOTS

Contributions to this chapter were made by Dr. Dan Kroupa

3.1 Introduction

Among industrially relevant chemical reactions, redox reactions are important in the production of a variety of valuable chemicals.[1-2] For example, a potential widespread solar fuel, H_2, can be synthesized by the electrolysis of water. The movement of electrons in these systems is controlled through electrical potential by use of a potentiostat. While this electrical potential could be generated using an indirect renewable energy source, such as a photovoltaic, the direct generation of high potential electrons in a photocatalytic system would be valuable.

In a techno-economic analysis, the US Department of Energy has projected that photoelectrochemical systems composed of colloidal, solution-phase components are the most economically viable means of generating H_2, though there are significant materials chemistry challenges to be overcome.[3] Chief among these concerns is photosensitizer redox potentials, stability and ability to reduce back electron transfer. Two classes of solution-phase photosensitizers can be considered - molecular and semiconducting photosensitizers. Semiconducting, quantum-confined photosensitizers have many advantages such as long-lived excited states, tunable surface chemistry, increased stability and lower cost compared to precious metal, molecular photosensitizers such as $Ru(bpy)_3$.[4]

In the case of colloidal quantum dots, back electron transfer has the potential to be modulated through the surface chemistry of these semiconducting photosensitizers. Currently photo-induced back electron transfer is modulated in system specific ways, such as the charge separated state's dipole orientation.[5-6] An alternative approach that would be generalizable would be to provide a driving force for forward electron transfer with selective binding of catalysts such that, upon reduction of the catalyst, it is

expelled from the coordination-sphere of the photosensitizer, thus limiting back electron transfer. Upon return to the molecular catalyst resting state, the affinity of the catalyst molecule for the photosensitizer interface would be restored, enabling efficient photocatalysis.

Currently, the equilibrium binding of various molecules to the surface of semiconducting photosensitizers have been measured through changes in photoluminescence (PL),[7-12] through isothermal titration calorimetry,[13] and by NMR spectroscopy.[14-16] Each of these techniques has an associated time-scale for measuring equilibrium processes and as such has associated limitations. For example, in the case of PL quenching, the primary assumption is that changes in photoluminescence intensity is directly proportional to electron transfer to the acceptor molecule, although this is not necessarily true and the data can be complicated with the redox potentials of the adsorbate molecules as well as other competing events such as trap state recombination. Often PL quenching does not correlate with an actual binding event and therefore is not reliable.[17] NMR spectroscopy does allow the ability to rigorously calculate binding constants, although this method is restricted to systems with appropriate chemical shifts for the technique and does not afford electronic information about the adsorbate upon binding.

In this chapter we explore the equilibrium binding between adsorbates and the semiconducting photosensitizer, CdSe quantum dots, using cyclic voltammetry. Cyclic voltammetry can measure electronic structure changes of an adsorbate as the result of interaction with CdSe by measuring the potential at which the oxidation and reduction of the new species occurs. This technique can also measure binding constants by monitoring the decrease in current as a result of the new species' lower diffusion coefficients. In these ways we can track equilibrium binding of an adsorbate to CdSe through the shift in potential and changes in current of the resulting voltammogram. The ability to tune the scan rate in these experiments also allows for evaluating equilibria that span a range of kinetic rates. This technique can provide robust, quantitative information about the interaction of quantum dot photosensitizers with electroactive small molecule adsorbates and is likely to prove a generalizable strategy to learn about both quantum dot surface chemistry and the modulation of electronic structure that results from donor-acceptor interactions in these systems.

3.2 Results and discussion

3.2.1 Investigating the equilibrium binding of CdSe and ferrocene derivatives by cyclic voltammetry

An example equilibrium process can be seen in Scheme 3.1, where species A is in equilibrium with species B. The forward rate constant is described by k_f, k_b describes the backward rate constant and K, the equilibrium constant, is the ratio of k_f. to k_b. In order for cyclic voltammetry to be sensitive to any non-electrochemical equilibrium events that perturb the electrochemistry, such as chemical reactions and binding interactions, the associated values for k_f and k_b, must be large enough on the time-scale of the CV experiment. This is described by the dimensionless kinetic parameter for cyclic voltammetry, λ, seen in Equation 3.1. For example, at a scan rate of 1,000 mV/s and under standard conditions, the lower limit of the combined value of k_f and k_b is ~4 s^{-1} regardless of the value of K.[18]

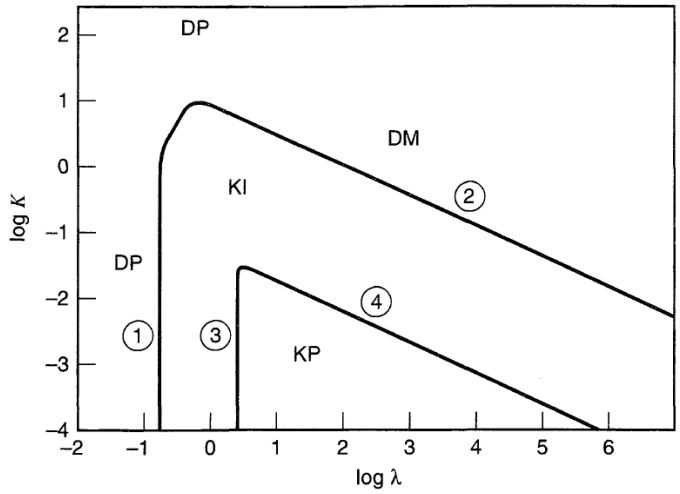

Figure 3.1. C_rE_r reaction diagram demonstrating different electrochemical zones as a function of K and λ; DP= pure diffusion, KI= intermediate kinetics, KP= pure kinetics and DM= diffusion modified by equilibrium constant of preceeding reaction. Source: Bard, A. J.; Faulkner, L. R.; Leddy, J.; Zoski, C. G., *Electrochemical methods: fundamentals and applications*. Wiley New York: 1980; Vol. 2.

We can utilize a zone diagram in order to predict what behavior will be observed electrochemically (Figure 3.1). In the pure diffusion zone (DP), the electrochemical response will not be a result of equilibrium, but instead represent either species A or B. On the left side of the graph under DP, only A will be observed as the process is not fast enough and on the right side of the graph, under DP, only B will be observed as the process is now too fast. We can transition between zones if the value for K is not too high (above 10) and if the k_f/k_b is not too low compared to the scan rate. In these regimes, the easiest way to move zones is to increase the scan rate (decrease λ) or decrease the scan rate (increase λ). We can utilize this zone diagram in order to enter a zone where we are able to observe an equilibrium process. This is also useful if there is no information about the electrochemistry of B. By transitioning zones, we can access this information. For example, we might increase the scan rate in order to access the electrochemical response of only B and not an equilibrium response. Zones DM (diffusion modified), KI (intermediate kinetics, and KP (pure kinetics) all give equilibrium electrochemical responses. KP describes a zone in which the electrochemical response is not diffusion controlled and will exhibit an S-shape voltammogram. KI and DM both describe intermediate zones.

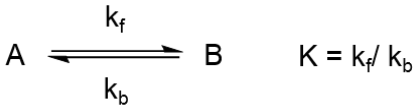

Scheme 3.1. Example equilibrium process.

$$\lambda = \frac{k_f + k_b}{\nu}\left(\frac{RT}{nF}\right) \qquad \text{Equation 3.1}$$

We sought to explore the equilibrium interactions between CdSe and adsorbate molecules by cyclic voltammetry. Reports in the literature support that this could be possible with equilibrium constants on the order of 10^{-1}-10^{2}.[7, 16] We sought molecules that might have lower equilibrium binding constants in order to more easily observe their equilibrium by electrochemistry. We chose ferrocene (Fc) due to its inability to directly coordinate the CdSe surface through inner-sphere chemistry, and other ferrocene derivatives, ferrocene carboxylic acid and decamethylferrocene for comparison (Figure 3.2), due to their

well-behaved, reversible electrochemistry in a potential range where reduction or oxidation of the CdSe would not occur.

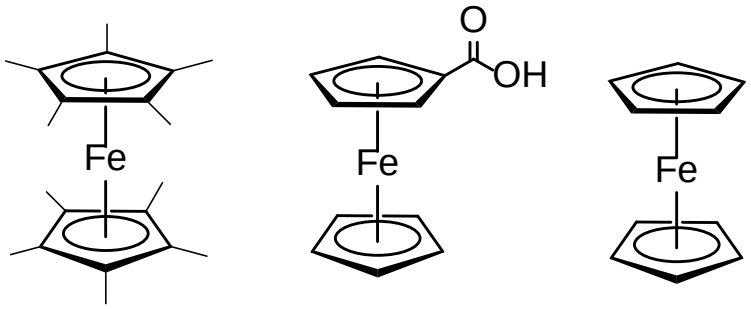

Figure 3.2. Ferrocene and ferrocene derivatives used in this study.

Solvent choice was crucial to maintain solubility of the CdSe, which is typically soluble in nonpolar solvents as-synthesized, as well as of the electrolyte at a concentration of at least 0.1 M necessary for the electrochemical measurements. Finally, another consideration of solvent choice is the ability to facilitate fast heterogeneous electron transfer between the redox-active molecule and the electrode. To illustrate this point, the effect of CH_3CN on electron transfer kinetics is shown in Figure 3.3. This data shows a decrease in ΔE_p of the ferrocene couple from 380 mV in the pure THF solvent down to 72 mV after over 23% CH_3CN has been added. This is likely due to the increased dielectric of CH_3CN allowing for faster electron transfer. Tetrahydrofuran (THF) meets the qualifications of the first two criteria, however in order to maintain good electron transfer kinetics and maintain CdSe solubility, a 90/10 THF/CH_3CN mixture was used in following study.

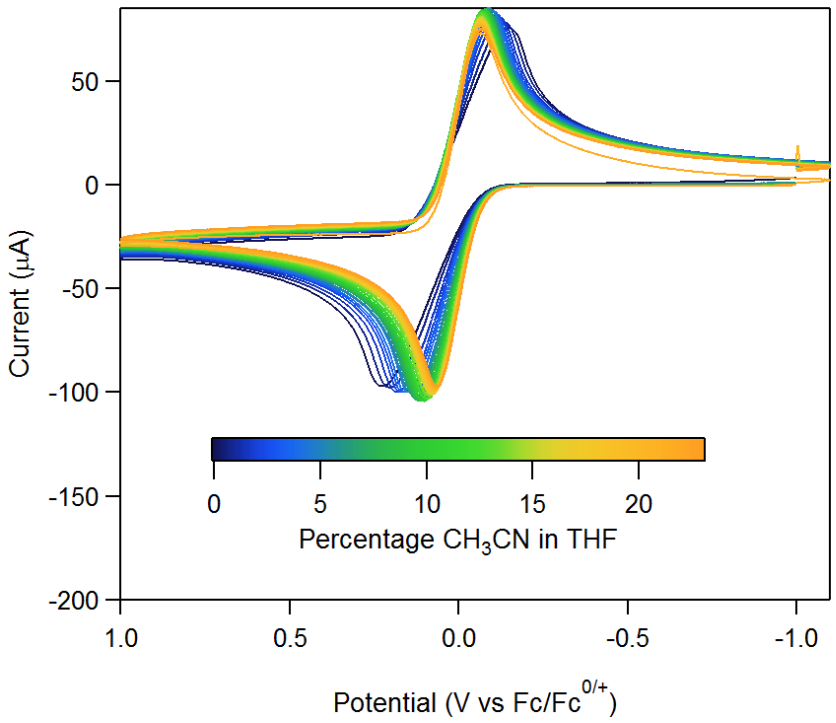

Figure 3.3. CVs of 0.5 mM ferrocene upon addition of CH_3CN to THF, 0.2M $^nBu_4PF_6$, glassy carbon working, Pt aux and Ag wire ref, 100 mV/s.

Beginning with a solution of 2 mM ferrocene in a 90/10 solution of THF/CH_3CN, we performed a titration of CdSe into the Fc solution (Figure 3.4). Upon addition of CdSe, we observe significant changes in the voltammogram, which are more prominent at higher scan rates, such as 7,000 mV/s (Figure 3.5). Specifically, an anodic shift in the half peak potential, $E_{p/2}$, of the Fc peak is observed. This shift is a thermodynamic effect, the magnitude of which reflects the energy by which Fc is stabilized by interaction with CdSe.

This first piece of evidence indicates a reversible chemical step preceding an electrochemical step, a C_rE_r mechanism, in the case where K is large. Intuitively, as the scan rate is increased, the equilibrium time is shorter and therefore a higher concentration of the new species is measured near the electrode

surface. Relating this to the zone diagram above, as λ is decreased, we are qualitatively transitioning from the upper right of the graph from zone DM toward zone KI.

Differences in the voltammograms can also be observed in the cathodic wave. A decrease in amplitude of the original cathodic wave, greater than that seen in the anodic wave, and the appearance of a new peak is observed. This suggests that not only does Fc interact with the CdSe, but Fc^+ does as well and qualitatively in a stronger interaction. With the assumption that both Fc and Fc^+ are interacting with the CdSe and that the associated complexes, Fc-CdSe and Fc^+-CdSe, are electrochemically active, a square scheme can be constructed (Scheme 3.2). Associated with this sqaure scheme is Equation 3.2, which describes the relationship between Fc, Fc^+, Fc-CdSe and Fc^+-CdSe.

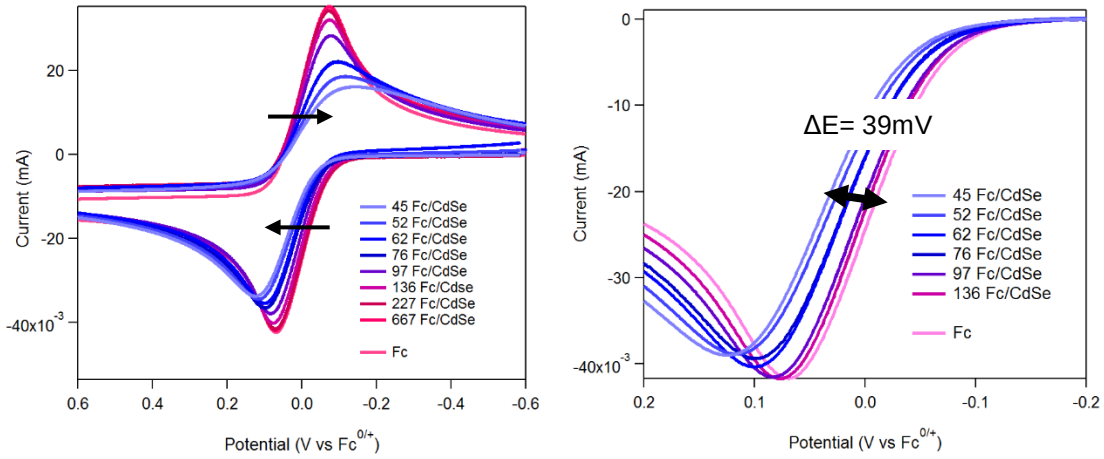

Figure 3.4. a) CVs of 2mM ferrocene and upon additions of CdSe solution, 0.15 M $^nBu_4PF_6$, 90/10 THF CH_3CN, glassy carbon working, Pt aux and Ag wire ref, 100 mV/s b) anodic wave from (a) that has been volume corrected from the titration showing the $\Delta E_{p/2}$.

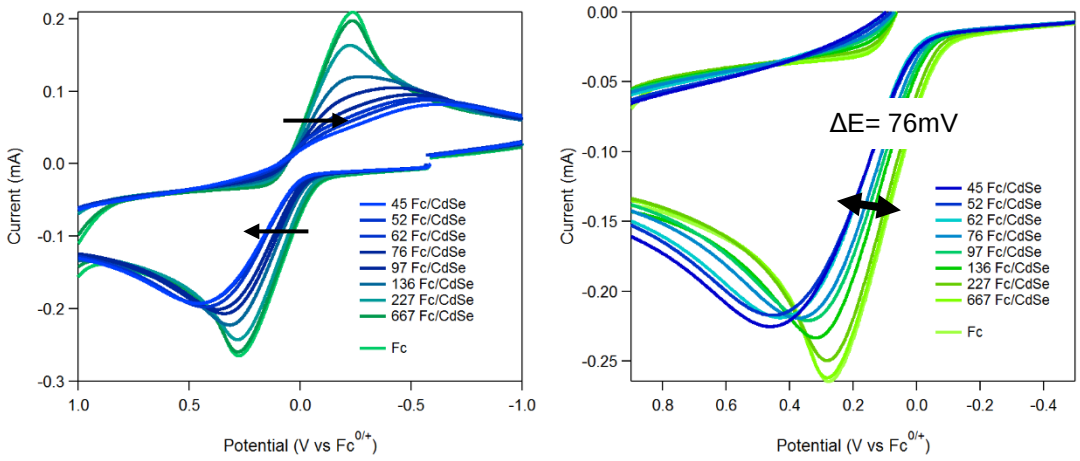

Figure 3.5. CVs of 2 mM ferrocene and upon additions of CdSe solution, 0.15 M $^{n}Bu_4PF_6$, 90/10 THF CH_3CN, glassy carbon working, Pt aux and Ag wire ref, 7,000 mV/s, b) anodic wave from (a) that has been volume corrected from the titration showing the $\Delta E_{p/2}$.

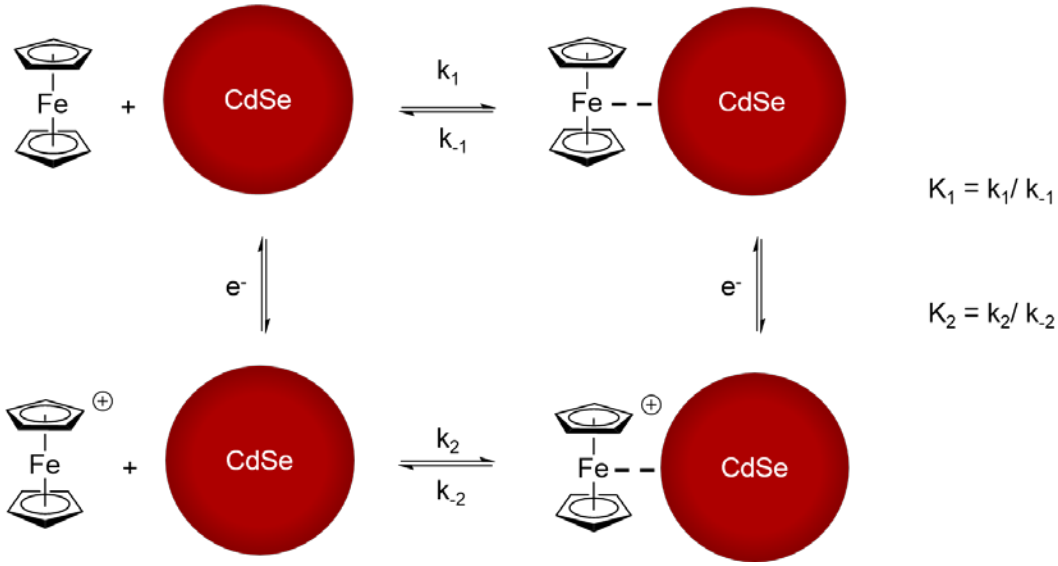

Scheme 3.2. Square scheme depicting the interaction between Fc and Fc^+ with CdSe.

The $\Delta E_{p/2}$ in the anodic peaks increase from 39 mV to 76 mV as the scan rate is increased from 100 mV/s to 7,000 mV/s (Figure 3.4 and 3.5). At higher scan rates and higher CdSe/Fc ratios, the potential

of the half wave of the anodic peak stops decreasing (Figure 3.6). We believe that this peak is indicative of the oxidation potential of the CdSe-Fc species.

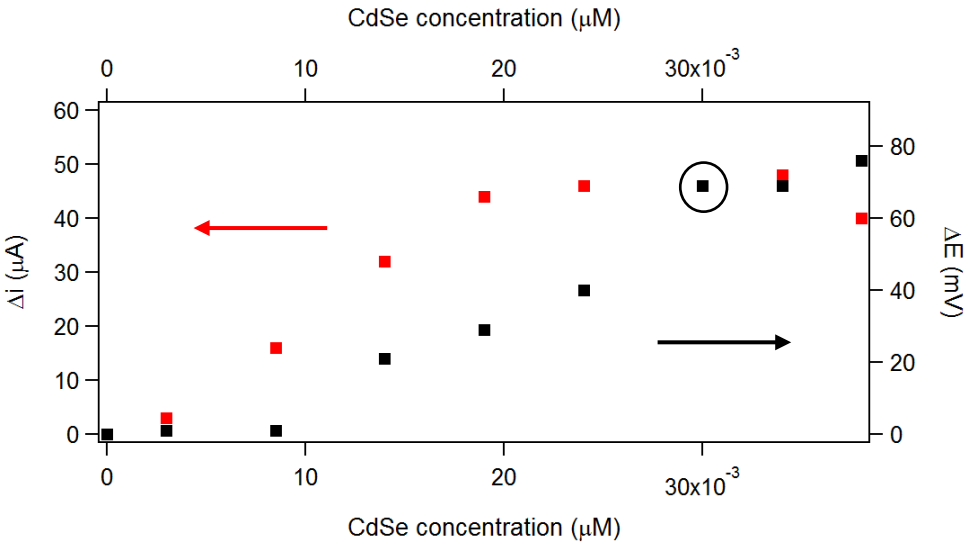

Figure 3.6. Comparing changes in $E_{p/2}$ and i_p as a function CdSe concentration; the circled point corresponds to a ratio of 62 Fc/CdSe; red and black dots are overlapping here.

In addition to potential shifts, the current magnitude also decreases, even after correction for volume increases from the titration. This can be attributed to the decreased diffusion coefficient of the Fc-CdSe and Fc^+-CdSe. This is expected since the diffusion coefficients (measured by DOSY NMR for CdSe and from the Randles-Sevich equation for Fc) are different by an order of magnitude, decreasing from 3.03 x 10^{-6} to 1.7 x 10^{-7} cm^2/s. In order to find the ratio of freely diffusing Fc to that of the Fc-CdSe, increasing equivalents of CdSe were added and the scan rate was increased to 7,000 mV/s. The i_{pc} reached a plateau at the ratio 52 Fc/CdSe under these conditions. Since we view this trace as the Fc-CdSe species, we can obtain the ratio, $D_{CdSe\text{-}Fc}/D_{Fc}$, from the ratio of the peak currents, $i_{pCdSe\text{-}Fc}/i_{p,Fc}$ This was found to be 1.16 and is important in the following electrochemical simulations.

The CVs presented in Figure 3.3 and 3.4 suggest that the oxidation of Fc-CdSe and the reduction of Fc^+-CdSe) both more oxidative and more reductive respectively than the original (Fc/Fc^+). This situation is unreasonable, and it is more likely that the new redox couple of Fc-CdSe/Fc^+-CdSe is similar in E^0, but

has a lower heterogeneous electron transfer rate, k^0, which governs the peak-to-peak separation and leads to the CVs seen above.

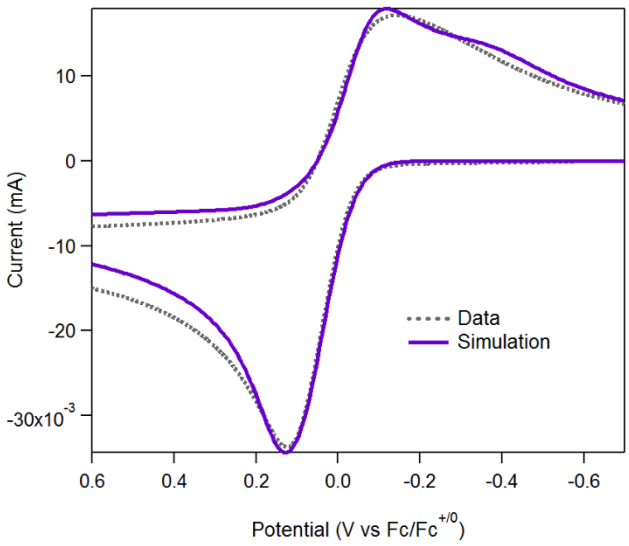

Figure 3.6. Electrochemical data (62 Fc/CdSe @ 100 mV/s) overlayed with simulation using the square scheme equilibriation model.

Electrochemical modeling software, DigiSim, was utilized to model the following equilibrium processes. The parameters used to model the system can be seen in Table 3.1. Notably we used the $D_{CdSe\text{-}Fc}/D_{CdSe\text{-}Fc}$ ratio and accounted for an average of 62 Fc molecules interacting with 1 CdSe nanocrystal from the data in Figure 3.6. The transfer coefficient, α, was modulated in order to fit the relative peak breadth. In order to achieve a satisfactory fit, the heterogeneous rate constant was decreased from 0.0015 to 0.0001 cm/s and to account for the new peak, the $E^{0'}$ of the Fc^+-CdSe/ Fc-CdSe was modeled to be 20 mV more negative than the Fc/Fc^+ couple. When analyzing the square scheme, a change in the $E^{0'}$(Fc-CdSe/Fc^+-CdSe) of 59 mV will result in a change of 10x in the equilibrium ratio K_2/K_1 as demonstrated from Equation 3.2. Therefore, the small shift in potential observed in this system represents an increase in the equilibrium constant for Fc^+-CdSe by ~2x. Although this is unexpected when considering interactions with CdSe originate primarily through the Cd^{2+} binding sites on the surface,[19-20] recent research suggests that Se^{2-} sites can be accessed on the surface of CdSe,[21-23] and we propose these sites are responsible for the greater interaction between CdSe and Fc^+.

In order to demonstrate the effect of two important parameters, k^0 and the shift in $E^{0'}$(Fc-CdSe/Fc^+-CdSe), simulations were carried out, allowing these values to remain the same for Fc/Fc^+ and unperturbed for this new couple (Figure 3.7). Without accounting for the shift in $E^{0'}$(Fc-CdSe/Fc^+-CdSe), the top peak shape is not accurately described. Similarly, if the k^0 is not modulated the peak shifts in the anodic and cathodic waves are not taken into account.

Table 3.1 Parameters used to fit the electrochemical simulation in 3.6

Parameter	Value used in simulation
K_1	500
K_2	1089
$E^{0'}$(Fc-CdSe/Fc^+-CdSe)	-20 mV
$E^{0'}$(Fc- /Fc^+-)	0 mV
$\alpha_{(Fc- /Fc+-)}$	0.5
$\alpha_{(Fc-CdSe/Fc+-CdSe)}$	0.3

$$E^{0'}\left(\frac{Fc-CdSe}{Fc^+-CdSe}\right) = E^{0'}\left(\frac{Fc}{Fc^+}\right) - \frac{RT}{nF}\ln\left(\frac{K_2}{K_1}\right) \qquad \text{Equation 3.2}$$

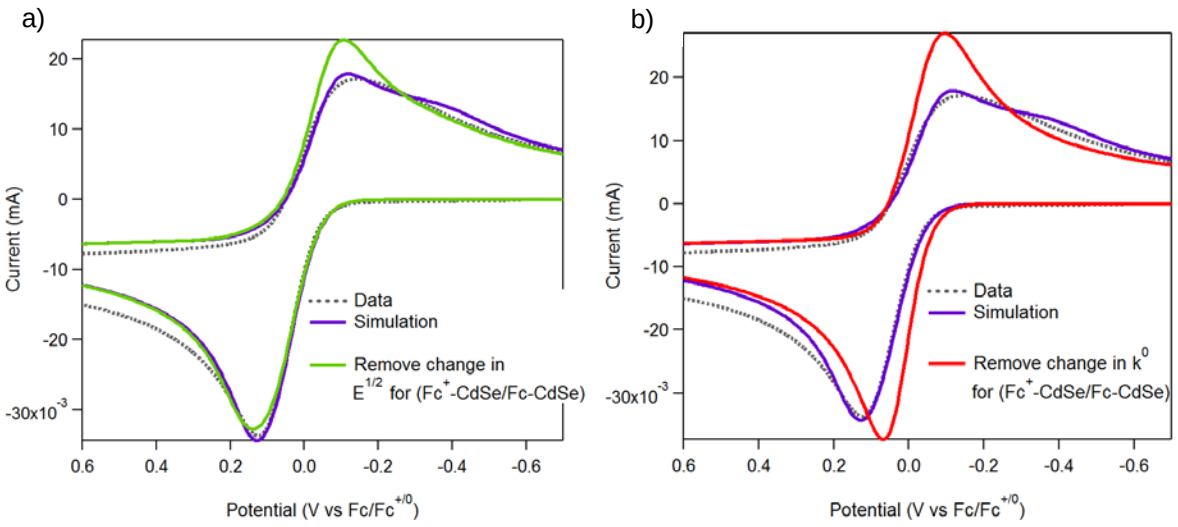

Figure 3.7. Simulations overlayed with changes in simulation a) the change in $E^{1/2}$ for Fc^{+}-CdSe and b) change in k^0 for Fc^{+}-CdSe/CdSe-Fc.

The experiments above were repeated with two other ferrocene derivatives: ferrocene carboxylic acid (FcCA) and decamethylferrocene (dmFc) (Figure 3.8). Interestingly the dmFc displays no evidence for equilibrium binding. We hypothesize that the presence of the methyl groups may prevent close association of dmFc with the CdSe surface, pushing the equilibrium out of the range that is detectable by cyclic voltammetry. Alternatively, the sum of k_f and k_b, or the frequency of the interaction may be too low to observe. On the other hand, FcCA has a greater binding affinity for CdSe as can be seen in the larger potential shift and greater change in current upon addition of CdSe. This is likely a result of the ferrocene carboxylic acid's ability to exchange with the oleate ligands on the CdSe surface. This demonstrates that the equilibrium binding of small molecules to CdSe can be modulated by size and functional group and that these changes in equilibrium are detectable using the cyclic voltammetry method.

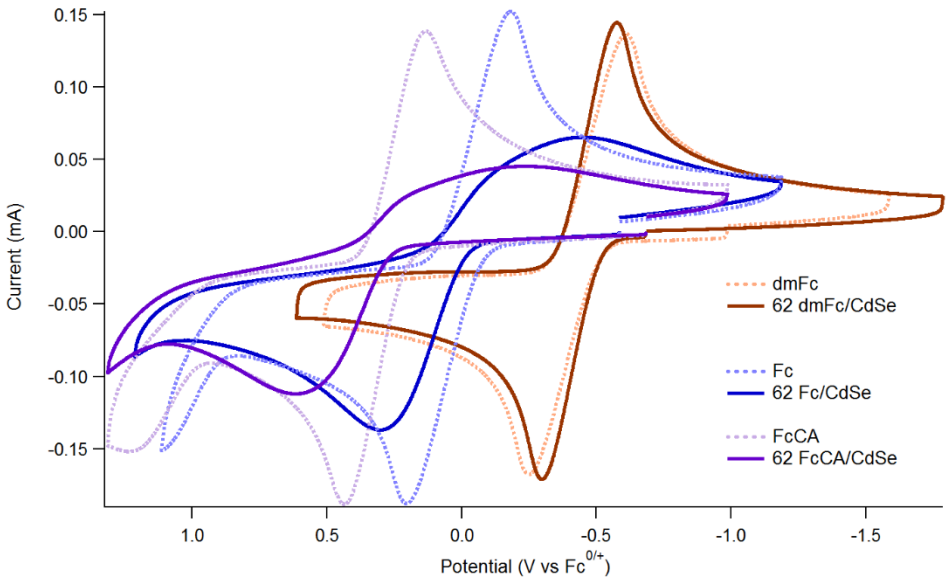

Figure 3.8. a) CVs of 2mM Fc, DmFc and FcCA and upon additions of CdSe solution, 0.15M $^{n}Bu_4PF_6$, 90/10 THF CH_3CN, glassy carbon working, Pt aux and Ag wire ref, 3000mV/s

3.2.2. Spectroscopic measurements of CdSe small molecule interactions

In order to further support our hypothesis of equilibrium binding, steady-state photoluminescence (PL) and transient absorption (TA) spectroscopies were also carried out. The PL spectra of CdSe QDs without the addition of Fc^+ (Figure 3.9A) shows band edge excitonic emission (E), as well as lower energy peaks (D_1, D_2, D_3) indicating the presence of optically active mid-gap defect states. For metal chalcogenide QDs, these defect states are often associated with undercoordinated surface atoms.[24] Upon addition of Fc^+, we observed a simultaneous decrease in the defect related PL peaks with an increase in the excitonic PL peak, consistent with Fc^+ adsorbing to the QD surface and passivating defect states (Figure 3.9B). At the highest Fc^+ loading, a quenching of the QD band edge excitonic emission in observed.

TA spectroscopy was used to study the electronic excited state dynamics of the CdSe QD / Fc^+ interaction. We did not observe any transient spectral features associated with Fc/Fc^+ (Figure 3.10A), concluding that Fc/Fc^+ must electronically interact with the CdSe QDs in the ground state. Analysis of the TA kinetics of CdSe QDs without the addition of Fc^+ (Figure 3.10B, black) shows a nanosecond recovery of the excitonic bleach consistent with band-to-band recombination in CdSe QDs. The addition

of Fc^+ results in the growth of a fast (picosecond) recovery component of the excitonic bleach. In combination with the exciton quenching observed at high Fc^+ loading in steady-state PL, we propose that the fast decay component is a result of hole trap-assisted Auger recombination, which arises from ground state electron transfer from QD surface Se to form Fc and a localized hole at the QD surface.[25] Upon photoexcitation of such a complex, the band edge electron rapidly recombines with the surface localized hole by nonradiatively transferring its energy to the band edge hole. Notably, the $dmFc^+$ has no effect on the TA kinetics of the CdSe recombination, corroborating our hypothesis that dmFc/ $dmFc^+$ does not interact appreciably with the QD surface (Figure 3.10C and D).

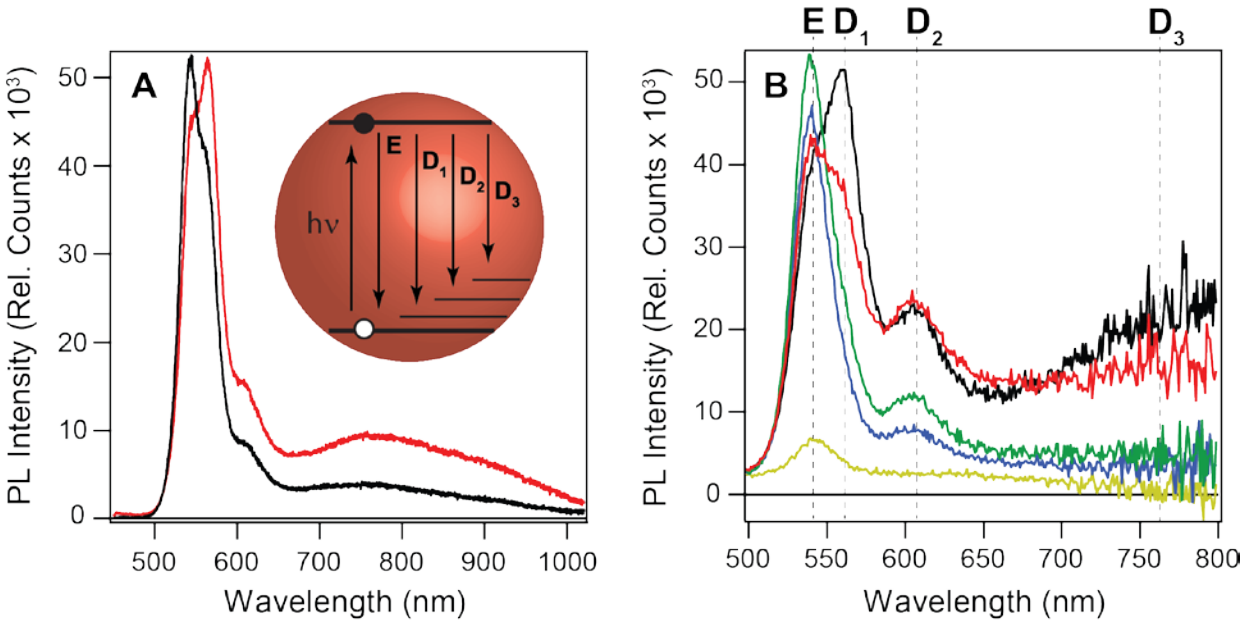

Figure 3.9. (A) Photoluminescence spectra of the CdSe nanocrystals before (black) and after (red) purification through a gel permeation chromatography column. (B) Photoluminescence spectra of the CdSe nanocrystals before addition of Fc^+ (black) and after addition of 7 eq (red), 83 eq (green), 167 eq (blue) and 333 eq (yellow) of Fc^+. The emission peaks associated with band-to-band recombination (exciton; E) and defects (D_1, D_2, D_3) are illustrated in the inset of panel A.

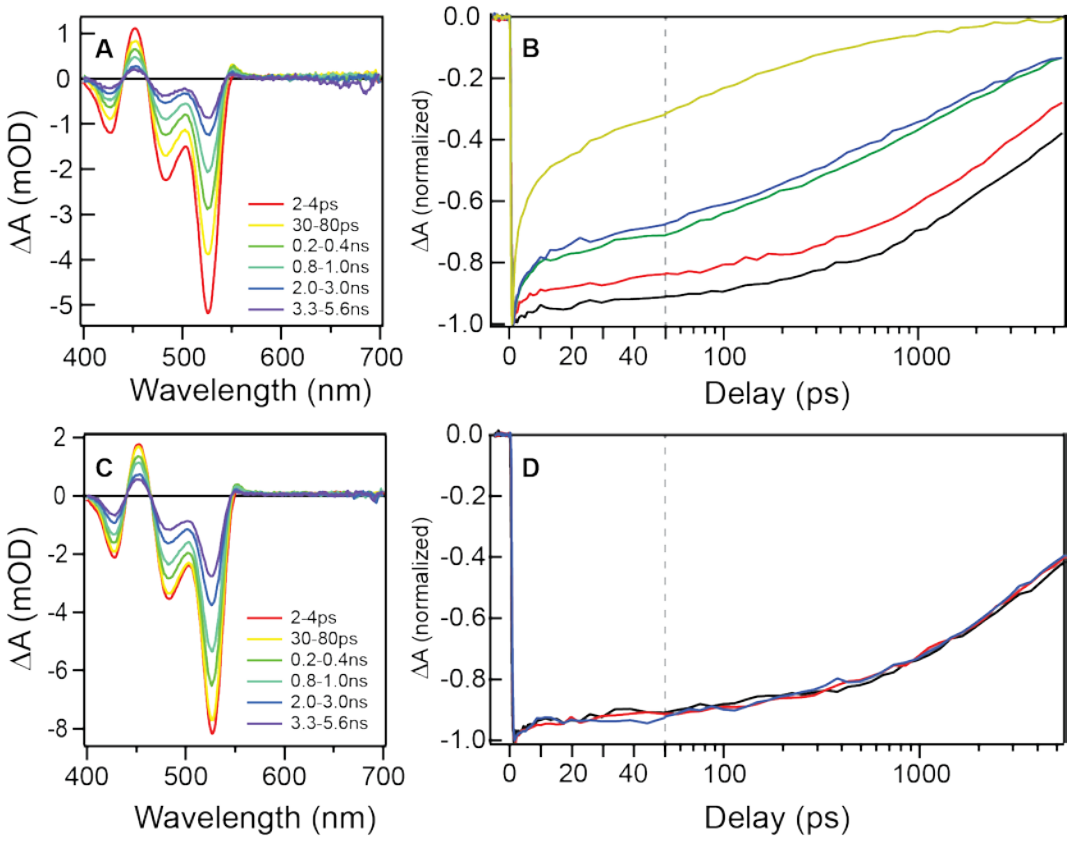

Figure 3.10. (A) Representative transient spectral data for CdSe nanocrystals with added Fc^+. (B) Transient kinetic data for CdSe QDs before addition of Fc^+ (black) and after addition of 7 eq (red), 83 eq (green), 167 eq (blue) and 333 eq (yellow) of Fc^+. (C) Representative transient spectral data for CdSe nanocrystals with added $dmFc^+$. (D) Transient kinetic data for CdSe QDs before addition of $dmFc^+$ (black) and after addition of 23 eq (red) and 275 eq (blue).

3.2.3. Preliminary evidence for small molecule selective oxidation state binding with CdSe

As mentioned in the introduction of this chapter, the selective binding of electroactive small molecules only in specific oxidation states has the potential to serve as a mechanism to decrease back electron transfer and increase efficiencies of photocatalytic reactions. Recalling the cobaloxime complexes developed in Chapter 2, we examined the interaction of complex **1** (doubly deprotonated Co) and complex **2** (bimetallic Co-Zn) with CdSe (Figure 3.11). Here we observe only one of the Co(III/II) or Co(II/I) waves decreasing in current upon addition of CdSe, suggesting only one particular redox couple

is interacting the CdSe and decreasing its diffusion coefficient. Interestingly for complex **1**, the Co(II/I) is most effected. This may result from the increased electron density on the deprotonated dioxime oxygen atoms promoting Cd^{2+} binding at the CdSe surface. Conversely, for complex **2**, Zn^{2+} for Cd^{2+} exchange may be promoted when Co is in a higher oxidation state where the oxime oxygens are less basic, leading to only observation of equilibrium binding with the Co(III/II) couple by cyclic voltammetry.

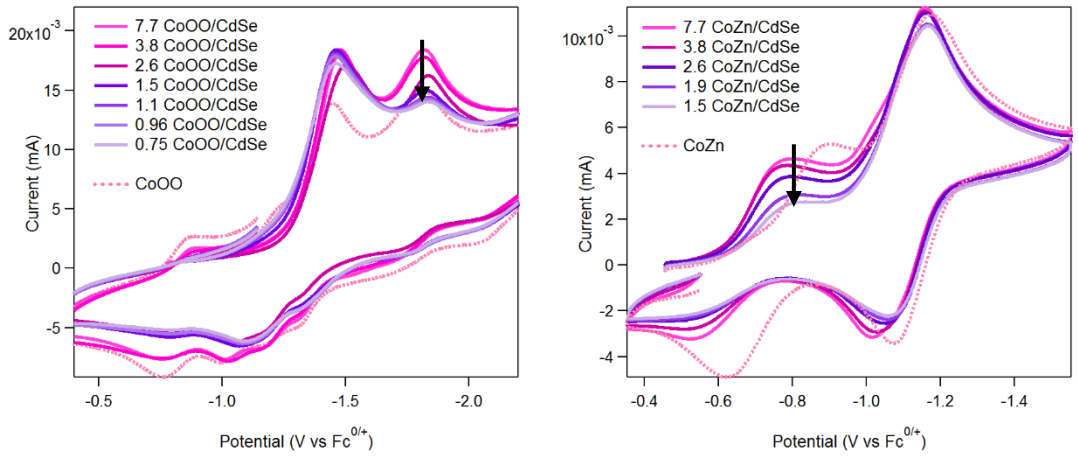

Figure 3.11. CVs of 2 mM a) complex **1** and b) complex **2** upon addition of CdSe, 0.15 M $^{n}Bu_4PF_6$, 90/10 THF CH_3CN, glassy carbon working, Pt aux and Ag wire ref, 300 mV/s.

In order to more completely probe the nature of the interaction between the quantum dot and the redox-active probe molecule, the effect of the quantum dot surface charge should be investigated. The stoichiometry of CdSe surfaces can be tuned from Cd^{2+}-rich to Se^{2-}-rich, which should have a measurable impact on the equilibrium binding of oxidized or reduced species. Measuring the zeta potential of CdSe surfaces would be a first step. Then exploration of a redox-active probe that can be oxidized or reduced to yield charged species would be illuminating. For example, $V^{III}(acac)_3$ undergoes a reduction to the negatively charged species, $[V^{II}(acac)_3]^-$ and an oxidation to the positively charged species, $[V^{IV}(acac)_3]^+$. This redox probe is ideal as both redox couples are reversible and within the electrochemical window of THF.[26] Even qualitatively, the degree of the potential shift and current decreases between the V(II/III) and V(III/IV) couples upon addition of CdSe would allow the determination of the dominant effect. If the couple containing the negatively charged species, V(II/III), is perturbed then likely surface Cd^{2+} is dominant,

whereas if the couple containing the positively charged species, V(III/IV), is perturbed, then the surface Se^{2-} is dominant. This would allow the direct investigation of these effects within a single experiment.

A general strategy for a reductive catalyst interacting primarily through Cd^{2+} can be seen in Figure 3.12. In this scheme, the small molecule catalyst is in equilibrium with Cd^{2+} and M^{2+} in solution. Upon reduction of the small molecule to a reduced state, the equilibrium binding constant of the small molecule with M^{2+} in solution is greater relative to its binding constant with Cd^{2+}. The reduced form of this catalyst is less attracted to the surface of CdSe, limiting the back electron transfer upon reduction and thus improving efficiencies of reductively driven photocatalytic processes.

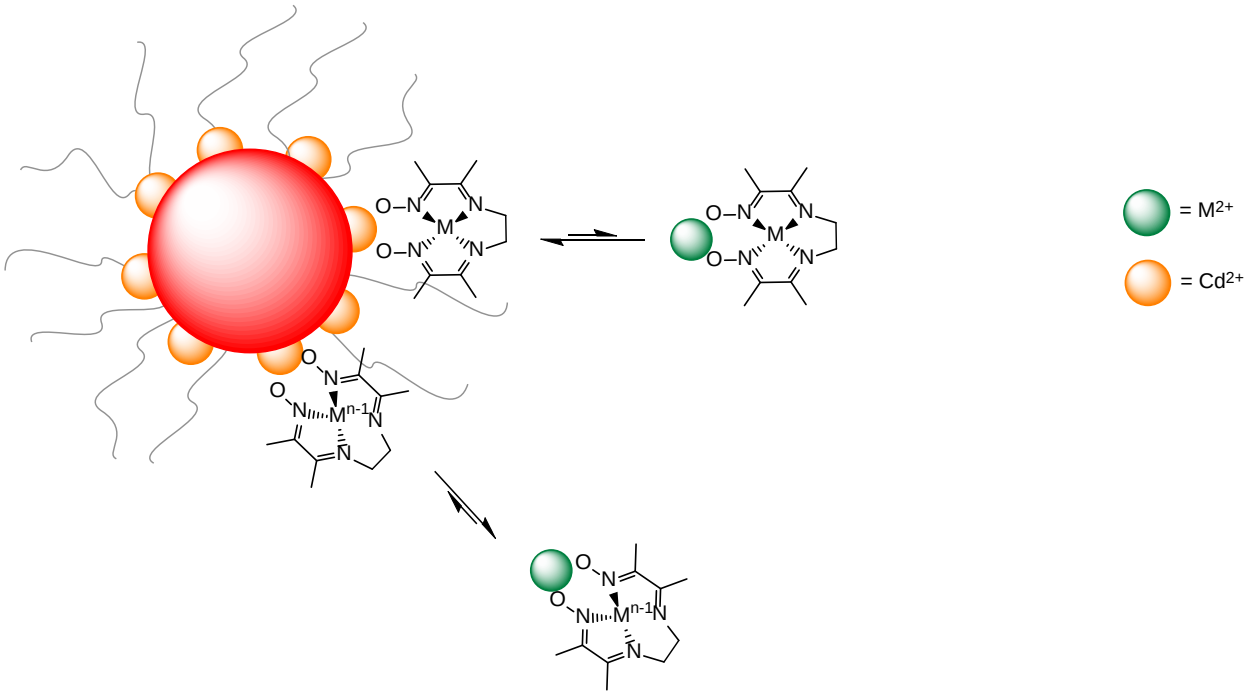

Scheme 3.3. Proposed interactions of a small molecule with Cd^{2+} at the surface of CdSe and with M^{2+} in solution. The equilibrium is perturbed upon reduction to favor binding with M^{2+} in solution, effectively expelling the small molecule from the surface of CdSe upon reduction.

3.3 Conclusions

In conclusion, cyclic voltammetry has been demonstrated as a sensitive and powerful probe of equilibrium binding of electroactive small molecules to the surface of colloidal quantum dot photo-senistizers. In combination with other techniques such as transient absorption and PL quenching, this method provides detailed information about the evolution of CdSe electronic structure on interaction with donor or acceptor species. In the case of Fc/Fc^+, a square scheme can be constructed which enables us to deduce that Fc^+ is more attracted to the surface of CdSe, with a measured 2x increase in equilibrium constant when compared with the neutral Fc. Substituents can be used to perturb the equilibrium binding of these electroactive species, as was demonstrated in the case of ferrocene carboxylic acid and decamethyl ferrocene. Preliminary evidence also shows that selective oxidation state binding may be a viable mechanism to engineer cascade catalysis in photoelectrochemical systems, suppressing back electron transfer processes and improving overall light-to-fuel efficiency.

3.4 Experimental

All electrochemical experiments were performed in a N_2 filled glove box. The electrolyte $[^nBu_4N][PF_6]$ used in cyclic voltammetry experiments was recrystallized two times in EtOH and dried overnight under vacuum at 100 °C. All CV experiments were taken in a N_2 filled glove box. Ferrocene was recrystallized in pentane and ferrocene carboxylic acid and decamethylferrocene were recrystallized in CH_3CN and toluene. Glassy carbon working electrodes (CH Instruments and BASi), platinum auxiliary electrode (BASi) and a Ag wire pseudo reference electrode in a Vycor-fritted compartment (BASi) filled with $[^nBu_4N][PF_6]$ and CH_3CN were used. Glassy carbon electrodes with a diameter of 3.0 mm were polished using 0.05, 0.3 and 1.0 micron polishing powder (CHI instruments) followed by 5-minute sonication cycles in deionized water for every set of electrochemical experiments. All experiments were referenced to an internal ferrocene standard added after the experiment unless otherwise noted. Ultra-high purity acetonitrile used in cyclic voltammetry (Burdick and Johnson) was dried over alumina overnight, subjected to 3 freeze pump thaw cycles, brought in the glove box, filtered and stored over 3 Å molecular sieves. Tetrahydrofuran was purified on a solvent system and stored over 3 Å molecular sieves.

CdSe nanocrystals were synthesized according to literature procedures[17] using CdO, Se powder and oleic acid in a heat-up synthesis. The material was worked up in a N_2 filled glovebox. One crash out using toluene as the solvent and MeOH as the antisolvent was performed and the resulting material was dissolved in toluene and run once down a gel permeation column. ^{1}H NMR shows that there are no free ligands exchanging with the surface. The synthetic batch was portioned out and the toluene removed in vacuo. The CdSe used for electrochemical measurements was immediately dissolved in the 90/10 CH_3CN/THF electrolyte mixture and discarded after 1 day.

3.5 References

1. Baizer, M., Prospects for further industrial applications of organic electrosynthesis. *Journal of Applied Electrochemistry* **1980,** *10* (3), 285-290.
2. Wagenknecht, J. H., Industrial organic electrosynthesis. ACS Publications: 1983.
3. James, B. D.; Baum, G. N.; Perez, J.; Baum, K. N., Technoeconomic analysis of photoelectrochemical (PEC) hydrogen production. *DOE report* **2009**.
4. Wilker, M. B.; Schnitzenbaumer, K. J.; Dukovic, G., Recent Progress in Photocatalysis Mediated by Colloidal II-VI Nanocrystals. *Israel journal of chemistry* **2012,** *52* (11-12), 1002-1015.
5. Tao, N., Electron transport in molecular junctions. *Nature nanotechnology* **2006,** *1* (3), 173.
6. Han, Y.; Dillon, R. J.; Flynn, C. J.; Rountree, E. S.; Alibabaei, L.; Cahoon, J. F.; Papanikolas, J. M.; Dempsey, J. L., Interfacial electron transfer yields in dye-sensitized NiO photocathodes correlated to excited-state dipole orientation of ruthenium chromophores. *Canadian Journal of Chemistry* **2017,** (000), 1-10.
7. Donakowski, M. D.; Godbe, J. M.; Sknepnek, R.; Knowles, K. E.; Olvera de la Cruz, M.; Weiss, E. A., A quantitative description of the binding equilibria of para-substituted aniline ligands and CdSe quantum dots. *The Journal of Physical Chemistry C* **2010,** *114* (51), 22526-22534.
8. Morris-Cohen, A. J.; Vasilenko, V.; Amin, V. A.; Reuter, M. G.; Weiss, E. A., Model for adsorption of ligands to colloidal quantum dots with concentration-dependent surface structure. *ACS nano* **2011,** *6* (1), 557-565.
9. Morris-Cohen, A. J.; Malicki, M.; Peterson, M. D.; Slavin, J. W.; Weiss, E. A., Chemical, structural, and quantitative analysis of the ligand shells of colloidal quantum dots. *Chemistry of Materials* **2012,** *25* (8), 1155-1165.
10. Hens, Z.; Martins, J. C., A solution NMR toolbox for characterizing the surface chemistry of colloidal nanocrystals. *Chemistry of Materials* **2013,** *25* (8), 1211-1221.
11. Hassinen, A.; Moreels, I.; de Mello Donegá, C.; Martins, J. C.; Hens, Z., Nuclear magnetic resonance spectroscopy demonstrating dynamic stabilization of CdSe quantum dots by alkylamines. *The Journal of Physical Chemistry Letters* **2010,** *1* (17), 2577-2581.
12. Gomes, R.; Hassinen, A.; Szczygiel, A.; Zhao, Q.; Vantomme, A.; Martins, J. C.; Hens, Z., Binding of phosphonic acids to CdSe quantum dots: a solution NMR study. *The Journal of Physical Chemistry Letters* **2011,** *2* (3), 145-152.
13. Shen, Y.; Tan, R.; Gee, M. Y.; Greytak, A. B., Quantum Yield Regeneration: Influence of Neutral Ligand Binding on Photophysical Properties in Colloidal Core/Shell Quantum Dots. *ACS Nano* **2015,** *9* (3), 3345-3359.
14. Fritzinger, B.; Capek, R. K.; Lambert, K.; Martins, J. C.; Hens, Z., Utilizing Self-Exchange To Address the Binding of Carboxylic Acid Ligands to CdSe Quantum Dots. *Journal of the American Chemical Society* **2010,** *132* (29), 10195-10201.
15. Owen, J. S.; Park, J.; Trudeau, P.-E.; Alivisatos, A. P., Reaction Chemistry and Ligand Exchange at Cadmium−Selenide Nanocrystal Surfaces. *Journal of the American Chemical Society* **2008,** *130* (37), 12279-12281.

16. Knauf, R. R.; Lennox, J. C.; Dempsey, J. L., Quantifying Ligand Exchange Reactions at CdSe Nanocrystal Surfaces. *Chemistry of Materials* **2016,** *28* (13), 4762-4770.
17. Chambrier, I.; Banerjee, C.; Remiro-Buenamañana, S.; Chao, Y.; Cammidge, A. N.; Bochmann, M., Synthesis of Porphyrin–CdSe Quantum Dot Assemblies: Controlling Ligand Binding by Substituent Effects. *Inorganic Chemistry* **2015,** *54* (15), 7368-7380.
18. Bard, A. J.; Faulkner, L. R.; Leddy, J.; Zoski, C. G., *Electrochemical methods: fundamentals and applications*. wiley New York: 1980; Vol. 2.
19. Chen, P. E.; Anderson, N. C.; Norman, Z. M.; Owen, J. S., Tight binding of carboxylate, phosphonate, and carbamate anions to stoichiometric CdSe nanocrystals. *Journal of the American Chemical Society* **2017,** *139* (8), 3227-3236.
20. Anderson, N. C.; Hendricks, M. P.; Choi, J. J.; Owen, J. S., Ligand exchange and the stoichiometry of metal chalcogenide nanocrystals: spectroscopic observation of facile metal-carboxylate displacement and binding. *Journal of the American Chemical Society* **2013,** *135* (49), 18536-18548.
21. Drijvers, E.; De Roo, J.; Martins, J. C.; Infante, I.; Hens, Z., Ligand Displacement Exposes Binding Site Heterogeneity on CdSe Nanocrystal Surfaces. *Chemistry of Materials* **2018,** *30* (3), 1178-1186.
22. Saniepay, M.; Mi, C.; Liu, Z.; Abel, E. P.; Beaulac, R., Insights into the Structural Complexity of Colloidal CdSe Nanocrystal Surfaces: Correlating the Efficiency of Nonradiative Excited-State Processes to Specific Defects. *Journal of the American Chemical Society* **2018,** *140* (5), 1725-1736.
23. Tsui, E. Y.; Hartstein, K. H.; Gamelin, D. R., Selenium Redox Reactivity on Colloidal CdSe Quantum Dot Surfaces. *Journal of the American Chemical Society* **2016,** *138* (35), 11105-11108.
24. Harris, R. D.; Bettis Homan, S.; Kodaimati, M.; He, C.; Nepomnyashchii, A. B.; Swenson, N. K.; Lian, S.; Calzada, R.; Weiss, E. A., Electronic Processes within Quantum Dot-Molecule Complexes. *Chemical Reviews* **2016,** *116* (21), 12865-12919.
25. Cohn, A. W.; Rinehart, J. D.; Schimpf, A. M.; Weaver, A. L.; Gamelin, D. R., Size dependence of negative trion Auger recombination in photodoped CdSe nanocrystals. *Nano letters* **2013,** *14* (1), 353-358.
26. Herr, T.; Noack, J.; Fischer, P.; Tübke, J., 1, 3-Dioxolane, tetrahydrofuran, acetylacetone and dimethyl sulfoxide as solvents for non-aqueous vanadium acetylacetonate redox-flow-batteries. *Electrochimica Acta* **2013,** *113*, 127-133.

CHAPTER 4. EFFECT OF LIGAND COVERAGE ON HYDROGEN EVOLUTION CATALYZED BY COLLOIDAL WSe_2

Significant portions of the following have been previously published[1]

Contributions to this project were made by Dr. Olivia Lenz.

4.1 Introduction

An emerging class of hydrogen evolution reaction (HER) catalysts are transition metal dichalcogenides (TMDs), 2D layered nanomaterials that can reach high current densities at low overpotentials.[2-3] Commonly, these materials, e.g. WSe_2, are synthesized via chemical vapor deposition (CVD)[4-5], chemical vapor transport (CVT)[6] and vapor liquid solid (VLS)[7] methods. These vacuum synthetic methods are more costly, energy intensive and less scalable than solution-phase colloidal syntheses. Intrinsic to colloidal syntheses, and not to the vacuum techniques mentioned above however, is the presence of capping ligands at the material surfaces. These surface ligands can impede catalytic activity by blocking catalyst active sites and alter the electronic structure of the material.[8-10] High temperature annealing is commonly reported to remove the ligands in colloidally prepared samples, but this introduces another costly production step and may alter the material phase and morphology, limiting the ability to exploit catalytically active non-thermodynamic phases for catalysis.

In this chapter, a ligand stripping procedure is reported that removes capping ligands from the edge sites of colloidally synthesized WSe_2 at room temperature with no morphology change as determined by powder X-ray diffraction (PXRD), scanning electron microscopy (SEM), and X-ray photoelectron spectroscopy (XPS), in contrast to annealing the same material. The catalytic activity of the stripped catalyst is greatly enhanced, with the HER overpotential decreasing by up to 180 mV. The mechanism of this improved catalytic activity is explored using a combination of electrochemical methods demonstrating an increase in intrinsic catalytic capability, beyond the expected increase in electroactive surface area.

4.2 Results and discussion

4.2.1 Synthesis and preparation of WSe_2 deposited electrodes

The WSe_2 nanocrystals are synthesized through a colloidal solution phase method utilizing WCl_4 and 1,3-diethyl-imidazolidine-2-selenone as the W and Se precursors, respectively, and dodecylamine as the solvent and capping ligand. SEM imaging reveals a plate-like morphology, which is expected due to the sheet-like crystal structure predicted for the transition metal dichalcogenide class of materials (Figure 4.1). Analysis by XRD indicates that the WSe_2 is intercalated with dodecylamine until the material is annealed above temperatures of 400 ºC (Figure 4.2). As WSe_2 exists in two polytypes, 1T (octahedral, metallic) and 2H (trigonal prismatic, semiconducting), we have used XPS to determine the major polytype in our samples. For the samples with intercalated amines, the 1T polytype is dominant, and after annealing the WSe_2 becomes more 2H in character (See Experimental Figure 18), consistent with the relative thermodynamics of the two phases. Most commonly, the 1T polytype is only achieved through lithium intercalation and exfoliation of bulk 2H samples, thus this synthesis is advantageous in offering an alternative one-step process for fabricating preferentially 1T WSe_2.

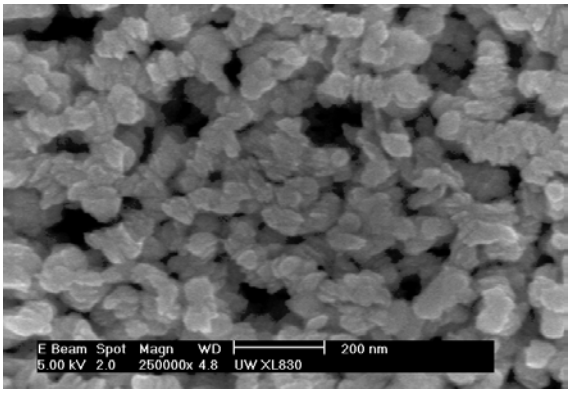

Figure 4.1. SEM of WSe_2 nanocrystal

We chose to chemically (as opposed to thermally) remove the ligands on the surface through treatment with triethyloxonium tetrafluoroborate (Meerwein's reagent), which has been shown to be an effective method for removing a variety ligands from semi-conductor surfaces.[11] Successful removal of

primary amine ligands from nanomaterials using Meerwein's reagent has been demonstrated, with a proposed mechanism of amine removal via alkylation to the quaternary ammonium cation.[12-18] Scheme 4.1 summarizes the proposed reaction chemistry at the surface of WSe_2.

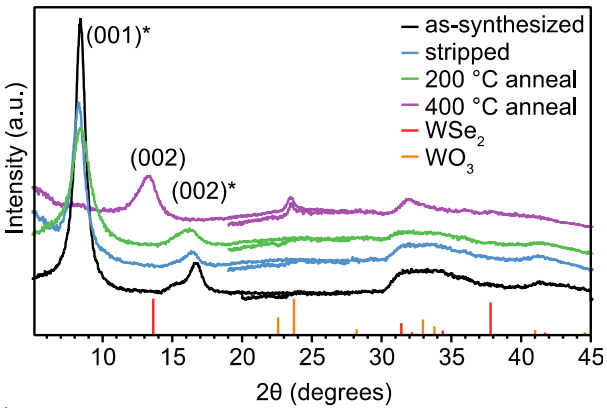

Figure 4.2. PXRD of as synthesized, Meerwein's treated (stripped) and annealed WSe_2 overlayed with reference WSe_2 and WO_3 diffraction data

The as-prepared WSe_2 was loaded onto carbon fiber electrodes by drop casting from a toluene solution. These samples were then dipped into a solution of 0.1 M Meerwein's reagent in MeCN for 30 seconds and then rinsed with MeCN. To confirm the removal of amine, thermogravimetric analysis (TGA) was used to analyze the mass fraction of amine in as-synthesized and stripped samples (Figure 4.3). This analysis shows a 3% decrease in amine content (by weight) of the samples treated with Meerwein's reagent. This suggests that the majority of the amine is still present in an intercalated form non-covalently bound between the electron-rich chalcogen-terminated layers (confirmed by PXRD, Figure 4.2). In addition, analysis of FTIR (Figure 4.4) shows that the WSe_2 treated with Meerwein's reagent still has amine present, whereas annealing removes all ligands.

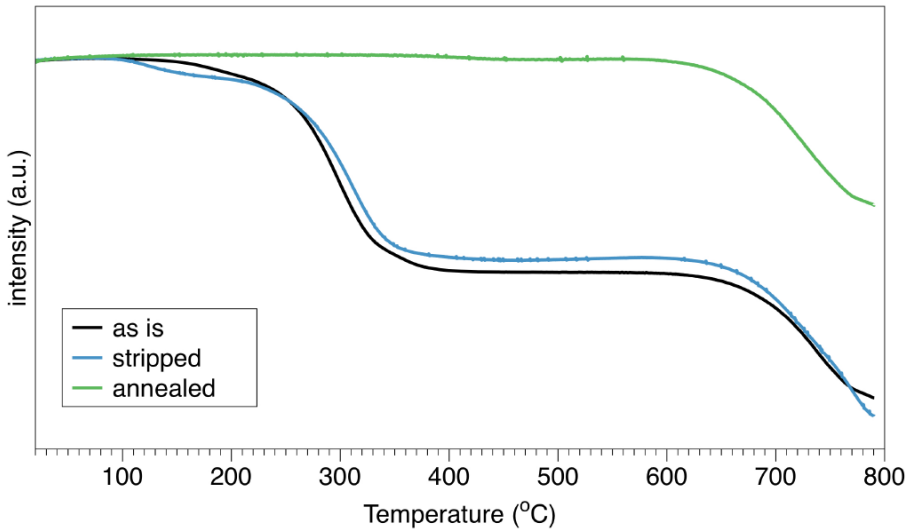

Figure 4.3. TGA of WSe_2 as synthesized, stripped (Meerwein's treated) and annealed

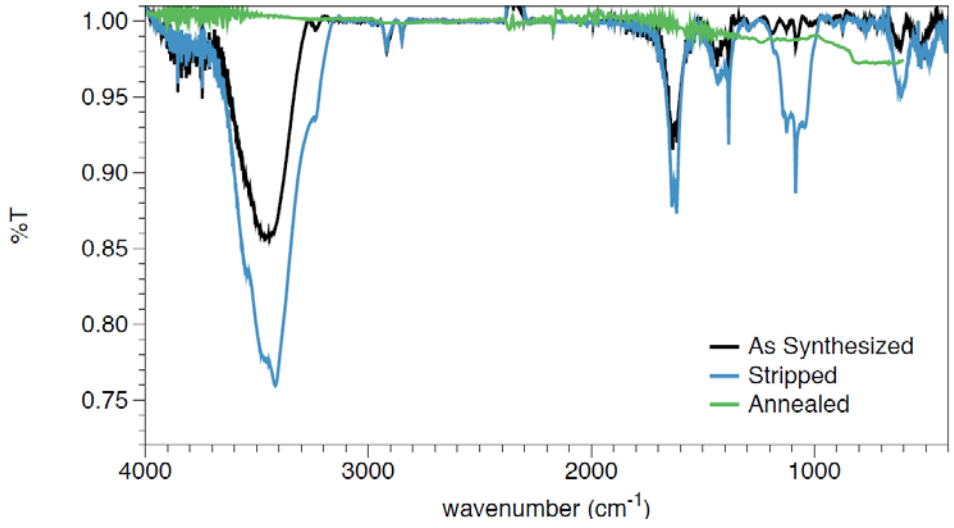

Figure 4.4. FTIR of WSe_2 as synthesized, stripped (Meerwein's treated) and annealed

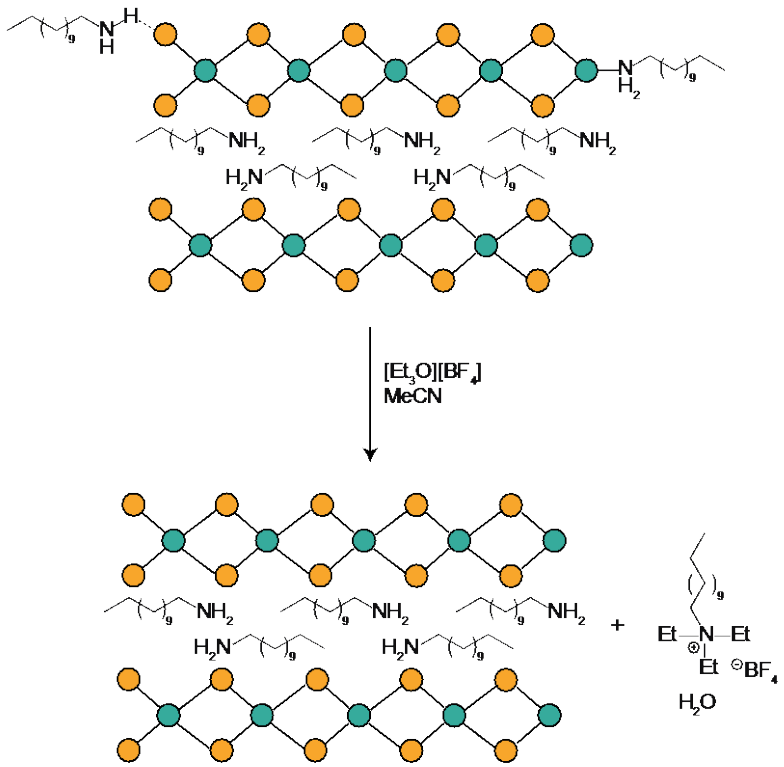

Scheme 4.1. Illustration of ligand removal by Meerwein's reagent. Intercalated ligands are not affected.

4.2.2 Electrochemical measurements on WSe_2 electrodes

Electrochemical measurements were conducted on carbon fiber electrodes that were loaded as described above. Treatment of the WSe_2 electrodes with Meerwein's reagent was found to have a significant impact on the overpotential of the HER in 0.5 M H_2SO_4 (Figure 4.5) as evident in the linear sweep voltammogram (LSV). In order to ensure that the all the amine on the surface that would impact the hydrogen evolution catalysis has been removed, a concentration study of Meerwein's reagent (0.01, 0.1 and 1.0M) was conducted (Figure 4.5). When attempting to remove ligands with 0.01M Meerwein's reagent there is no noticeable change in the LSV and for 0.1M and 1.0M Meerwein's reagent, there is no change as well. Therefore we have used 0.1M Meerwein's reagent in the following electrochemical studies.

In Figure 4.6a, the change in overpotential (Δ_{OP}) is 118 mV (at 10 mA/cm^2_{geo}) upon removal of amines. In addition to Δ_{OP}, the Tafel slope decreases from 155 to 121 mV/decade upon treatment with Meerwein's reagent (Figure 4.6b). Tafel slope analysis can give insight into a mechanism if the slopes are specific and resistance of the material does not manifest in the slope,[19] however it generally is a measure of how much driving force (potential) is needed to increase the rate (current) by a factor of 10. In semiconductors, a decreased Tafel slope can result from increased HER kinetics, for example from increased electron transport through the material.[20]

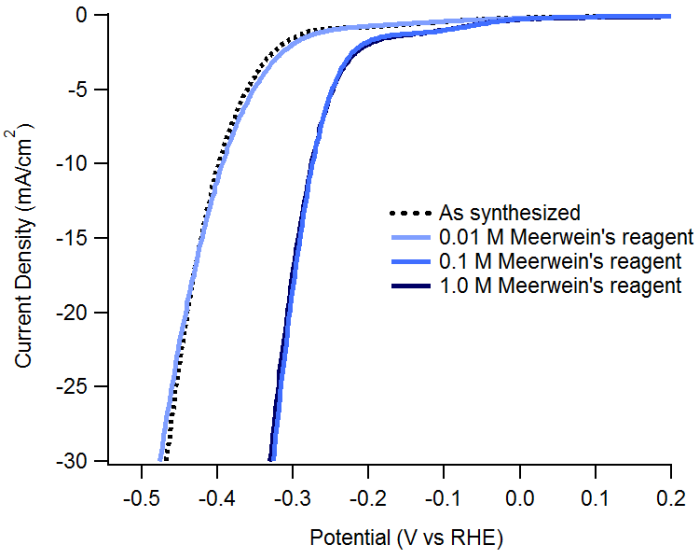

Figure 4.5.Concetration study of Meewein's reagent and the effect on overpotential

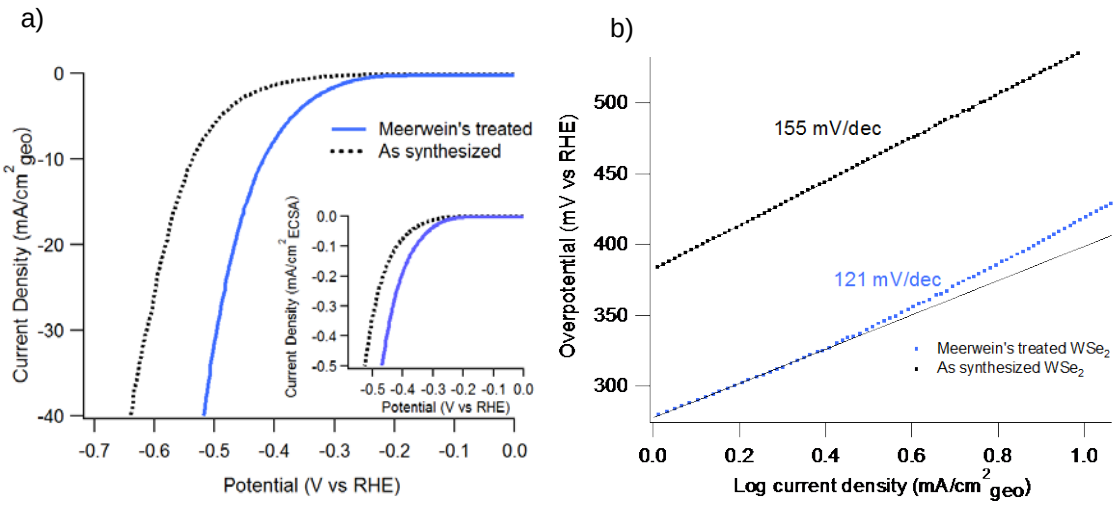

Figure 4.6. a) LSV of WSe_2 deposited on a carbon fiber electrode before (dashed black line) and after treatment with Meerwein's reagent (solid blue line) in 0.5M H_2SO_4, inset depicts the same LSV corrected for ECSA calculated by CV. b) Tafel slope analysis on the LSV traces in a).

In order to determine if the effect of Meerwein's reagent is reversible, the treated electrode was soaked in a solution of 0.1 M dodecylamine in MeCN. The resulting LSVs show subsequent exposures to

the dodecylamine solution results in increasing overpotentials (Figure 4.7a) and increasing Tafel slopes. Starting with the initial Tafel slope of 154 for the Meerwein's treated WSe_2, this slope increases to 162, 165 and 173 mV/dec upon subsequent exposures (Figure 4.7b). This experiment further supports the causal relationship between surface-bound, non-intercalated amine and the decreased catalytic activity of colloidally prepared WSe_2.

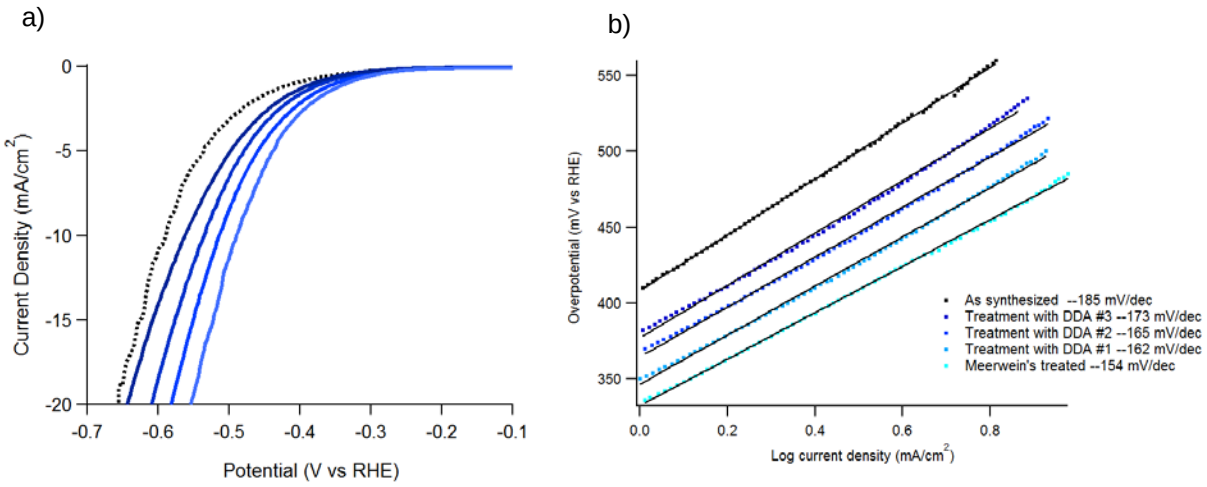

Figure 4.7. a) LSVs of increasing amounts of amine religated on the surface of WSe_2 electrode. The as synthesized (dashed black) and the Meerwein's (lightest blue) show the outermost traces. As the electrode is exposed to more dodecylamine (darker blue), the LSVs b) Tafel slopes with increasing treatment with DDA

We expected that the removal of the dodecylamine ligands would result in an increased surface area of the WSe_2 electrode.[9-10] We calculated the electrochemically active surface area (ECSA), which measures the area that is accessible for electrode reactions.[21] The ECSA is measured at potentials where only double layer charging and discharging are occurring. In this region, the resulting current is a product of the scan rate and the capacitance of the double layer, C_{DL}.[22] Comparing the electroactive surface area of the Meerwein's reagent treated electrode to the as-synthesized electrode, we see an increase in the ECSA from 17.6 to 40.8 cm^2 (Figure 4.8). Correcting the LSV data for this surface area increase (Figure 4.2a, inset) there is still a 62 mV overpotential difference (at 5 mA/cm^2_{ECSA}) not accounted for by surface area alone.

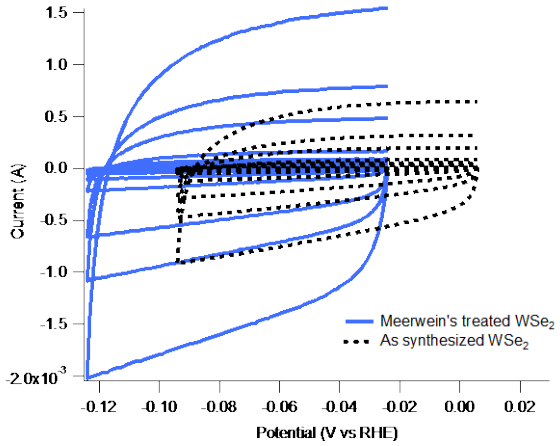

Figure 4.8. Cyclic voltammograms (10, 25, 50,100, 300, 500, and 1,000 mV/s) of as synthesized and Meerwein's treated WSe_2 electrodes showing an increased C_{DL} and therefore electrochemically active surface area for the Meerwein's treated WSe_2

4.2.3 Electrochemical Impedance Spectroscopy on as synthesized WSe_2 and Meerwein's treated WSe_2 electrodes.

To further probe the effects of the Meerwein's reagent treatment on the HER catalyzed by WSe_2, electrochemical impedance spectroscopy (EIS) was performed on the as-synthesized and Meerwein's treated WSe_2 loaded electrodes (Figure 4.9) at potentials ranging from 344 to 394 mV vs RHE. To fit the spectra, we used a modified Randles circuit [21, 23] (Figure 4.10). The values from the fit to this equivalent circuit across the potential range are summarized in Table 4.1. Here R_{CT} represents the charge transfer resistance of the HER process, C_{CT} represents the pseudocapacitance of H_{ad}, R_C represents the resistance of contact between the carbon fiber electrode and the deposited WSe_2, R_S is the solution resistance and C_{DL} is the double layer capacitance.[23] We found that with stripping, the R_{CT} decreases from 53 to 23 Ω at 344 mV vs RHE (Figure 4.11). The R_{CT} is a measure of how fast the rate of electron-transfer responds to a change in potential. The Tafel slope reflects the R_{CT} under steady state conditions.[24]

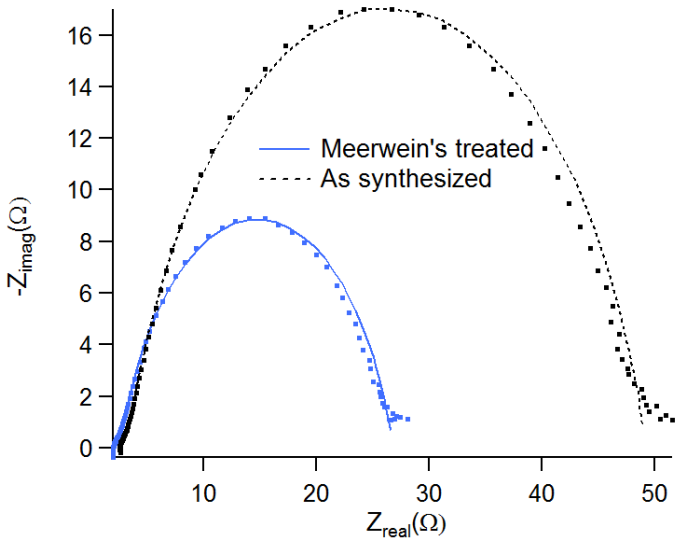

Figure 4.9. Nyquist plots for the as synthesized and Meewein's treated WSe2 electrodes at -344mV vs RHE

In addition to decreases in R_{CT}, other parts of the equivalent circuit were affected. Average resistance values for R_C across this potential range decreased from 1.5 to 1.0 Ω, indicating the resistance from the contact with the electrode has decreased, presumably a side-effect of some residue ligand sandwiched between the electrode and the WSe_2. The average solution resistance across this potential range from the working to the reference electrode, R_S, also decreased from 2.5 Ω to 1.9 Ω.This is likely due to the increase in surface area, allowing charge to move through more working electrode area.

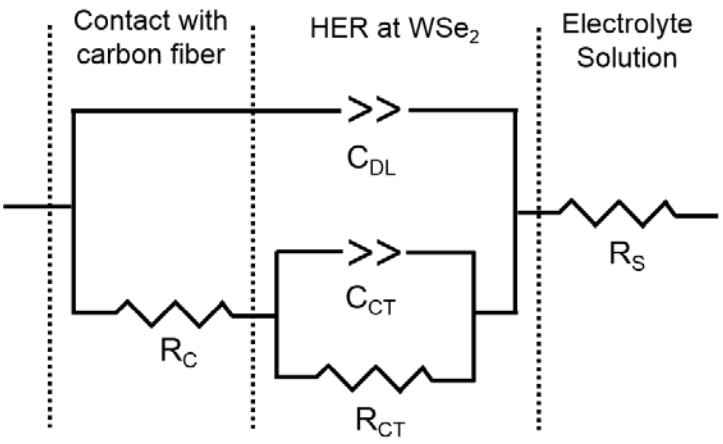

Figure 4.10. Equivalent circuit used to fit the electrochemical impedance spectra

Table 4.1. Fit values from EIS data fit to equivalent circuit in Figure 4.7

As synthesized							Treated with Meerwein's reagent					
E/mV	R_C/Ω	R_{CT}/Ω	C_{CT}/mF	C_{DL}/mF	R_S/Ω	R_P/cm^2 ECSA	R_C/Ω	R_{CT}/Ω	C_{CT}/mF	C_{DL}/mF	R_S/Ω	R_P/cm^2 ECSA
344	1.441	52.9	0.47	0.17	2.56	3.0	1.148	23.15	1.51	0.467	2.03	0.6
354	1.428	45.2	0.52	0.15	2.57	2.6	1.267	23.55	1.40	0.526	1.98	0.6
364	1.371	36.6	0.56	0.18	2.58	2.1	0.892	17.18	1.88	0.450	1.93	0.4
374	1.675	31.9	0.52	0.22	2.57	1.8	0.905	15.62	1.88	0.453	1.89	0.4
384	1.715	28.1	0.54	0.23	2.56	1.6	0.948	14.08	1.82	0.538	1.84	0.3
394	1.413	24.2	0.60	0.21	2.59	1.4	0.958	12.46	1.86	0.533	1.82	0.3

The values calculated for C_{DL} by EIS can be used to determine relative increases of surface area even in the overpotential region.[21] The average calculated values for C_{DL} increase from 0.20 to 0.50 mF

across this potential range (Table 4.1). This is an increase in surface area of 2.5x, in agreement with the relative increase in surface area from the ECSA measurements determined by cyclic voltammetry (2.3x). The C_{CT} values, corresponding to the pseudocapacitance of adsorbed intermediates, also increases from an average of 0.54 to 1.73 mF upon application of Meerwein's reagent.

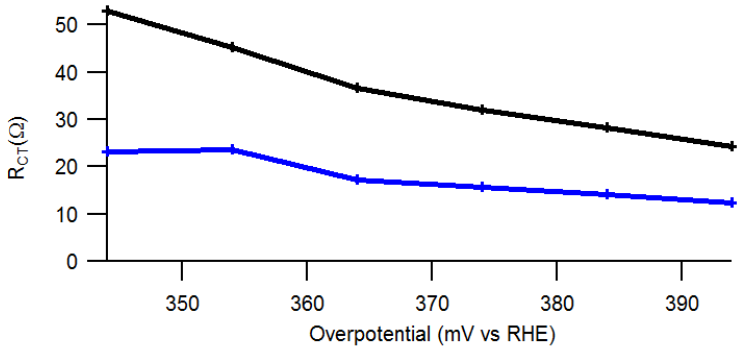

Figure 4.11. Calculated values for R_{CT} from Figure 4.6 and the equivalent circuit in Figure 4.7

In order to make comparisons according to surface area site, the R_{CT} at 344 mV values were corrected for surface area, application of Meerwein's reagent to the WSe_2 decreases the R_{CT}*mF from 11.5 to 10.6 Ω*mF at 354 mV (Figure 4.11). This suggests that the kinetics of HER are faster on the Meerwein's reagent treated WSe_2 per surface area site. Tafel slope analysis was also performed using R_{CT} values for the as-synthesized and Meerwein's treated WSe_2 (Figure 4.12). The Tafel slope for the as-synthesized WSe_2 was found to be 138mV/dec by this method, which is lower than the 151mV/dec calculated from the LSV data. This lower Tafel slope determined from the EIS data reflects sources of uncompensated resistance being removed from the analysis, likely from increased electron transport through the material. In contrast, the Tafel slope, from the Meerwein's treated WSe_2 was found to be 118 mV/dec, similar to the 121 mV/dec found from the LSV.

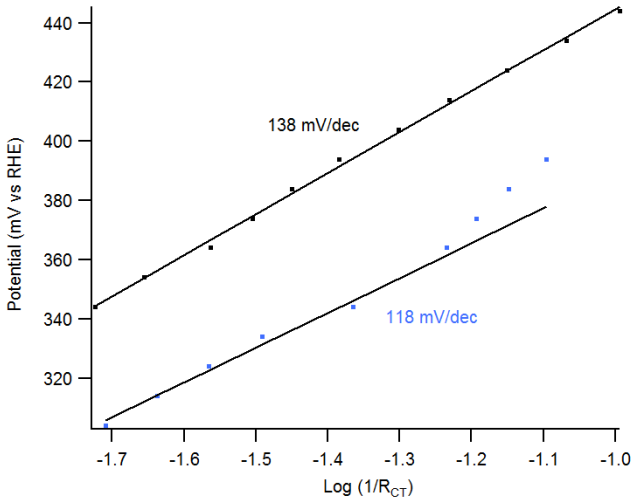

Figure 4.12. Tafel slopes derived from R_{CT} values from the equivalent circuit

4.2.4 Exploration into intrinsic catalytic activity of Meerwein's treated WSe_2

We believe the increase in the surface area is not enough to account for the increase in catalytic activity of Meerwein-treated samples. For MoS_2, an increase in ECSA by a factor of 100 only led to a decrease in overpotential of less than 30 mV.[25] In this work, we see a modest increase in surface area (2.3-2.5x), which we attribute solely to the removal of ligands, and a difference in overpotential of 118 mV. This led us to investigate how the electronic structure, and consequently ΔG_H is changing, perhaps leading to an increase in intrinsic catalytic activity of the Meerwein's treated material.

WSe_2 likely undergoes HER in a H_{ad} consuming step (Heyrovsky or Tafel) as the rate determining step, given that the measured Tafel slopes fall in a range that spans below 120 mV/dec (indicative of a Volmer mechanism) (See Experimental Figure 19). The relationship between current density (rate) and overpotential for the Heyrovsky step (for the Tafel step, the θ term is squared) is seen in Equation 4.1. An increase in current density at the same overpotential (at a given $[H^+]$) is related to θ (coverage of H_{ad} per available active site) and $\Delta G_{H,}$ the Gibbs free energy of adsorption of the H_{ad} resulting from the Volmer step.[19] Here β is the Brønsted-Evans-Polanyi (BEP) coefficient and α is the transfer coefficient.[26] From

this expression we can see that a decrease in ΔG_H will increase the rate of a reaction with a H_{ad} consuming step.

$$\nu = k^0[H^+]\theta_H \exp\left(\frac{-\alpha F E_{SHE} + (1-\beta)\Delta G_H}{RT}\right) \qquad \text{Equation 3.1}$$

To probe ΔG_H we utilized ultraviolet photoelectron spectroscopy (UPS). In the Fermi energy region of the UPS spectra, we find that the Meerwein's treated WSe_2 valence band maximum (VBM) lies 0.688 eV below E_F, while the VBM of the as-synthesized WSe_2 is 0.385 eV below E_F (Figure 4.13).

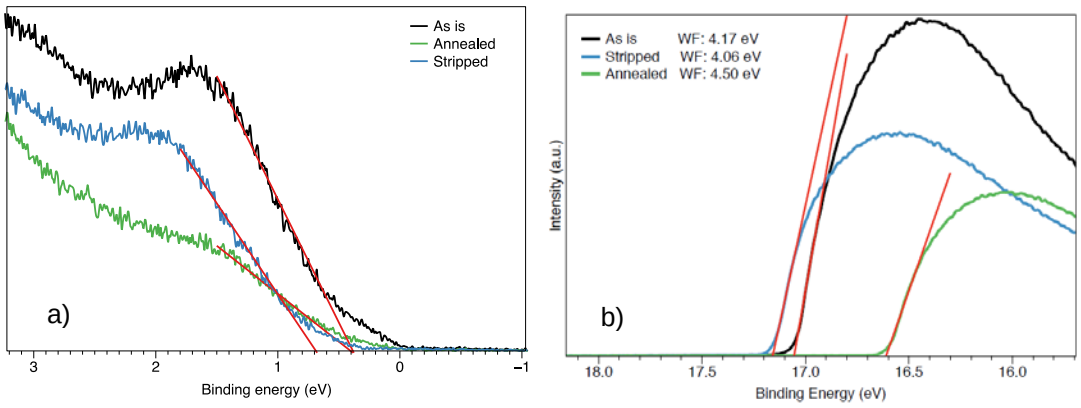

Figure 4.13: UPS plots of the as synthesized and stripped samples. a) depicts the spectra region used to calculate the distance between the VBM and the E_F b) depicts the spectra region used to measure the work function (WF)

The distance between the d-band center and E_F has frequently been related to the M-H bond strength and/or ΔG_H.[26] This can be conceptualized with a qualitative band diagram (Figure 4.14), which for this purpose keeps the E_F fixed. While we recognize that our WSe_2 sample is not a pure metal, generally for TMDCs the d-bands are the most significant contributor to valence band maximum region and in this discussion we will use them interchangabely.[27-28] According to trends developed for metallic HER catalyst, the higher the d states relative to the E_F, the stronger the M-H bond.[29] This indicates that the as-synthesized WSe_2, with the smaller (E_d-E_F) distance, has fewer filled antibonding states than the Meerwein's treated WSe_2. Less filled antibonding states leads to a stronger bond, leading to the conclusion that for our samples, the as-synthesized WSe_2 should have a stronger M-H bond than the Meerwein's

treated WSe_2. If we use the relationship for metal catalysts that a weaker M-H bond corresponds to a more thermoneutral ΔG_H, then we would expect the Meerwein's treated WSe_2 to produce a higher exchange current density (log j_0) than the as-synthesized WSe_2.[26] This fits the trend we see with our samples from the Tafel plots, where the Meerwein's treated WSe_2 has an exchange current density of 0.018 mA/cm^2 compared to 0.006 mA/cm^2 of the as-synthesized WSe_2. The work function of the Meerwein's treated WSe_2 is lower at 4.06 eV (higher E_F) than in the as synthesized WSe_2 at 4.17 eV. This data suggests that the dodecylamine ligands contribute to removing electron density from the surface- possibly in the form of Se-H interactions seem in Scheme 4.1.

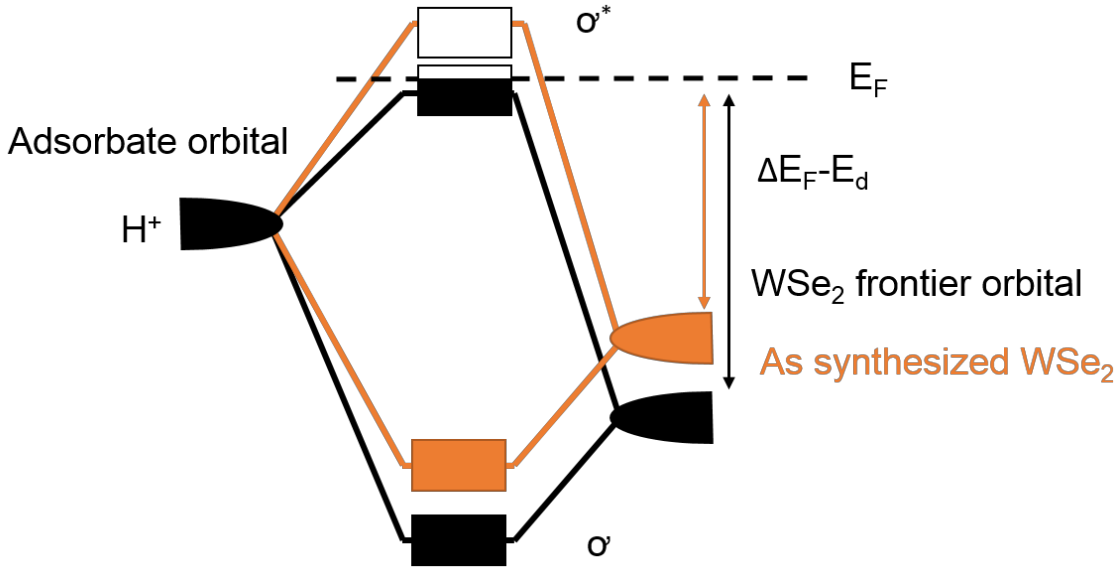

Figure 4.14. Qualitative frontier orbital and adsorbate orbital diagram showing the bonding and antibonding orbitals resulting from bond formation with respect to the E_F

4.2.5 Other considerations to catalysis- oxide formation, loading effects and stability

The specific effect of Meerwein's reagent on the overpotential of HER catalyzed by WSe_2 is also influenced by material preparation. If the WSe_2 is post-synthetically worked up in air, an appreciable amount of oxide (indicated by the presence of W^{6+}) is observed by XPS (Figure 4.15).

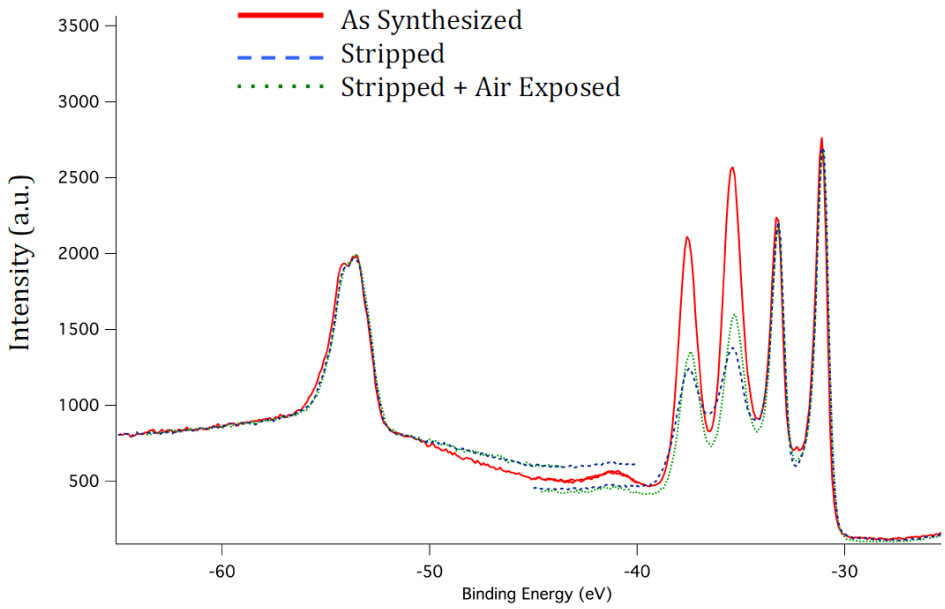

Figure 4.15. XPS spectra demonstrating that upon treatment with Meerwein's reagent, the 4f (VI) binding area is decreased, indicating the W^{6+} in the form of oxides is decreasing. Upon air exposure these peaks begin to increase again.

Comparatively, samples processed under air-free conditions have a minimal W^{6+} content. We found that the Meerwein's reagent treatment decreases the oxide content if samples worked up in air (Figure 4.15). This is notable in that oxides are generally removed via harsher etching reagents such as hydrazine and HF, harsher and more toxic reagents than Meerwein's reagent.

With these oxide containing samples, we conducted a loading study where we systematically added more of the WSe_2 suspension to the electrode between LSV scans. We observed a decrease in overpotential with higher loading until a point when the trend reversed, presumably due to significant resistance within layers of the deposited material (Figure 4.16).[20, 23] Upon treatment of the oxide-containing samples with Meerwein's reagent Δ_{OP} was found to range from 118 to 180 mV as a function of loading (Figure 4.16). The ECSA of the oxide containing sample also had a greater increase in surface area (5.4x) than the non-oxide containing samples, indicating that the W^{6+} is not as catalytically active as the W^{4+} and removal of the oxide exposes more active sites (See Experimental Figure 4.20).

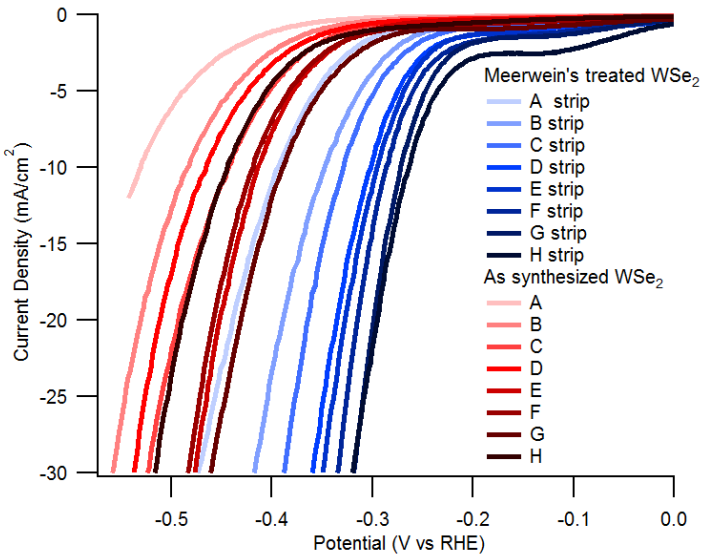

Figure 4.16. LSVs of WSe_2 electrodes with different loadings and after subsequent treatment with Meerwein's reagent

The long-term stability of the WSe_2 was also explored by subsequent electrolyses under -10mA/cm^2 for 5 hours and the LSVs are shown in Figure 4.16 after each 1 hour electrolyses. The activity at -10mA/cm^2 decreases by ~75mV in this time.

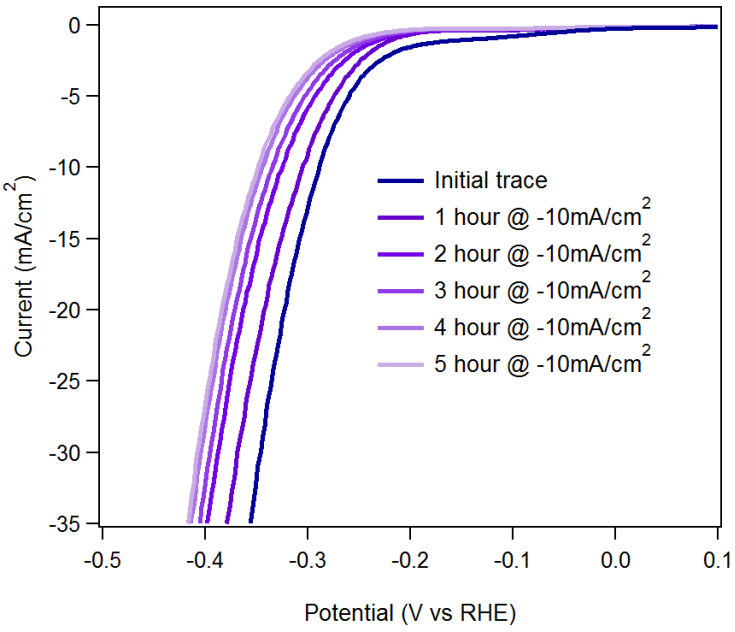

Figure 4.17. LSVs of WSe_2 electrodes after 1 hour electrolyses at -10 mA/cm^2

4.3 Conclusions

In conclusion, we have demonstrated that Meerwein's reagent is an effective and facile chemical ligand removal strategy that does not require any air-free techniques or high temperatures. This method enables the retention of surfaces and phases straight from synthesis that might be altered by heat in the thermal annealing process common to other studies. In addition, we have investigated the role of dodecylamine ligand coverage on WSe_2 for the HER. We demonstrate that the ligands bound to the surface reduce the kinetics of the HER as seen by EIS and Tafel slope analysis. We also demonstrate that the intrinsic catalytic capability of the WSe_2 per surface site increases. Post synthetic surface modification of colloidally-prepared WSe_2 using Meerwein's reagent offers a simple approach to modifying the ligand coverage and accessing electrocatalysts with improved overpotential and intrinsic catalytic reactivity.

4.4 Experimental

4.4.1 General considerations

Tungsten tetrachloride (WCl_4, Strem, stored in glovebox), dodecylamine (DDA, TCI America, distilled and stored in glovebox), diphenyl ether (distilled and stored in glovebox), triethyl orthoformate (TCI America), ethane-1,2-diamine (TCI America), selenium powder (Se, Sigma Aldrich, 200 mesh), acetonitrile (MeCN, Sigma Aldrich, anhydrous), and triethyloxonium tetrafluoroborate (Et_3OBF_4, Sigma Aldrich) are used as received unless otherwise noted. Solutions used for electrochemical measurements were 99.999% H_2SO_4 (Sigma Aldrich) in 18MΩ Millipore H_2O.

Electrochemical characterization

All electrochemical measurements were conducted in a custom four-neck cell fitted with a platinum coil auxiliary electrode separated in a fritted compartment, a $Ag/AgSO_4$ reference electrode separated by a Vycor frit and a working electrode and at a scan rate of 5 mV/s. The working electrodes used in this study were fabricated from carbon paper (Fuel Cell Store, Spectracarb 2050A 0850). The carbon fiber electrodes were made by cutting a 1 cm x 3 cm rectangle and attaching a copper wire with silver epoxy to the electrode material. The copper wire/silver epoxy was then covered with gel epoxy to create a 1 cm x 1 cm surface area. (Note: the backside of the electrode was not covered due to its porosity with epoxy leaking onto both sides.)

All cyclic voltammograms depicting proton reduction were performed after sparging the cell with Ar or N_2. The electrolyte solution is 0.5 M H_2SO_4 in 18 MΩ Millipore water. All measurements in this study was referenced to RHE, which was measured using a platinum coil electrode in H_2 saturated 0.5 M H_2SO_4.

Tafel slope analysis was performed on LSVs with 5 mV/s scan rate from the onset of the reductive current to ~150mV after the onset and fitted to a best fit line. In cases where the fit wasn't linear in this region, the line was fit to the initial linear portion of the curve.

A Gamry Interface 1000 was used for all electrochemical measurements. The frequency range for EIS measurements was 0.1Hz to 500 kHz with 14 points per decade. Measurements were taken with 5.3 mV rms AC voltage.

Cyclic voltammograms for electrochemically active surface area (ECSA) measurements were taken in a 100 mV range around the open circuit potential. The ECSA was calculated from the following equation, $A = \frac{C_{DL}}{C_S}$. The average capacitances from the oxidative and reductive currents were used for C_{DL}. The average general capacitance, C_s, used was 0.035 mF/cm^2.[2,3]

Loading the electrodes involved a 20-100 µL aliquot of WSe_2/toluene slurry applied to the carbon fiber electrodes. For multiple applications, the first was allowed to dry, before reapplying. If necessary, the solution was sonicated beforehand. For the nonoxide, containing samples, the electrodes were dipped into Meerwein's reagent in an Ar atmosphere and then placed into Ar or N_2 sparged 0.5M H_2SO_4 solution.

4.4.2 XPS of as synthesized and annealed WSe_2

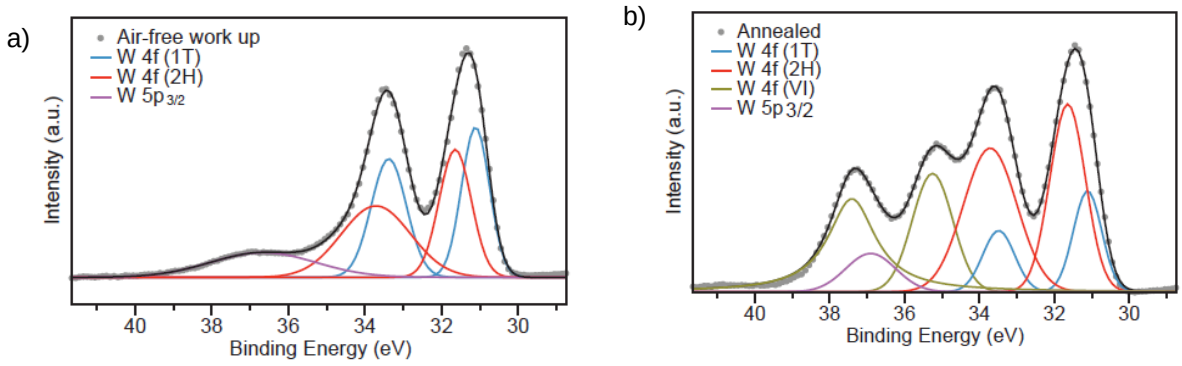

Figure 4.18. a) WSe_2 as synthesized is majority 1T b) after annealing the 2H content is increased

4.4.3 Tafel slopes from higher loaded WSe_2 electrode

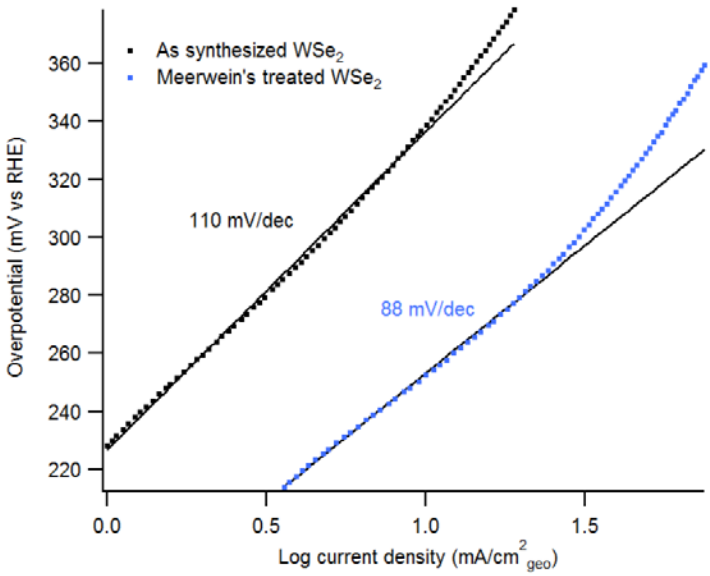

Figure 4.19. Tafel slopes from higher-loaded WSe_2 electrodes demonstrating a Tafel slope below 120mV/dec

4.4.4 Cyclic voltammograms for oxide-containing WSe_2 electrodes before and after Meerwein's treatment

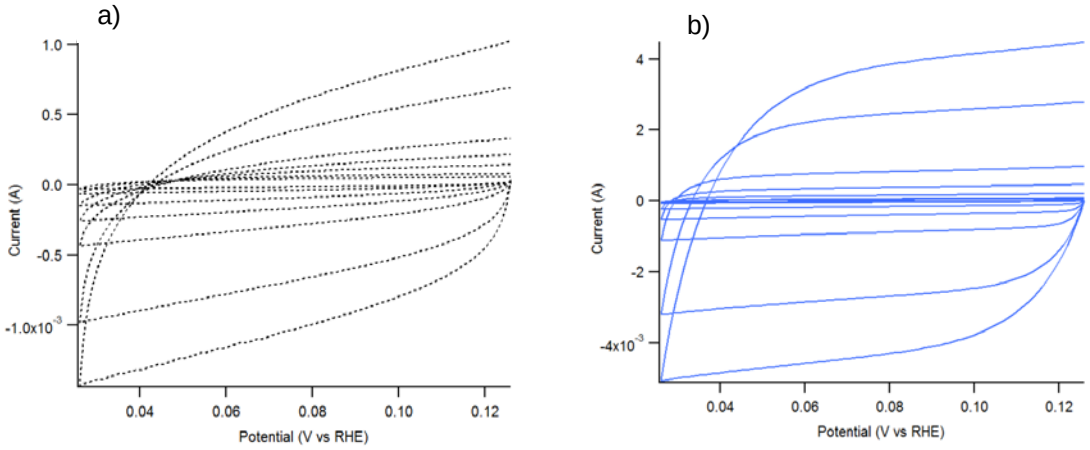

Figure 4.20. Cyclic voltammograms (10, 25, 50,100, 300, 500, and 1,000 mV/s) of a) as synthesized oxide-containing WSe_2 electrodes and b) Meerwein's treated oxide- containing WSe_2 electrodes showing an increased C_{DL} and therefore electrochemically active surface area for the Meerwein's treated WSe_2

4.5 References

1. Henckel, D. A.; Lenz, O.; Cossairt, B. M., Effect of Ligand Coverage on Hydrogen Evolution Catalyzed by Colloidal WSe_2. *ACS Catalysis* **2017,** *7* (4), 2815-2820.
2. Morales-Guio, C. G.; Stern, L.-A.; Hu, X., Nanostructured hydrotreating catalysts for electrochemical hydrogen evolution. *Chemical Society Reviews* **2014,** *43* (18), 6555-6569.
3. Kong, D.; Cha, J. J.; Wang, H.; Lee, H. R.; Cui, Y., First-row transition metal dichalcogenide catalysts for hydrogen evolution reaction. *Energy & Environmental Science* **2013,** *6* (12), 3553-3558.
4. Zou, M.; Zhang, J.; Zhu, H.; Du, M.; Wang, Q.; Zhang, M.; Zhang, X., A 3D dendritic WSe2 catalyst grown on carbon nanofiber mats for efficient hydrogen evolution. *Journal of Materials Chemistry A* **2015,** *3* (23), 12149-12153.
5. Wang, F.; Li, J.; Wang, F.; Shifa, T. A.; Cheng, Z.; Wang, Z.; Xu, K.; Zhan, X.; Wang, Q.; Huang, Y.; Jiang, C.; He, J., Enhanced Electrochemical H_2 Evolution by Few-Layered Metallic WS2(1−x)Se2x Nanoribbons. *Advanced Functional Materials* **2015,** *25* (38), 6077-6083.
6. Velazquez, J. M.; Saadi, F. H.; Pieterick, A. P.; Spurgeon, J. M.; Soriaga, M. P.; Brunschwig, B. S.; Lewis, N. S., Synthesis and hydrogen-evolution activity of tungsten selenide thin films deposited on tungsten foils. *Journal of Electroanalytical Chemistry* **2014,** *716*, 45-48.
7. Wang, H.; Kong, D.; Johanes, P.; Cha, J. J.; Zheng, G.; Yan, K.; Liu, N.; Cui, Y., $MoSe_2$ and WSe_2 Nanofilms with Vertically Aligned Molecular Layers on Curved and Rough Surfaces. *Nano Letters* **2013,** *13* (7), 3426-3433.
8. Smith, J. G.; Jain, P. K., The Ligand Shell as an Energy Barrier in Surface Reactions on Transition Metal Nanoparticles. *Journal of the American Chemical Society* **2016,** *138* (21), 6765-6773.

9. Li, D.; Wang, C.; Tripkovic, D.; Sun, S.; Markovic, N. M.; Stamenkovic, V. R., Surfactant Removal for Colloidal Nanoparticles from Solution Synthesis: The Effect on Catalytic Performance. *ACS Catalysis* **2012,** *2* (7), 1358-1362.
10. Liu, Z.; Shamsuzzoha, M.; Ada, E. T.; Reichert, W. M.; Nikles, D. E., Synthesis and activation of Pt nanoparticles with controlled size for fuel cell electrocatalysts. *Journal of Power Sources* **2007,** *164* (2), 472-480.
11. Rosen, E. L.; Buonsanti, R.; Llordes, A.; Sawvel, A. M.; Milliron, D. J.; Helms, B. A., Exceptionally Mild Reactive Stripping of Native Ligands from Nanocrystal Surfaces by Using Meerwein's Salt. *Angewandte Chemie International Edition* **2012,** *51* (3), 684-689.
12. Lynch, J.; Giannini, C.; Cooper, J. K.; Loiudice, A.; Sharp, I. D.; Buonsanti, R., Substitutional or Interstitial Site-Selective Nitrogen Doping in TiO_2 Nanostructures. *The Journal of Physical Chemistry C* **2015,** *119* (13), 7443-7452.
13. Nikolaev, K.; Ermakov, S.; Ermolenko, Y.; Averyaskina, E.; Offenhausser, A.; Mourzina, Y., A novel bioelectrochemical interface based on in situ synthesis of gold nanostructures on electrode surfaces and surface activation by Meerwein's salt. A bioelectrochemical sensor for glucose determination. *Bioelectrochemistry* **2015,** *105*, 34-43.
14. Nikolaev, K. G.; Ermakov, S. S.; Offenhäusser, A.; Mourzina, Y., Activation of gold nanostructures with Meerwein's salt. *Mendeleev Communications* **2014,** *24* (3), 145-146.
15. Palomaki, P. K.; Miller, E. M.; Neale, N. R., Control of plasmonic and interband transitions in colloidal indium nitride nanocrystals. *J Am Chem Soc* **2013,** *135* (38), 14142-50.
16. Rosen, E. L.; Buonsanti, R.; Llordes, A.; Sawvel, A. M.; Milliron, D. J.; Helms, B. A., Exceptionally mild reactive stripping of native ligands from nanocrystal surfaces by using Meerwein's salt. *Angew Chem Int Ed Engl* **2012,** *51* (3), 684-9.
17. Suehiro, S.; Horita, K.; Kumamoto, K.; Yuasa, M.; Tanaka, T.; Fujita, K.; Shimanoe, K.; Kida, T., Solution-Processed Cu_2ZnSnS_4Nanocrystal Solar Cells: Efficient Stripping of Surface Insulating Layers Using Alkylating Agents. *The Journal of Physical Chemistry C* **2014,** *118* (2), 804-810.
18. Suehiro, S.; Horita, K.; Yuasa, M.; Tanaka, T.; Fujita, K.; Ishiwata, Y.; Shimanoe, K.; Kida, T., Synthesis of Copper-Antimony-Sulfide Nanocrystals for Solution-Processed Solar Cells. *Inorg Chem* **2015,** *54* (16), 7840-5.
19. Shinagawa, T.; Garcia-Esparza, A. T.; Takanabe, K., Insight on Tafel slopes from a microkinetic analysis of aqueous electrocatalysis for energy conversion. *Scientific Reports* **2015,** *5*, 13801.
20. Vrubel, H.; Moehl, T.; Gratzel, M.; Hu, X., Revealing and accelerating slow electron transport in amorphous molybdenum sulphide particles for hydrogen evolution reaction. *Chemical Communications* **2013,** *49* (79), 8985-8987.
21. Bai, L.; Gao, L.; Conway, B. E., Problem of in situ real-area determination in evaluation of performance of rough or porous, gas-evolving electrocatalysts. Part 2.-Unfolding of the electrochemically accessible surface of rough or porous electrodes: a case-study with an electrodeposited porous Pt electrode. *Journal of the Chemical Society, Faraday Transactions* **1993,** *89* (2), 243-249.
22. Trasatti, S.; Petrii, O. A., Real surface area measurements in electrochemistry. *J. Electroanal. Chem.* **1992,** *327* (1-2), 353-76.
23. Morales-Guio, C. G.; Liardet, L.; Hu, X., Oxidatively Electrodeposited Thin-Film Transition Metal (Oxy)hydroxides as Oxygen Evolution Catalysts. *Journal of the American Chemical Society* **2016,** *138* (28), 8946-8957.
24. Harrington, D. A., The rate-determining step in electrochemical impedance spectroscopy. *Journal of Electroanalytical Chemistry* **2015,** *737*, 30-36.
25. Benck, J. D.; Chen, Z.; Kuritzky, L. Y.; Forman, A. J.; Jaramillo, T. F., Amorphous Molybdenum Sulfide Catalysts for Electrochemical Hydrogen Production: Insights into the Origin of their Catalytic Activity. *ACS Catalysis* **2012,** *2* (9), 1916-1923.
26. Zeradjanin, A. R.; Grote, J.-P.; Polymeros, G.; Mayrhofer, K. J. J., A Critical Review on Hydrogen Evolution Electrocatalysis: Re-exploring the Volcano-relationship. *Electroanalysis* **2016,** *28* (10), 2256-2269.
27. Kuc, A., Low-dimensional transition-metal dichalcogenides. **2014,** *11*, 1-29.
28. Lebègue, S.; Eriksson, O., Electronic structure of two-dimensional crystals from ab initio theory. *Physical Review B* **2009,** *79* (11).

29. Nørskov, J. K.; Abild-Pedersen, F.; Studt, F.; Bligaard, T., Density functional theory in surface chemistry and catalysis. *Proceedings of the National Academy of Sciences* **2011,** *108* (3), 937-943.

CHAPTER 5. IMPROVED HER CATALYSIS THROUGH FACILE, AQUEOUS ELECTROCHEMICAL ACTIVATION OF NANOSCALE WSE_2

Contributions to this project were made by Dr. Olivia Lenz.

5.1. Introduction

Layered transition metal dichalcogenides (TMDCs) have recently been subject to intense research by the scientific community due to the novel properties arising from their layered 2D structure, including corrosion stability, chemically tunable electronic properties, and ability to incorporate guest ions.[1-3] Depending on the crystal structure, TMDCs can be either metallic or semiconducting while remaining stoichiometric. With the increasing need for storage of vast quantities of renewable energy and development of non-carbon containing fuel sources, TMDCs that can catalyze the hydrogen evolution reaction (HER) are of increasing interest to the community. Within this class of materials, MoS_2, WS_2, $MoSe_2$, and WSe_2 have been shown to catalyze the HER with low overpotentials.[4-15] All four TMDCs are promising earth abundant alternatives to Pt metal. Compared to the sulfide-containing TMDCs, WSe_2 has been less explored as a catalyst for the HER.

Each 2D layer of a 3D TMDC is separated by a van der Waals gap, with S, Se, or Te terminating the basal planes. This van der Waals gap reduces the material conductivity, and consequently the HER performance of multilayer TMDCs, because electrons are required to traverse these gaps to move between the individual layers.[16-19] This issue has been addressed in the MoS_2 literature by modulating the final material conductivity through careful attention to synthetic conditions and material structure. The best reported activity of MoS_2 is for trilayer polygons deposited by ultra-high vacuum onto a Au(111) substrate, where the issue of charge transport between layers is a minimal concern.[5, 20] Other researchers have

increased conductivity by utilizing an amorphous structure,[13-14, 21] restricting the crystals to one or a few layers,[16, 20, 22-24] or through intercalation of the van der Waals gap with guest species.[7, 19, 25-29]

Among the champion electrocatalytic systems mentioned above, we note a distinct lack of reports of TMDCs prepared using colloidal synthesis methods. Colloidal synthesis offers many advantages, including scalability, the ability to directly access kinetic phases, and morphological control. However, colloidally prepared TMDCs typically have poor electrocatalytic activity, rendering them of little interest for catalytic applications. In this report, we reveal strategies for post-synthetically overcoming this low activity. We demonstrate that the poor electrocatalytic performance arises from two primary sources: 1) the presence of ligands that block active edge-sites in the as-synthesized colloidal nanocrystals and 2) low conductivity within the 3D TMDC electrode. We address the former through chemical removal of surface ligands and the latter through aqueous electrochemical activation in the presence of cations (protons and alkali metal cations) at low potentials, decreasing the charge transfer resistance. A related electrochemical activation process leading to increased HER kinetics has been associated with intercalation of H^+ in MoS_2.[18-19] Examination of the intercalation chemistry literature pertaining to TMDCs reveals extensive research on intercalating neutral molecules, charged metal ions, and even zero valent metal ions into the van der Waals gap through either physical or electrochemical means.[2, 19, 30-35] Intercalation of metal ions into the van der Waals gap of TMDCs is typically conducted electrochemically or using strong reducing reagents, like alkyl lithium reagents.[36-39] Here we report the facile, aqueous electrochemical activation of colloidally-synthesized TMDC nanocrystals with protons and alkali metal cations without the use of high potentials, organic solvents, or prior treatment with alkyl lithium reagents.

5.2. Results and Discussion

5.2.1. Synthesis and characterization of 2H WSe_2

The WSe_2 nanoflowers (NFs) are synthesized via an air-free hot-injection method. In short, a suspension of selenium in 1-octadecene is injected into a hot mixture of the tungsten carbonyl and trioctylphospine oxide (TOPO). We have confirmed the material composition and structure using powder

X-ray diffraction (XRD), X-ray photoelectron spectroscopy (XPS), transmission electron microscopy (TEM) (Figure 5.1-5.3).

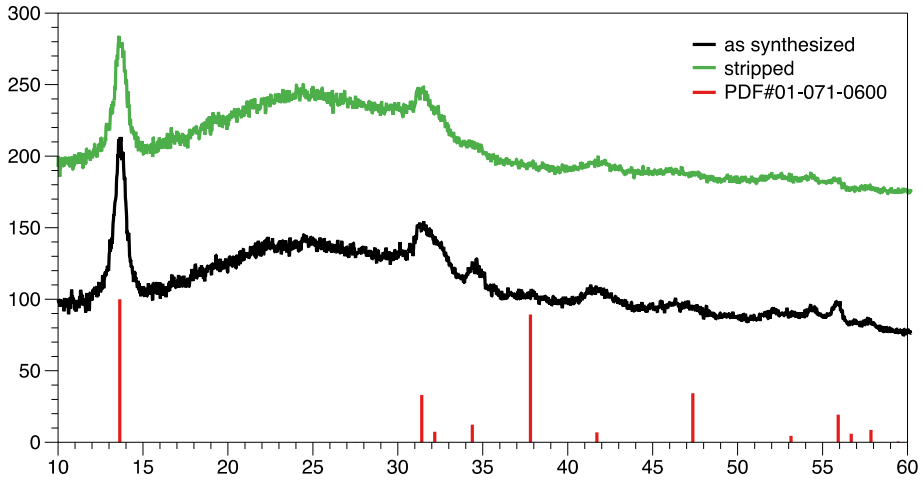

Figure 5.1. XRD spectra of as-synthesized (black) and Meerwein's treated WSe_2 NFs (green). The c-axis spacing of the as synthesized sample was determined to be 12.96 Å via Bragg analysis.

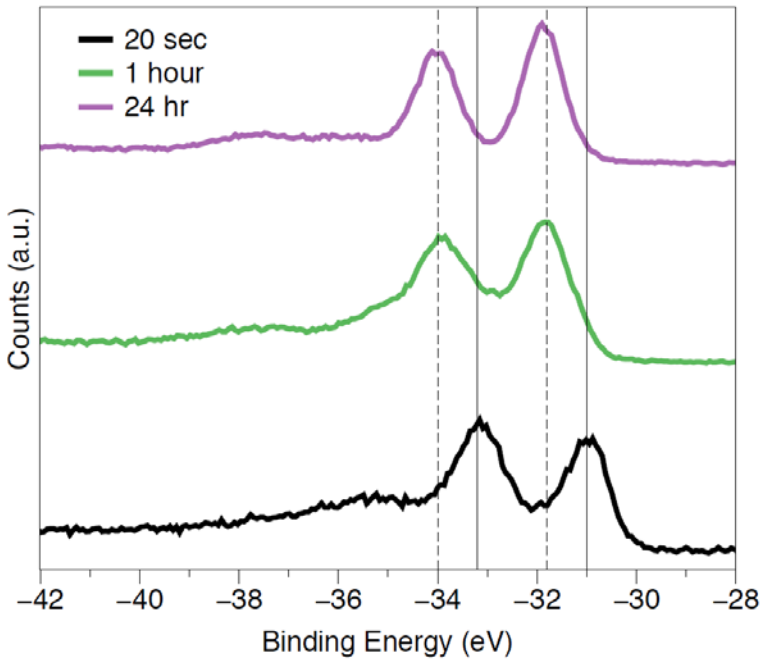

Figure 5.2. XPS data for WSe_2 NFs as a function of synthesis time showing the evolution in polytype from 1T to 2H.

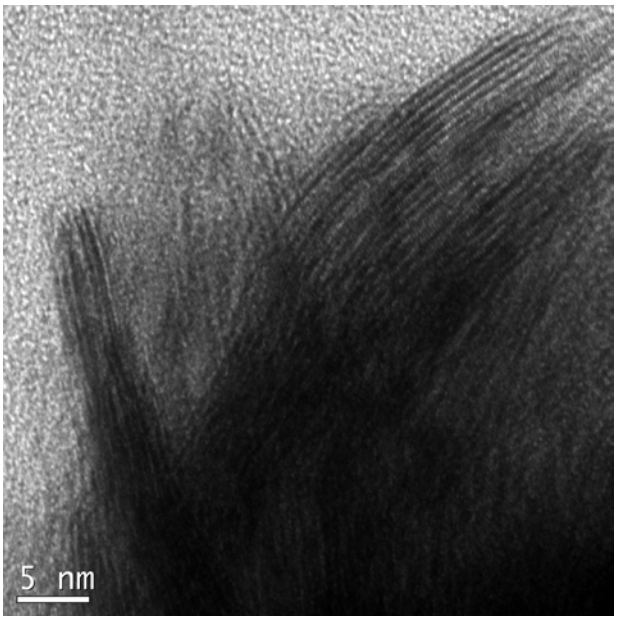

Figure 5.3. TEM image of WSe_2 NFs post-anneal. C-axis lattice spacing is 13.14 +/- 0.73 Å, consistent with that calculated from the XRD data.

Notably, as synthesized, the resulting NFs are not intercalated; this is likely a unique feature of the TOPO-based synthesis since TOPO is sterically too large to fit within the van der Waals gap. While we observe an evolution from the 1T to the 2H polytype as seen in the XPS spectra (Figure 5.2) and a concomitant decrease in HER activity with increased reaction time (Figure 5.4), in the following results we have chosen to use the pure 2H WSe_2 NFs present after a 24-hour reaction time. The WSe_2 NFs are dropcasted from a toluene suspension onto carbon fiber electrodes. This technique results in WSe_2 well dispersed on the electrode.

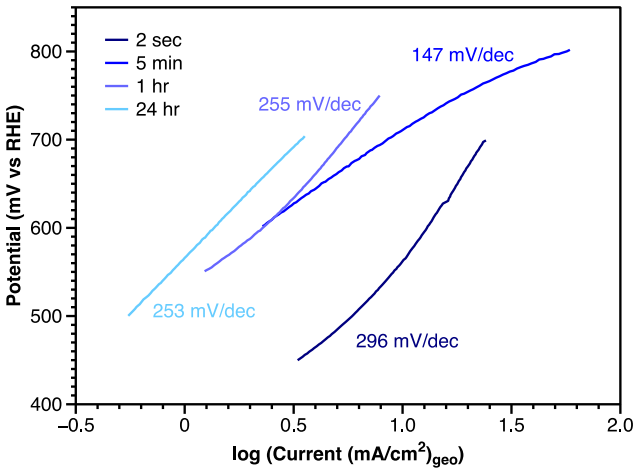

Figure 5.4. Tafel slopes measured for aliquots taken at different reaction times during the growth of WSe_2 NFs.

5.2.2. Meerwein's treatment of WSe_2 electrodes

Carbon fiber electrodes drop-casted with the as-synthesized WSe_2 demonstrate poor catalytic activity for HER, with an overpotential of >600 mV at -10 mA/cm^2 (Figure 5.5). As described in our previous report,[40] the prepared electrodes are treated with a dilute solution of the alkylating agent Meerwein's salt ($[Et_3O][BF_4]$), and we observe an improvement in overpotential by an average of 130mV across 3 syntheses at 10 mA/cm^2 (Figure 5.5). We attribute the variation in overpotential reduction between syntheses to varying ligand coverage after synthetic work-up. The change in overpotential is due to removal of edge- or defect-site bound TOPO ligands remaining from the NF synthesis, as evidenced by FTIR data demonstrating the removal of surface TOPO ligands (Figure 5.6).[40] We believe the edge- or defect-site bound ligands on the WSe_2 NFs are exclusively trioctylphosphine oxide due the purity of the starting reagent confirmed by ^{31}P and ^{1}H NMR spectroscopy (See Experimental Figure 5.22). Phosphine oxides are suitable ligands for late transition metals such as tungsten.[41-43] Furthermore, reaction between a 1:1 mixture of Meerwein's reagent and TOPO shows clean formation of ethoxytrioctylphosphonium tetrafluoroborate (See Experimental Figure 5.23), which is non-interacting with the WSe_2 surface.[44] Notably, characterization of the as synthesized and Meerwein's treated NFs by SEM reveals no change in morphology (Figure 5.7) and XPS shows no change in polytype (Figure 5.8).

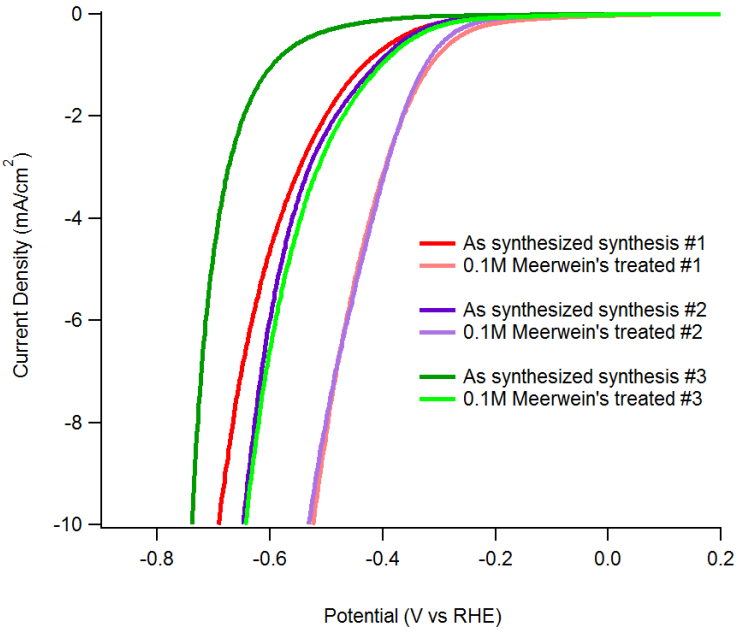

Figure 5.5. Linear sweep voltammograms of as-synthesized and Meerwein's treated (30 s) WSe_2 NF electrodes across three synthetic batches.

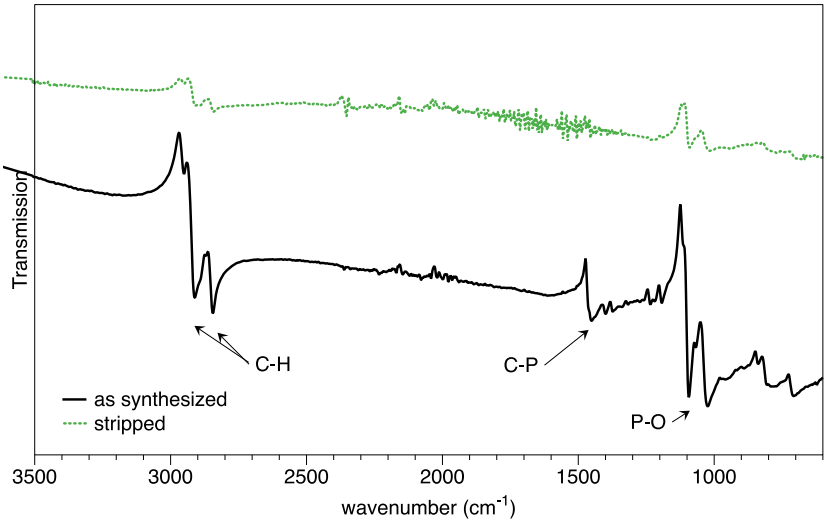

Figure 5.6. FTIR spectra of WSe_2 NFs as synthesized and after treatment with Meerwein's reagent, showing a significant decrease in the ligand density in the sample.

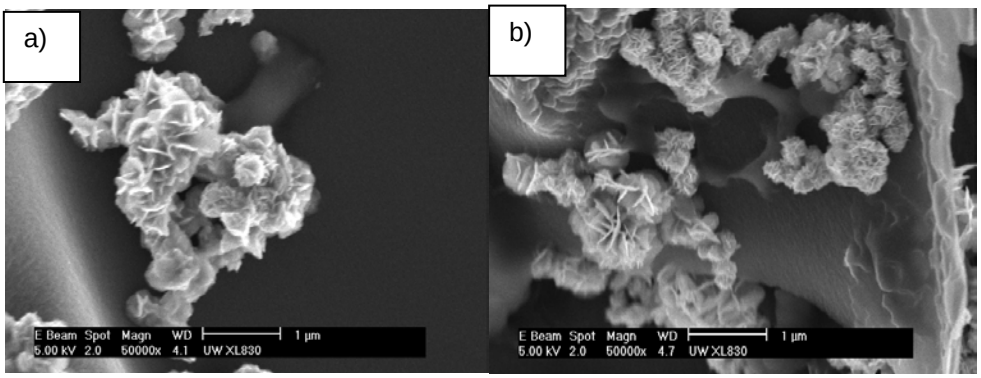

Figure 5.7. SEM images of WSe_2 NFs (a) before and (b) after Meerwein's treatment.

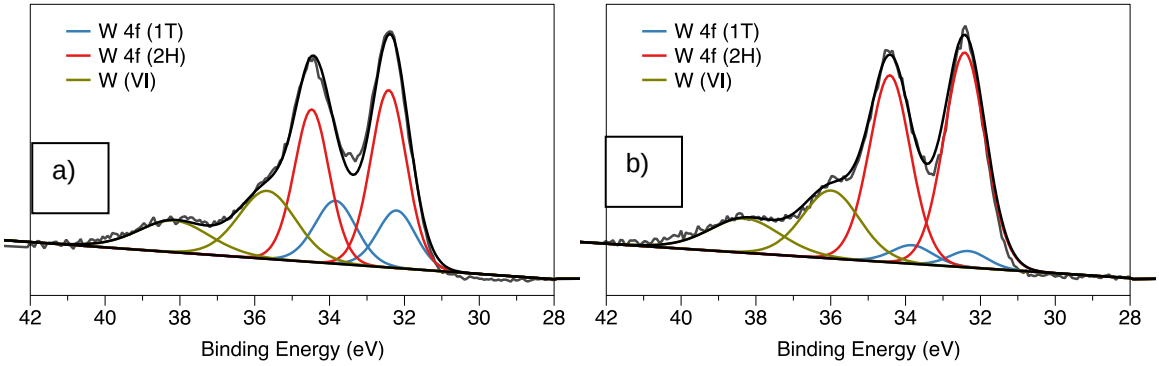

Figure 5.8. XPS data showing the 4f W binding energy for as synthesized (a) and Meerwein's treated (b) WSe_2 NFs.

5.2.3. Electrochemical activation of WSe_2 electrodes

While executing a standard electrolysis stability test of as-synthesized NFs, we observed a drastic decrease in overpotential with time. Extended electrolysis of the Meerwein's treated WSe_2 NF electrodes at -10 mA/cm^2 for 16 hours in 0.5 M H_2SO_4 lead to a decrease in overpotential of approximately 270mV (Figure 5.9). The Tafel slope also changes upon electrolysis, decreasing from 191 mV/dec to 116 mV/dec (Figure 5.10), indicating improved HER kinetics. We note that electrolysis with both graphite and Pt as the auxiliary electrode leads to improvements in overpotential. However, utilizing Pt has a more substantial

impact on the final change in overpotential upon both electrolysis and treatment with Meerwein's reagent, suggesting that Pt leaching from the counter electrode does occur under these conditions.

To explain the improvement in electrocatalytic performance after electrolysis, we first considered an increase in electrochemically active surface area and calculated the double layer capacitance (C_{DL}) of the electrode after each hour of electrolysis. Prior to electrolysis, application of Meerwein's reagent to an electrode deposited with as synthesized WSe_2 results in an increase in surface area by 11x (Figure 5.11). This result was expected as the Meerwein's reagent removes ligands from catalytically active edge sites. Additionally, we observe an increase in surface area of ~4x after electrolysis at -10mA/cm^2 at 16 hours, however this does not fully account for the decrease in overpotential observed.

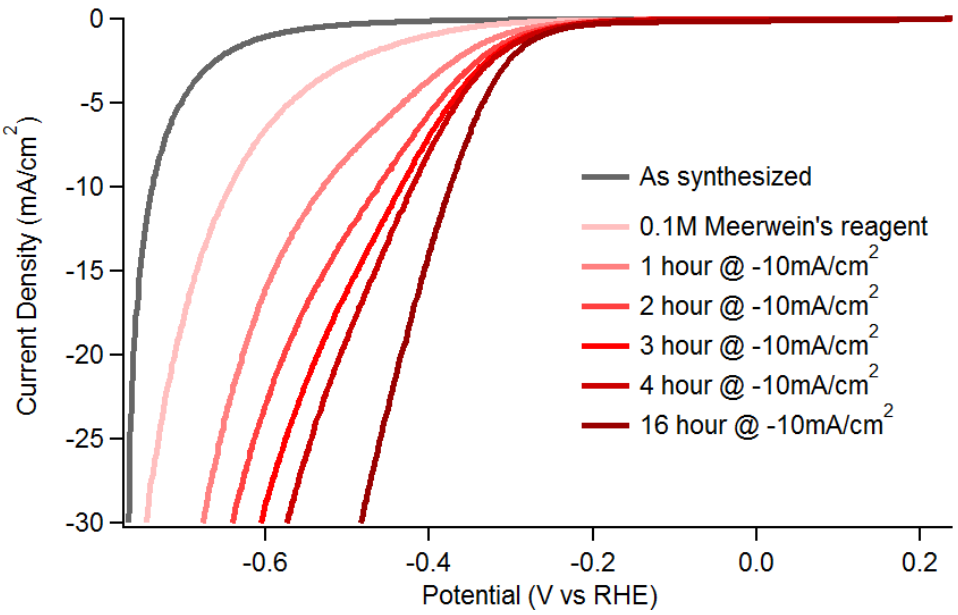

Figure 5.9. Linear sweep voltammograms of WSe_2 NF deposited on carbon fiber electrodes as synthesized, after Meerwein's treatment and after galvanostatic electrolysis at -10 mA/cm^2 in 0.5 M H_2SO_4.

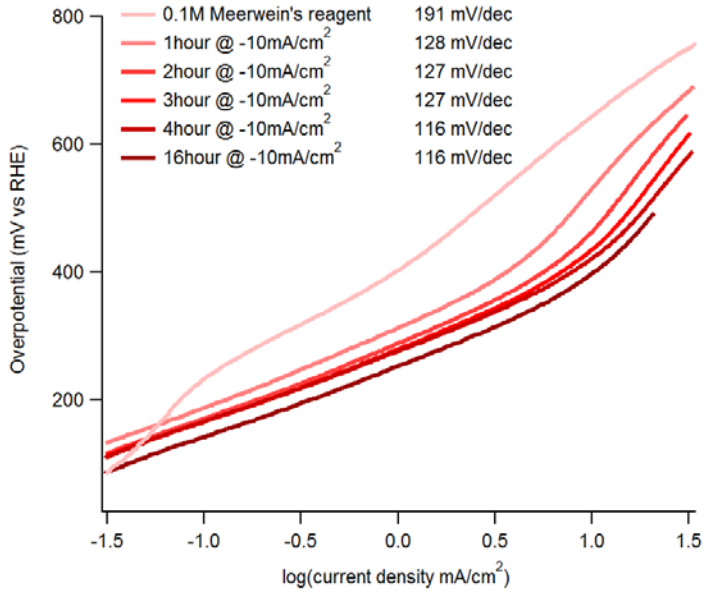

Figure 5.10. Data extracted from Figure 5.9 to determine Tafel slopes. The black regions indicate the portions of the LSVs used for the linear fit with Tafel slopes listed in the legend.

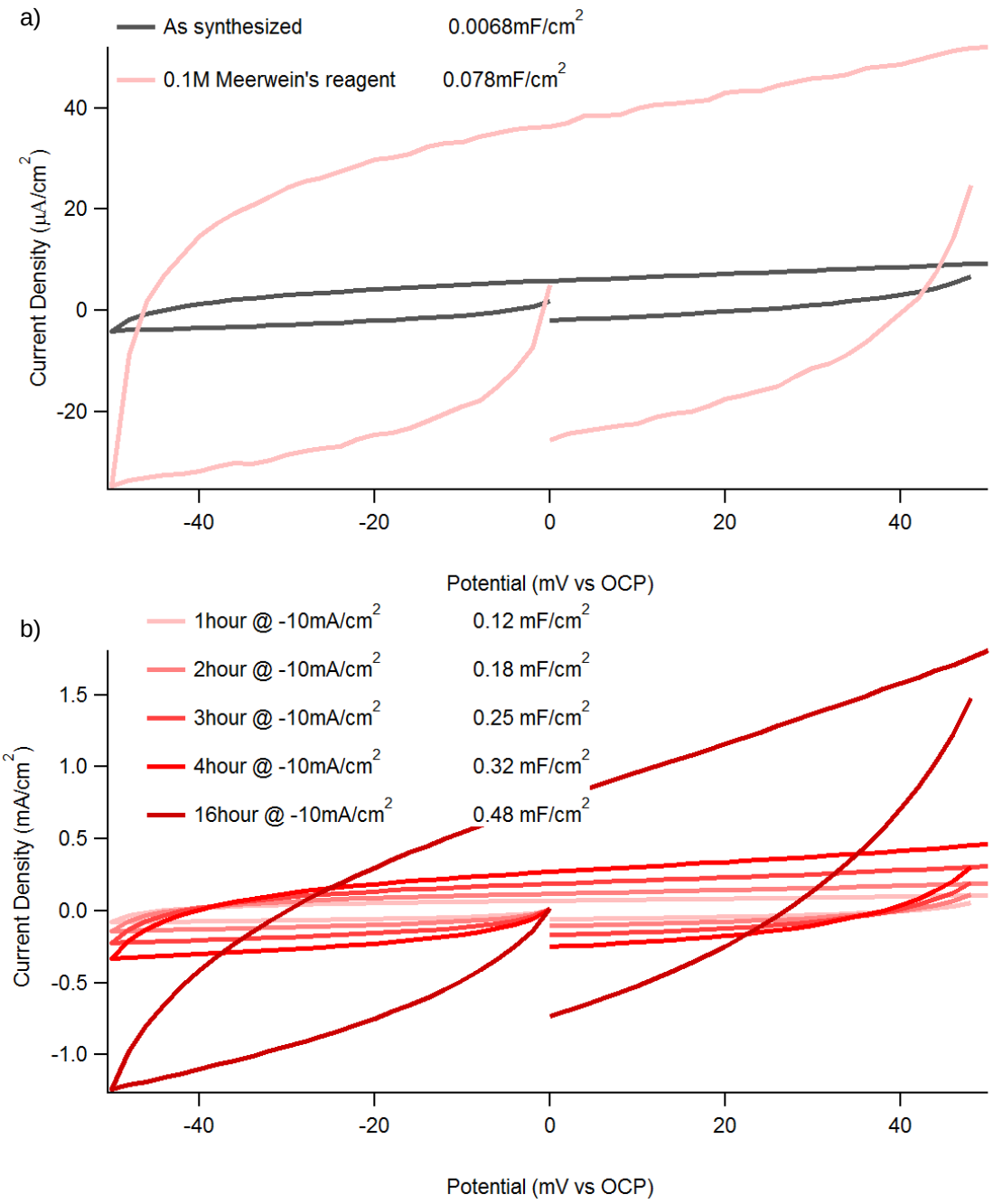

Figure 5.11. Cyclic voltammograms (500 mV/s) of WSe_2 NF electrode a) treatment with Meerwein's reagent and b) after electrolysis and . For each condition a scan rate dependence study was carried out using 50, 100, , 500,1,000 and 2,000 mV/s, leading to the C_{DL} values given in the legend.

To explain the increase in catalytic activity after electrolysis in H_2SO_4, we hypothesized that the material was incorporating H^+ under a reducing bias (Scheme 5.1). Incorporation of H^+ and e^- via intercalation into the van der Waals gap of TMDCs has been previously observed and described in the literature.[19, 45-47] To explore this electrochemical activation process, we subjected WSe_2 NF deposited electrodes to electrolysis conditions in alkali metal electrolytes. A reductive event is identified by a pre-feature in the linear sweep voltammograms (LSV) (Figure 5.12) and we observed that the potential of the pre-feature correlates with the standard reduction potential (E^o) of the alkali metal cation.[36] Since the standard reduction potentials also correlate with the hydration energies of the metal cations, it is possible that hydration plays a direct role in the activation chemistry. Additionally, we found that this reduction event is both complete and irreversible after the initial potential sweep (Figure 5.13), as sweeping the potential in the reverse direction did not exhibit an anodic peak nor did the cathodic peak reappear in consecutive forward potential sweeps

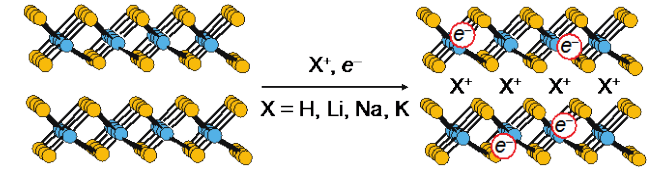

Scheme 5.1. Proposed electrochemical activation of WSe_2 with H^+ and alkali metal cations.

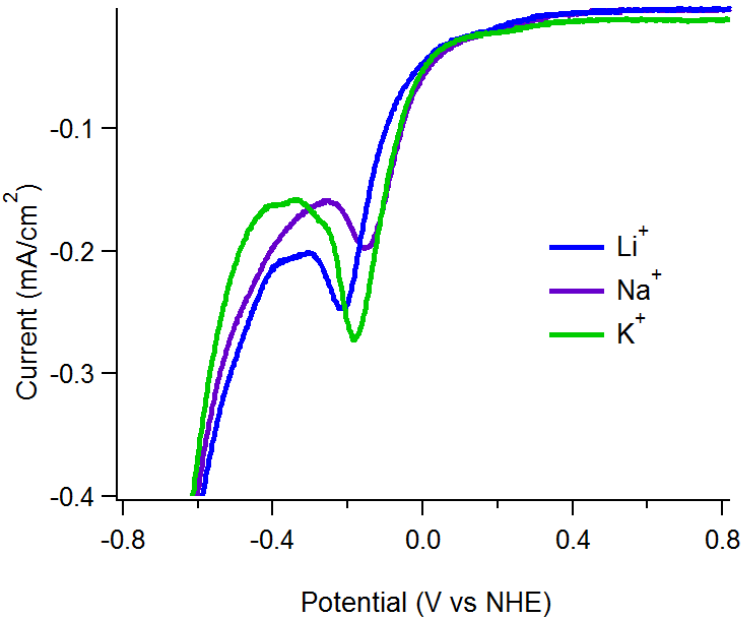

Figure 5.12. LSVs of WSe_2 NFs on titanium electrodes in 0.5 M Li_2SO_4, Na_2SO_4 and K_2SO_4 electrolyte.

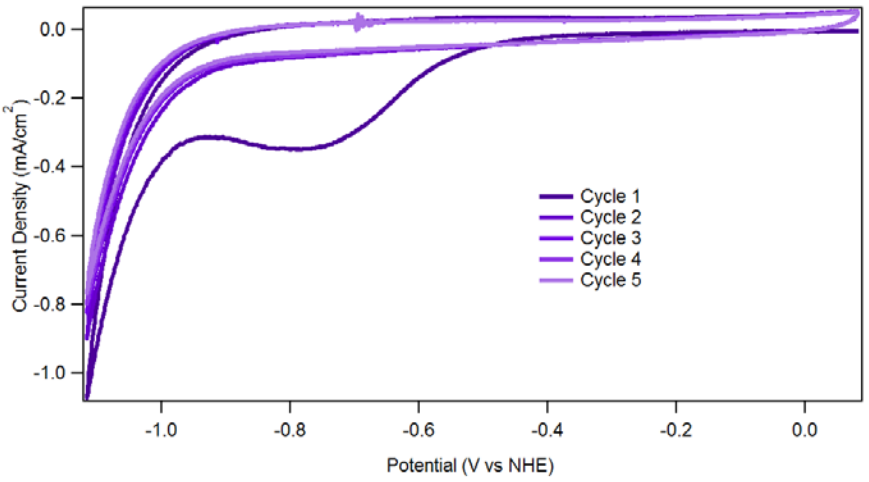

Figure 5.13. CVs of WSe_2 NF electrodes during and after electrochemical activation with Na^+ in 0.5M Na_2SO_4. No peak is evident after the first cycle at 5mV/s showing that the electrochemical activation process is complete and irreversible after the first cycle.

Irreversible intercalation events have been suggested to be a result of material reconstruction post-intercalation, evident especially in smaller particles.[48] We postulate that this electrochemical activation process is a defect-driven intercalation event that is thermodynamically driven.

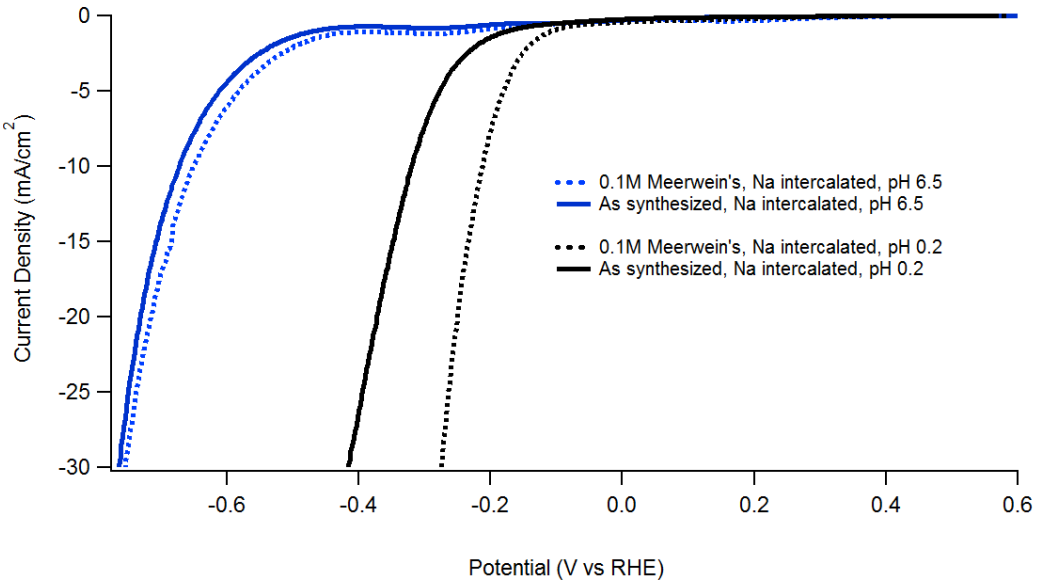

Figure 5.14. Treatment of WSe_2 electrodes that have been electrochemically activated by Na^+ before and after treatment with Meerwein's reagent in 0.5 M Na2SO4 (blue) and 0.5 M H_2SO_4 (black).

We also note that cation incorporation is successful before or after ligand stripping with Meerwein's reagent (Figure 5.14). Post-alkali cation activation, HER catalyzed by the WSe_2 NFs occurs at reduced overpotentials, in the range of 243-284 mV @ -10mA/cm^2 (Figure 5.15).

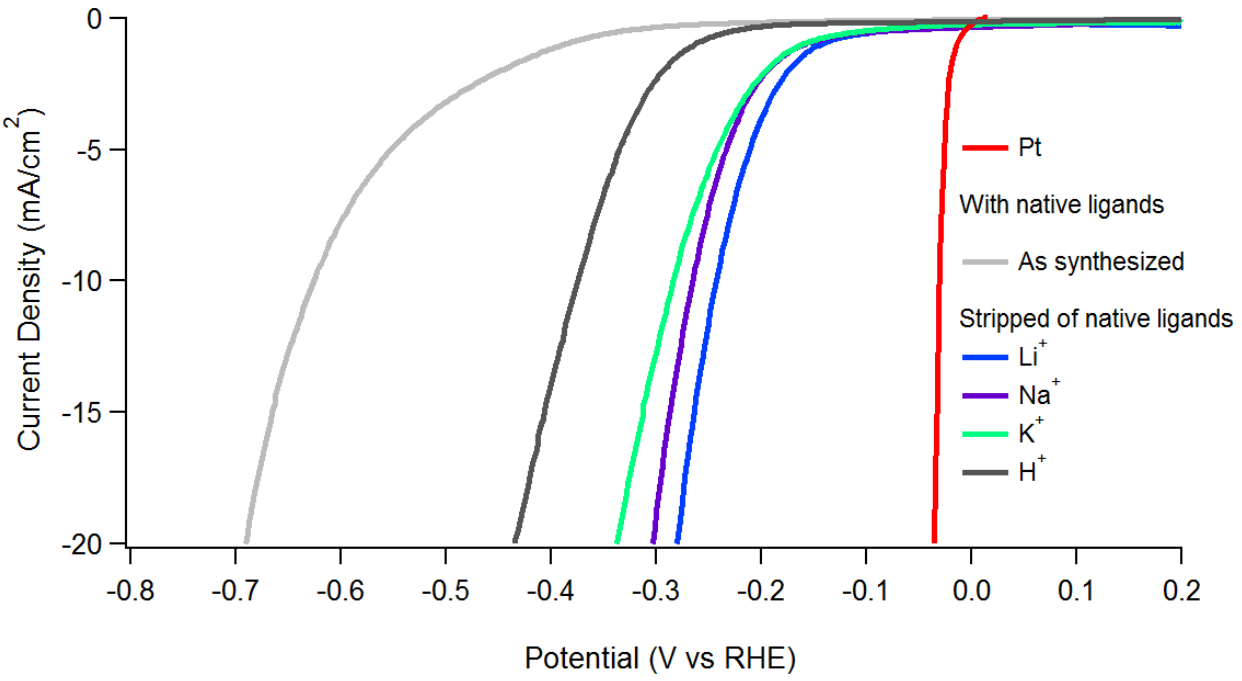

Figure 5.15. LSVs of WSe_2 NFs on carbon fiber electrodes in 0.5M H_2SO_4 before and after intercalation and treatment with $[Et_3O][BF_4]$.

5.2.4. Characterization of electrochemically activated WSe_2 electrodes

In order to investigate any structural changes to the WSe_2 after electrochemical activation and to explore the possibility for a traditional intercalation mechanism, we employed XRD, XPS, Raman, HRTEM and SEM. Interestingly, there is not an appreciable shift of the (002) peak in the XRD pattern, corresponding to the interlayer spacing in the WSe_2, after electrochemical activation (Figure 5.16).[49-51] Two possible explanations for the lack of a shift in the (002) peak if the electrochemical activation is interpreted as an intercalation process are: 1) the extent of intercalation under these conditions is low, and likely mediated by defects in our nanostructured material, or 2) the ions are intercalating without attached water molecules. This is consistent with observations of vapor phase intercalation with no change in (002) spacing until after exposure to ambient air resulting in co-intercalation of water molecules.[52-53] A shift in the XRD peaks is not observed even after extended electrolysis at the Na^+ intercalation potential for 20 min. Raman spectroscopy was also carried out to identify structural changes that may arise upon intercalation, as a change in peak

intensities and/or location with intercalation has been previously demonstrated in TMDCs.[50] However, WSe_2 has overlapping E_{1g} and A_{1g} peaks that obscure any minor changes in peak location or intensity, making this analysis inconclusive. Thus, we sought confirmation of cation intercalation through analysis of the ion binding energies using X-ray photoelectron spectroscopy (XPS). This analysis was restricted to the Na-intercalated sample since the K peaks overlap with the Se Auger peak and the Li peak is not able to be resolved with our instrument. When a WSe_2 NF deposited electrode dipped in a solution of 0.5 M Na_2SO_4, where we assume any Na^+ is just absorbed on to the surface of the material, is compared to one that has been electrochemically activated, we observe a significant shift in the Na 2*s* binding energy to higher energies (Figure 5.16B, left). A shift to higher binding energies implies that electrons require more energy to be removed, which is expected upon intercalation and is consistent with previous observations of Na-intercalated TMDCs in the literature.[54] From XPS analysis of the W 4*f* region (Figure 3B, right), we see no evidence of a change in polytype from 2H to 1T upon intercalation, as has been described in a number of publications.[34, 49-50, 55-56] In addition, HRTEM images of the as synthesized and Na^+ activated WSe_2 NFs show no observable change in interlayer spacing (Figure 5.17).

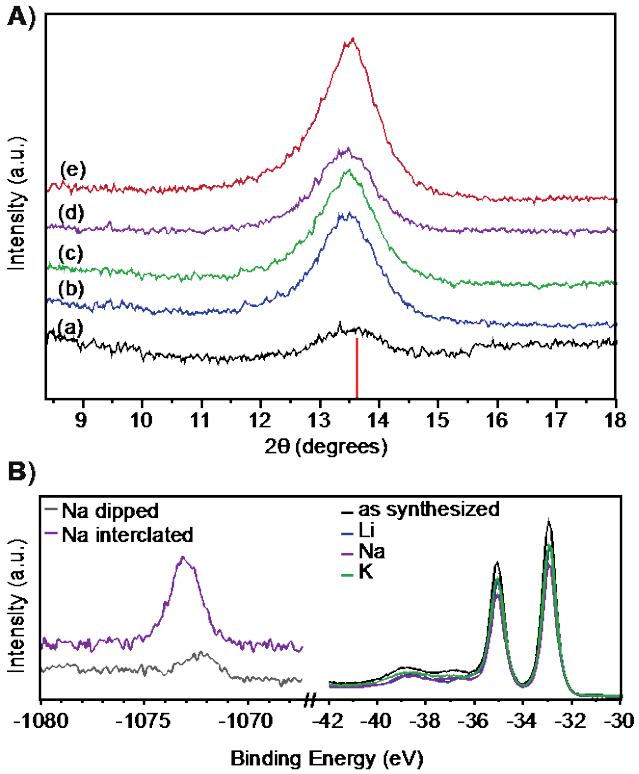

Figure 5.16. A) Close up view of the (002) peak in the XRD of (a) as synthesized, (b) Li^+, (c) K^+, and (d) Na^+ intercalated WSe_2 NFs. Spectrum (e) was observed after the extended Na^+ intercalation time. The bar on the x-axis is the expected (002) peak location for a bulk WSe_2 sample (PDF #00-038-1388). B) Na 2*s* XPS analysis of WSe_2 NFs dipped into a solution of $NaSO_4$ (gray) versus electrolyzed in a solution of $NaSO_4$ (purple); and W 4*f* XPS data for the as-synthesized and intercalated WSe_2 NFs.

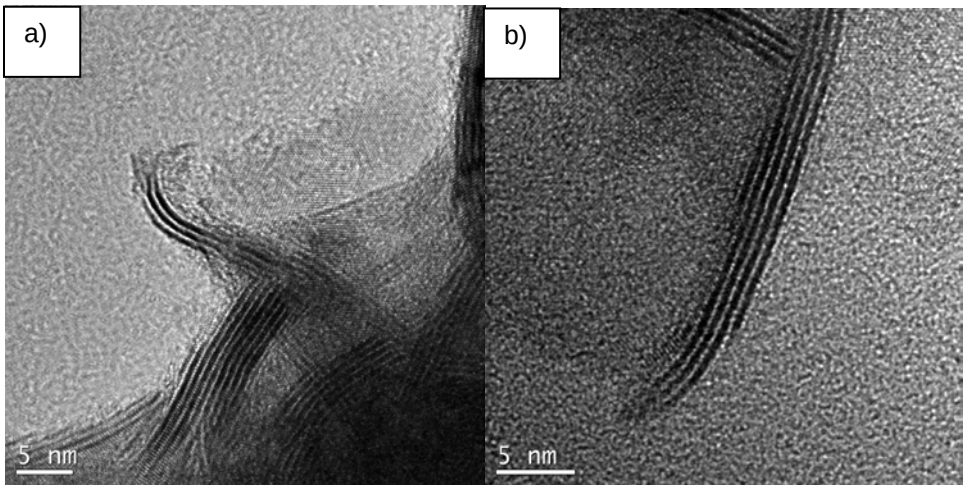

Figure 5.17. HRTEM of a) as-synthesized and b) Na^+-activated WSe_2 NFs.

Since there is no measurable change in polytype, we hypothesize the improved catalytic performance upon electrochemical activation arises via two other mechanisms: 1) modulation of the catalyst surface work function, and 2) improved electron transport between layers in the WSe_2 nanoflowers. We observe experimentally that the cations involved in the electrochemical activation process modulate the work function of the catalyst, a metric that has been correlated with the exchange current density and by association the M-H bond strength in the metal catalyst HER literature.[57,58] Ultraviolet photoelectron spectroscopy (UPS) analysis of each sample results in a linear correlation between the work function (WF) and overpotential for this series (Figure 5.18). We also note a linear relationship between WF and ionization energy of the cation, suggesting a potential opportunity for further system optimization. In this series, the more electronegative the incorporated cation, the lower the Fermi level, or the larger the work function, the more active the material is for HER. Theoretical work on the active sites of WSe_2 suggests the active site is the Se^{2-} edge and that this site binds hydrogen more tightly than what is ideal.[59] As we observe a decrease in overpotential after alkali ion incorporation, we infer that the resulting change in electronic structure leads to more thermoneutral Se-H bonding when compared to non-intercalated WSe_2. Additionally, this view of Se-H bond strength influenced by the electronegativity of the intercalate explains the $Li^+ < Na^+ < K^+$ overpotential trend in our data.

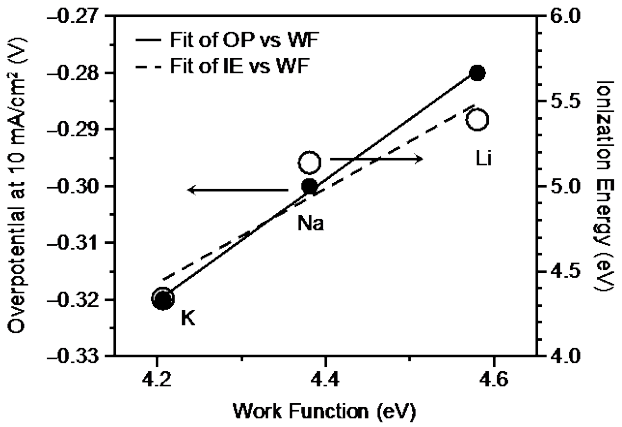

Figure 5.18. Plot of K^+, Na^+, and Li^+-intercalated WSe_2 NF deposited electrode overpotential (left axis) and alkali metal ionization energy (right axis) against the work function measured by UPS.

Not only is the catalyst work function modulated upon electrochemical activation, but the charge transfer resistance is also greatly reduced. It has been shown experimentally that electron hopping between layers of TMDCs greatly limits the HER activity of the catalyst, and we hypothesized that this electrochemical activation may be a viable strategy to increase the electron hopping rate.[60] Electrochemical impedance spectroscopy (EIS) was used to test this hypothesis through measuring the charge transfer resistance of the material, however, because the reductive prefeature occurs at a potential that coincides with hydrogen evolution, we required an alternate method for evaluating charge transfer resistance (R_{CT}) in the activated and non-activated samples. We determined that using a redox probe with a characteristic redox couple more oxidative than the reductive event, such as $[Fe(CN)_6]^{3-/4-}$ with an $E_{1/2}$ at 0.361 V vs NHE, would allow us to focus on the electron transfer event itself.[61] The EIS data is fit to an equivalent circuit (Figure 5.19, Table 5.1-5.2) and the resulting Nyquist plots (Figure 5.20) reveal that the R_{CT} decreases from 1440 ohms to 9.5 ohms after electrochemical activation. There is an inverse relationship between R_{CT} and heterogeneous electron transfer rate (k^0, see Experimental for derivation). We calculate an increase in k^0 from 1.5×10^{-3} to 9.4×10^{-2} cm/s for the $[Fe(CN)_6]^{3-/4-}$ couple upon intercalation.[62] This change in electron transfer rate by nearly two orders of magnitude suggests a significant improvement in lowering the charge transfer resistance of the material. This likely arises from improvement in both interlayer charge transfer and intralayer conductivity upon electrochemical activation. The proposed improvement in the intralayer

conductivity is likely due to the reduction of a W d-orbital based band allowing charge movement in the conduction band of the material (Scheme 5.2).[63-64]

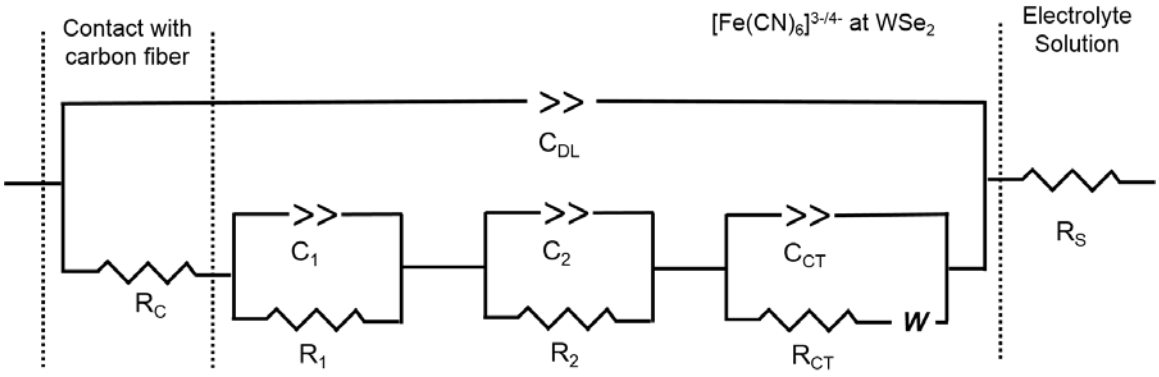

Figure 5.19. Equivalent circuit used to fit impedance data.

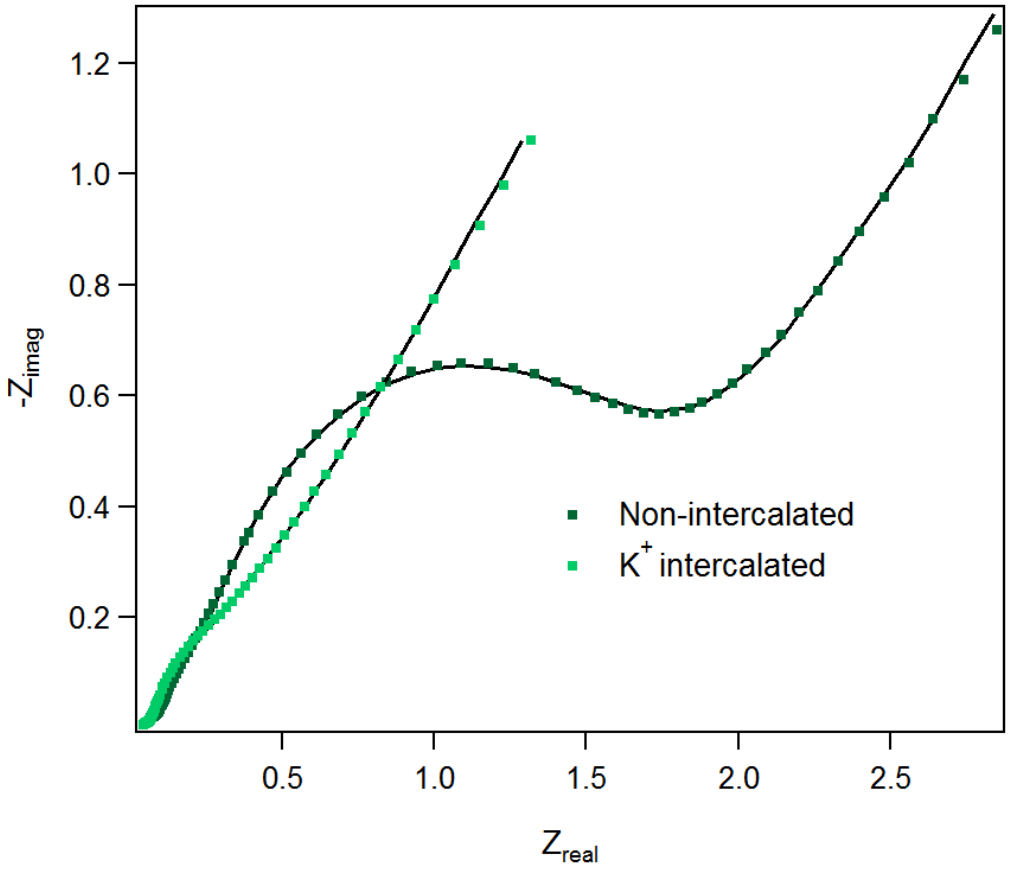

Figure 5.20. Nyquist plots for non-intercalated and K^+ intercalated WSe_2 NF deposited electrodes in the presence of 3 mM $[Fe(CN)_6]^{3-/4-}$ in 0.5 M K_2SO_4.

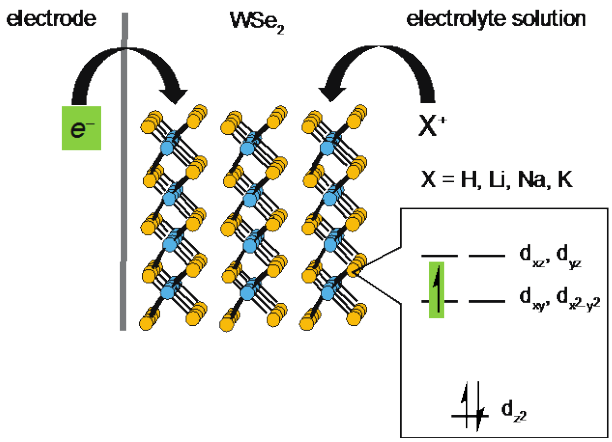

Scheme 5.2. Proposed scheme of electrochemical activation event whereby electrons and cations are incorporated, and the reduction of the W d-orbital based band leads to a decrease in charge transfer resistance.

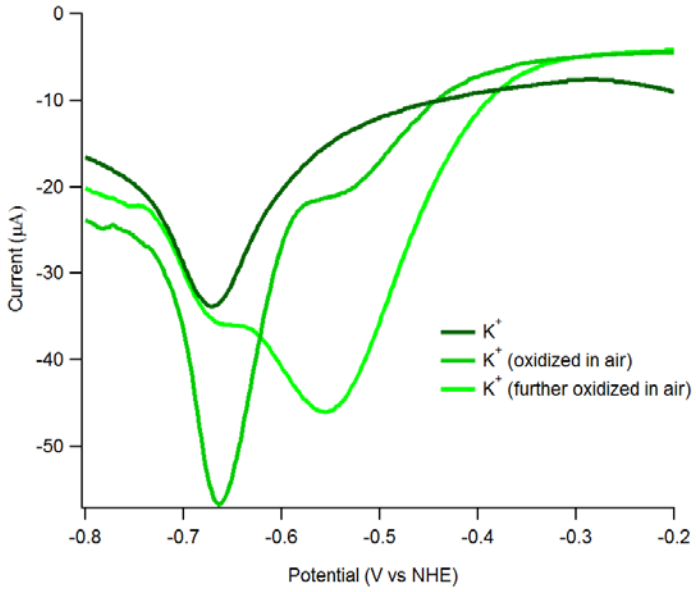

Figure 5.21. Linear sweep voltammetry of WSe_2 NF electrodes that have been exposed to air, showing evidence for a new reduction event associated with the oxidized material.

In order to eliminate the possibility of oxide formation contributing to the above observations, the WSe_2 electrodes were allowed to sit in air for hours and then electrochemically activated. A new reduction

peak appearing at a more oxidative potential in the LSVs, which we associate with oxide formation was revealed (Figure 5.21).

Finally, in order to benchmark the WSe_2 NFs among other WSe_2 electrodes reported in the literature, we divided the exchange current density (j_0/cm_{geo}^2) values by the electrochemically active surface area (ECSA) for the Meerwein's treated, Na^+ activated electrode. This value of $1.2x10^{-2}$ j_0/ECSA (mA/mF), is notably larger than that reported by Zou et. al. at $5.6x10^{-4}$ j_0/ECSA (mA/mF).[65] We attribute this to the larger number of active sites per surface area for the colloidally synthesized WSe_2 NFs reported here. In addition, extended electrolysis of the WSe_2 NFs activated by H^+ show stability beyond 12 hours (Figure 5.9).

5.3 Conclusion

In summary, we have observed facile, aqueous electrochemical activation of colloidally-synthesized nanoscale WSe_2 by H^+, Li^+, Na^+ and K^+ ions. This process occurs at potentials either coincident with or more positive than HER, which is unique to this nanoscale system and differs significantly from traditional electrochemically-driven intercalation processes observed in the bulk.[38] Electrochemical activation does not lead to any measurable change in the 2H polytype of the material or in the interlayer spacing. Ultimately, using electrochemical activation in conjunction with removal of the edge-bound ligands derived from the colloidal synthesis using a mild alkylating agent, we were able to increase the HER kinetics of colloidal WSe_2, leading to a > 400mV improvement in overpotential, with our champion electrode giving an overpotential of 243 mV at -10mA/cm^2. We attribute the dramatic effect of electrochemical activation to decreased charge transfer resistance, as well as to perturbation of the material work function. Because we are able to render the 2H, semiconducting polytype of WSe_2 highly active for HER we are excited about the prospects of this material for photoelectrocatalytic applications, and see potential for development of this and related systems for aqueous alkali metal battery cathodes.[66]

5.4 Experimental

5.4.1. General considerations and synthesis of 2H WSe_2

Materials: Trioctylphosphine Oxide (TOPO) (Aldrich, 99%) was recrystallized three times from CH_3CN. Tungsten hexacarbonyl (Aldrich, 99.99%), 1-octadecene (ODE, Aldrich, 90%), selenium powder (Aldrich, 100 mesh), Li_2SO_4 (Aldrich, 99.9%), K_2SO_4 (Aldrich, 99%), Na_2SO_4 (Aldrich, 99%), $K_3[Fe(CN)_6]$ (Aldrich, 99%), $K_4[Fe(CN)_6]$ (Aldrich, 99%), H_2SO_4 (99.999%), and triethyloxonium tetrafluoroborate (Aldrich, ≥97%) were used as-received.

Characterization Methods: Powder XRD data were collected on a Bruker D8 Discover with GADDS XRD system, with Cu Kα radiation. SEM and EDS data were collected on a FEI XL830 microscope. XPS data were collected on a Kratos AXIS Ultra spectrometer. Raman data were collected on a Reinshaw InVia instrument equipped with a 516 nm laser and used at low power to avoid damaging the sample.

All electrochemical measurements were conducted in a custom four-neck cell fitted with either a platinum coil or a graphite rod auxiliary electrode separated in a fritted compartment, a $Ag/AgSO_4$ reference electrode separated by a Vycor frit and a working electrode at 5mV/s unless otherwise noted. The working electrodes used in this study were fabricated from carbon paper (Fuel Cell Store, Spectracarb 2050A 0850). The carbon fiber electrodes were made by cutting a 1 cm x 3 cm rectangle and attaching a copper wire with silver epoxy to the electrode material. The copper wire/silver epoxy was then covered with gel epoxy to create a 1 cm x 1 cm surface area. (Note: the backside of the electrode was not covered due to its porosity with epoxy leaking onto both sides.) Titanium electrodes (Ti foil, 99.7%, Aldrich) were fabricated similarly.

All voltammograms depicting proton reduction were performed after sparging the cell with argon or nitrogen gas. The electrolyte solution is typically 0.5 M H_2SO_4 in 18 megaohm Millipore water unless otherwise noted. The figure of merit of overpotential at -10 mA/cm^2 was found from the voltammograms using the geometric surface area of the electrode. All measurements in this study were referenced to RHE, which was measured using a platinum coil electrode in H_2 saturated 0.5 M H_2SO_4.

EIS measurements were taken on WSe_2 NFs deposited on glassy carbon electrodes (BASi, 3.0mm dia) with the following parameters: DC voltage = open circuit voltage, AC voltage (mV rms) = 3.53, initial frequency= 50000 Hz, final frequency= 0.1 Hz, points per decade= 14.

All LSVs contained in the same plot are either the same electrode, or have the same loading if different electrodes were used.

Synthesis of WSe_2 NFs: In a method adapted from Yu *et al.* for the synthesis of MoS_2 nanocrystals, 10 g of TOPO and 0.14 g (0.4 mmol) of $W(CO)_6$ were stirred under argon at 250 °C using standard Schlenk line techniques.[67] After 24 hours, the reaction temperature was raised to 320 °C. A separate solution of 8.5 mg/mL of Se powder in ODE was sonicated at room temperature, following a procedure outlined by Pu *et al.*, and 5 mL were immediately injected into the hot W-TOPO solution.[68] We note that a small amount of the Se adheres to the vial and so the actual amount injected is slightly less than 8.5 mg/mL. After stirring at 320 °C for a specified reaction time (typically 24 h to obtain pure 2H phase material), the solution was cooled to 60 °C. To this cooled solution 8 mL of toluene were injected, followed by 8 mL of methanol. The solution was centrifuged, decanted, and the remaining precipitate washed with toluene and methanol twice more.

5.4.2. NMRs of trioctylphosphine oxide and reaction of trioctylphosphine with Meerwein's reagent

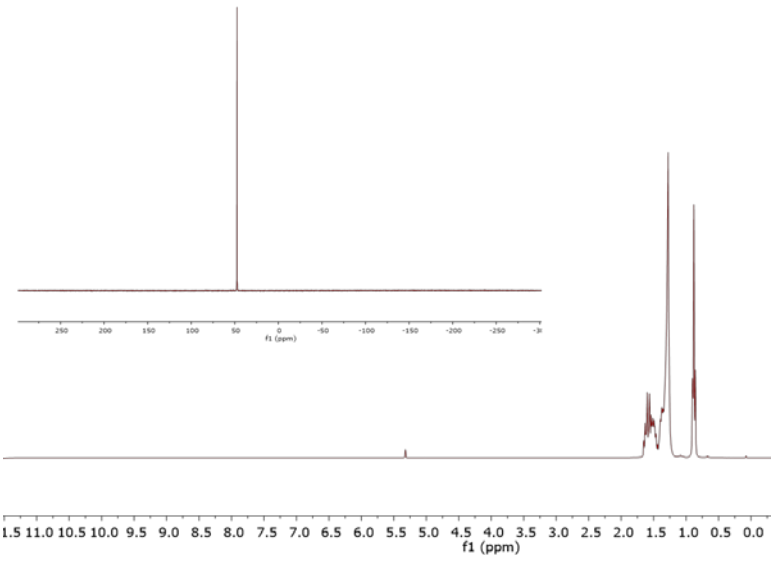

Figure 5.22. ^{1}H and ^{31}P (inset) NMR spectra of 3x recrystallized trioctylphosphine oxide in CD_2Cl_2.

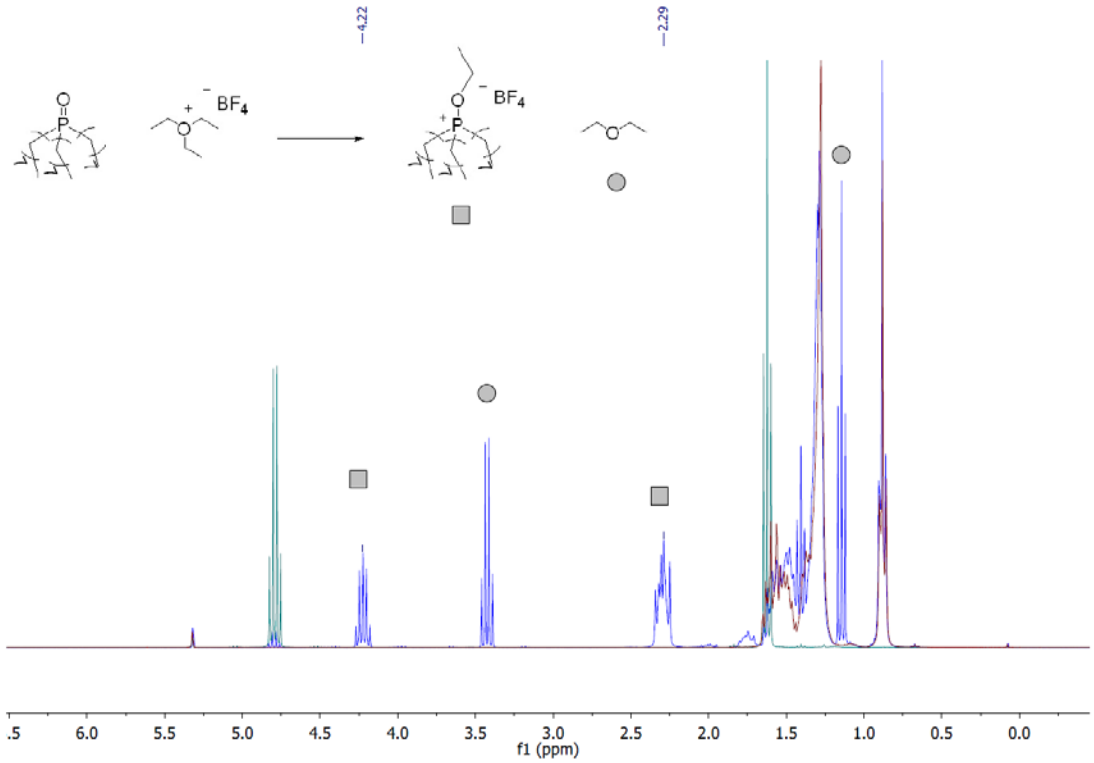

Figure 5.23. ^{1}H NMR spectra of Meerwein's reagent (green), trioctylphosphine oxide (maroon), and the products of the reaction between Meerwein's reagent and trioctylphosphine oxide (blue). Data for the phosphonium salt: ^{1}H NMR (300 MHz, CD_2Cl_2) δ 4.22 (p, *J* = 6.9 Hz, 2H), 2.43 – 2.16 (m, 6H), 1.41 (td, *J* = 6.9, 0.9 Hz, 3H), 1.67 – 1.20 (m, 46H), 0.99 – 0.75 (m, 11H). ^{31}P NMR (202 MHz, CD_2Cl_2) δ 99.92.

5.4.3. Fit data and errors for EIS

Table 5.1. Fit data and errors for impedance data presented for WSe_2 electrodes that have been electrochemically activated by K^+.

Element	**Value**	**+/- error**
RCT	9.448	201.9 ohm
Rs	41.53	30.45 ohm

CDL	1.014e-6	95.89e-6 S*s^a
a	906.4e-3	7.328
CCT	5.164e-6	287.2e-6 S*s^a
a	859.3e-3	5.353
W	858.1e-6	105.0e-6 S*s^(1/2)
C2	1.539e-3	2.319e-3 S*s^a
a	888.6e-3	942.8e-3
R2	88.00	274.1 ohm
R1	97.06	154.1 ohm
Rc	10.90	219.7 ohm
C1	135.0e-6	189.5e-6 S*s^a
a	992.1e-3	220.1e-3
Goodness of fit	50.71e-6	

Table 5.2. Fit data and errors for impedance data presented for as-synthesized WSe_2 electrodes.

Element	**Value**	**+/- error**
RCT	1.441e3	178.0 ohm
Rs	54.30	29.34 ohm
CDL	390.7e-9	6.878e-6 S*s^a
a	895.0e-3	1.453
CCT	17.31e-6	7.218e-6S*s^a

a	857.4e-3	60.87e-3
W	728.2e-6	32.27e-6 S*s^(1/2)
C2	8.479e-6	15.68e-6S*s^a
a	930.4e-3	593.0e-3
R2	109.8	327.5 ohm
R1	38.37	288.5 ohm
Rc	41.76	134.2 ohm
C1	17.77e-6	265.1e-6 S*s^a
a	765.7e-3	1.851
Goodness of fit	28.25e-6	

5.4.4. Calculation of heterogeneous rate constant from EIS Data

The resistance of charge transfer, R_{CT} is inversely proportional to the exchange current density, i_0

$$R_{CT} = \frac{RT}{nFi_0}$$

The heterogeneous rate constant, k^0, is related to the exchange current density and the following expression is true if the concentrations of the oxidized and reduced species are the same (C_R=C_O), which follows in our case as DC voltage of the EIS measurement is at the $E_{1/2}$ of the $Fe^{2+/3+}$ couple.[69]

$$k^0 = \frac{i_0}{nFAC}$$

Leading to the following expression,

$$k^0 = \frac{RT}{n^2F^2ACR_{CT}}$$

The area of the electrodes were calculated from the Randles-Sevcik equation, calculating for A, using 0.74×10^{-5} cm^2/s for the diffusion coefficient.[70] Areas calculated were $0.02cm^2$ for the non-intercalated and $0.05cm^2$ for the K^+-intercalated electrodes.

5.4 References

1. Benavente, E.; Santa Ana, M. A.; Mendizábal, F.; González, G., Intercalation chemistry of molybdenum disulfide. *Coordination Chemistry Reviews* **2002,** *224* (1), 87-109.
2. Jung, Y.; Zhou, Y.; Cha, J. J., Intercalation in two-dimensional transition metal chalcogenides. *Inorg. Chem. Front.* **2016,** *3* (4), 452-463.
3. Hirsch, A.; Hauke, F., Post Graphene 2D Chemistry: The Emerging Field of Molybdenum Disulfide and Black Phosphorus Functionalization. *Angewandte Chemie International Edition*, n/a-n/a.
4. Mahler, B.; Hoepfner, V.; Liao, K.; Ozin, G. A., Colloidal Synthesis of 1T-WS2 and 2H-WS2 Nanosheets: Applications for Photocatalytic Hydrogen Evolution. *Journal of the American Chemical Society* **2014,** *136* (40), 14121-14127.
5. Benck, J. D.; Hellstern, T. R.; Kibsgaard, J.; Chakthranont, P.; Jaramillo, T. F., Catalyzing the Hydrogen Evolution Reaction (HER) with Molybdenum Sulfide Nanomaterials. *ACS Catalysis* **2014,** *4* (11), 3957-3971.
6. Lukowski, M. a.; Daniel, A. S.; English, C. R.; Meng, F.; Forticaux, A.; Hamers, R. J.; Jin, S., Highly active hydrogen evolution catalysis from metallic WS_2 nanosheets. *Energy and Environmental Science* **2014,** *7* (8), 2608-2613.
7. Lukowski, M. a.; Daniel, A. S.; Meng, F.; Forticaux, A.; Li, L.; Jin, S., Enhanced hydrogen evolution catalysis from chemically exfoliated metallic MoS_2 nanosheets. *Journal of the American Chemical Society* **2013,** *135* (28), 10274-10277.
8. Seo, B.; Jeong, H. Y.; Hong, S. Y.; Zak, A.; Joo, S. H., Impact of a conductive oxide core in tungsten sulfide-based nanostructures on the hydrogen evolution reaction. *Chem. Comm.* **2015,** *51*, 8334-8337.
9. Tsai, C.; Chan, K.; Abild-Pedersen, F.; Norskov, J. K., Active edge sites in MoSe2 and WSe2 catalysts for the hydrogen evolution reaction: a density functional study. *Phys Chem Chem Phys* **2014,** *16* (26), 13156-64.
10. Velazquez, J. M.; Saadi, F. H.; Pieterick, A. P.; Spurgeon, J. M.; Soriaga, M. P.; Brunschwig, B. S.; Lewis, N. S., Synthesis and hydrogen-evolution activity of tungsten selenide thin films deposited on tungsten foils. *Journal of Electroanalytical Chemistry* **2014,** *716*, 45-48.
11. Voiry, D.; Salehi, M.; Silva, R.; Fujita, T.; Chen, M.; Asefa, T.; Shenoy, V. B.; Eda, G.; Chhowalla, M., Conducting MoS_2 nanosheets as catalysts for hydrogen evolution reaction. *Nano Lett* **2013,** *13* (12), 6222-6227.
12. Wang, H.; Kong, D.; Johanes, P.; Cha, J. J.; Zheng, G.; Yan, K.; Liu, N.; Cui, Y., MoSe2 and WSe2 nanofilms with vertically aligned molecular layers on curved and rough surfaces. *Nano Letters* **2013,** *13* (7), 3426–3433.
13. Merki, D.; Fierro, S.; Vrubel, H.; Hu, X., Amorphous molybdenum sulfide films as catalysts for electrochemical hydrogen production in water. *Chemical Science* **2011,** *2* (7), 1262-1267.
14. Merki, D.; Hu, X., Recent developments of molybdenum and tungsten sulfides as hydrogen evolution catalysts. *Energy & Environmental Science* **2011,** *4* (10), 3878-3888.
15. Yang, J.; Shin, H. S., Recent advances in layered transition metal dichalcogenides for hydrogen evolution reaction. *Journal of Materials Chemistry A* **2014,** *2* (17), 5979-5985.
16. Yu, Y.; Huang, S.-Y.; Li, Y.; Steinmann, S. N.; Yang, W.; Cao, L., Layer-dependent electrocatalysis of MoS_2 for hydrogen evolution. *Nano letters* **2014,** *14* (2), 553-558.

17. Vrubel, H.; Moehl, T.; Gratzel, M.; Hu, X., Revealing and accelerating slow electron transport in amorphous molybdenum sulphide particles for hydrogen evolution reaction. *Chemical Communications* **2013,** *49* (79), 8985-8987.
18. Yu, Y.; Li, G.; Huang, L.; Barrette, A.; Cai, Y.-Q.; Yu, Y.; Gundogdu, K.; Zhang, Y.-W.; Cao, L., Enhancing Multifunctionalities of Transition-Metal Dichalcogenide Monolayers via Cation Intercalation. *ACS Nano* **2017,** *11* (9), 9390-9396.
19. Li, G.; Zhang, D.; Yu, Y.; Huang, S.; Yang, W.; Cao, L., Activating MoS_2 for pH-Universal Hydrogen Evolution Catalysis. *Journal of the American Chemical Society* **2017**.
20. Jaramillo, T. F.; Jørgensen, K. P.; Bonde, J.; Nielsen, J. H.; Horch, S.; Chorkendorff, I., Identification of active edge sites for electrochemical H_2 evolution from MoS_2 nanocatalysts. *science* **2007,** *317* (5834), 100-102.
21. Benck, J. D.; Chen, Z.; Kuritzky, L. Y.; Forman, A. J.; Jaramillo, T. F., Amorphous Molybdenum Sulfide Catalysts for Electrochemical Hydrogen Production: Insights into the Origin of their Catalytic Activity. *ACS Catalysis* **2012,** *2* (9), 1916-1923.
22. Li, Y.; Wang, H.; Xie, L.; Liang, Y.; Hong, G.; Dai, H., MoS_2 Nanoparticles Grown on Graphene: An Advanced Catalyst for the Hydrogen Evolution Reaction. *Journal of the American Chemical Society* **2011,** *133* (19), 7296-7299.
23. Wang, H.; Kong, D.; Johanes, P.; Cha, J. J.; Zheng, G.; Yan, K.; Liu, N.; Cui, Y., $MoSe_2$ and WSe_2 Nanofilms with Vertically Aligned Molecular Layers on Curved and Rough Surfaces. *Nano Letters* **2013,** *13* (7), 3426-3433.
24. Kong, D.; Wang, H.; Cha, J. J.; Pasta, M.; Koski, K. J.; Yao, J.; Cui, Y., Synthesis of MoS_2 and $MoSe_2$ Films with Vertically Aligned Layers. *Nano Letters* **2013,** *13* (3), 1341-1347.
25. Wang, H.; Lu, Z.; Kong, D.; Sun, J.; Hymel, T. M.; Cui, Y., Electrochemical Tuning of MoS_2 Nanoparticles on Three-Dimensional Substrate for Efficient Hydrogen Evolution. *ACS Nano* **2014,** *8* (5), 4940-4947.
26. Ambrosi, A.; Sofer, Z.; Pumera, M., Lithium intercalation compound dramatically influences the electrochemical properties of exfoliated MoS_2. *Small* **2015,** *11* (5), 605-612.
27. Voiry, D.; Yamaguchi, H.; Li, J.; Silva, R.; Alves, D. C. B.; Fujita, T.; Chen, M.; Asefa, T.; Shenoy, V. B.; Eda, G.; Chhowalla, M., Enhanced catalytic activity in strained chemically exfoliated WS_2 nanosheets for hydrogen evolution. *Nat Mater* **2013,** *12* (9), 850-855.
28. Voiry, D.; Salehi, M.; Silva, R.; Fujita, T.; Chen, M.; Asefa, T.; Shenoy, V. B.; Eda, G.; Chhowalla, M., Conducting MoS_2 Nanosheets as Catalysts for Hydrogen Evolution Reaction. *Nano Letters* **2013,** *13* (12), 6222-6227.
29. Gao, M.-R.; Chan, M. K.; Sun, Y., Edge-terminated molybdenum disulfide with a 9.4-Å interlayer spacing for electrochemical hydrogen production. *Nature communications* **2015,** *6*, 7493.
30. Deshpande, M.; Patel, P.; Vashi, M. N.; Agarwal, M. K., Effect of intercalating indium in WSe_2 single crystals. *Journal of Crystal Growth* **1999,** *197* (4), 833-840.
31. Deshpande, M. P.; Parmar, M. N.; Pandya, N. N.; Chaki, S.; Bhatt, S. V., Studies on transport properties of copper doped tungsten diselenide single crystals. *Physica B: Condensed Matter* **2012,** *407* (4), 808-812.
32. Schellenberger, A.; Jaegermann, W.; Pettenkofer, C.; Kamaratos, M.; Papageorgopoulos, C. A., Li Insertion in 2H-WS_2: Electronic Structure and Reactivity. *Berichte der Bunsen-Gesellschaft fur Physikalische Chemie* **1994,** *98* (6), 833-841.
33. Schellenberger, A.; Jaegermann, W.; Pettenkofer, C.; Papageorgopoulos, C. A.; Kamaratos, M., Alkali Intercalation into Layered Compounds: UHV in-situ preparation and reactivity. *Berichte der Bunsen-Gesellschaft fur Physikalische Chemie* **1992,** *96* (11), 1755-1761.
34. Chen, Z.; Leng, K.; Zhao, X.; Malkhandi, S.; Tang, W.; Tian, B.; Dong, L.; Zheng, L.; Lin, M.; Yeo, B. S.; Loh, K. P., Interface confined hydrogen evolution reaction in zero valent metal nanoparticles-intercalated molybdenum disulfide. *Nat Commun* **2017,** *8*, 14548.
35. Powell, A. V., Chapter 7. Intercalation compounds of low-dimensional transition metal chalcogenides. *Annual Reports Section "C" (Physical Chemistry)* **1993,** *90* (7), 177-213.
36. Voiry, D.; Mohite, A.; Chhowalla, M., Phase engineering of transition metal dichalcogenides. *Chem Soc Rev* **2015,** *44* (9), 2702-12.
37. Zeng, Z.; Yin, Z.; Huang, X.; Li, H.; He, Q.; Lu, G.; Boey, F.; Zhang, H., Single-Layer Semiconducting Nanosheets: High-yield preparation and device fabrication. *Angewandte Chemie International Edition* **2011,** *50* (47), 11093-11097.

38. Besenhard, J.; Meyer, H.; Schöllhorn, R., Defined Intercalation Stages from Cathodic Reduction of MoS2 in Organic Electrolytes. *Zeitschrift für Naturforschung B* **1976,** *31* (7), 907-911.
39. Zheng, J.; Zhang, H.; Dong, S.; Liu, Y.; Nai, C. T.; Shin, H. S.; Jeong, H. Y.; Liu, B.; Loh, K. P., High yield exfoliation of two-dimensional chalcogenides using sodium naphthalenide. *Nature communications* **2014,** *5*, 2995.
40. Henckel, D. A.; Lenz, O.; Cossairt, B. M., Effect of Ligand Coverage on Hydrogen Evolution Catalyzed by Colloidal WSe2. *ACS Catalysis* **2017,** *7* (4), 2815-2820.
41. Brock, S. L.; Mayer, J. M., Oxygen atom transfer from a phosphine oxide to tungsten(II) compounds. *Inorganic Chemistry* **1991,** *30* (9), 2138-2143.
42. Jimtaisong, A.; Luck, R. L., Synthesis and Catalytic Epoxidation Activity with TBHP and H_2O_2 of Dioxo-, Oxoperoxo-, and Oxodiperoxo Molybdenum(VI) and Tungsten(VI) Compounds Containing Monodentate or Bidentate Phosphine Oxide Ligands: Crystal Structures of $WCl_2(O)_2(OPMePh_2)_2$, $WCl_2(O)(O_2)(OPMePh_2)_2$, $MoCl_2(O)_2dppmO_2{\cdot}C_4H_{10}O$, $WCl_2(O)_2dppmO_2$, $Mo(O)(O_2)_2dppmO_2$, and $W(O)(O_2)_2dppmO_2$. *Inorganic Chemistry* **2006,** *45* (25), 10391-10402.
43. Hildebrand, A.; Lonnecke, P.; Silaghi-Dumitrescu, L.; Hey-Hawkins, E., Tungsten phosphanylarylthiolato complexes $[W\{PhP(_2\text{-}SC_6H_4)_2\text{-}\kappa^3\,S,S',P\}_2]$ and $[W\{P(2\text{-}SC_6H_4)_3\text{-}\kappa^4\,S,S',S'',P\}_2]$: Synthesis, structures and redox chemistry. *Dalton Transactions* **2008,** (34), 4639-4646.
44. Crich, D.; Dyker, H., Dichotomous reaction pathways in the reaction of triarylphosphine oxides with meerwein's salt. *Tetrahedron Letters* **1989,** *30* (4), 475-476.
45. Makara, V. a.; Babich, N. G.; Zakharenko, N. I.; Pasechny, V. a.; Surzhko, V. F.; Kulikov, L. M.; Antonova, M. M.; Chekhovsky, a. a.; Romakai, L. P., Hydrogen Intercalates of Low-Dimensional Dichalcogenides. *International Journal of Hydrogen Energy* **1997,** *22* (2/3), 233-23
46. Dobrovolsky, V.; Kopylova, E. I.; Kulikov, L. M.; Semjonov-Kobzar, A. A.; Solonin, Y. M.; Askelrud, L. G., X-ray spectroscopy investigation of hydrogen-containing phases based on the compounds of tungsten with VI group elements. *International Journal of Hydrogen Energy* **2001,** *26* (5), 477-481.
47. Zhu, Z.; Peelaers, H.; Van de Walle, C. G., Hydrogen intercalation in MoS_2. *Physical Review B* **2016,** *94* (8).
48. Borghols, W. J. H.; Wagemaker, M.; Lafont, U.; Kelder, E. M.; Mulder, F. M., Size Effects in the $Li_{4+x}Ti_5O_{12}$ Spinel. *Journal of the American Chemical Society* **2009,** *131* (49), 17786-17792.
49. Zhang, R.; Tsai, I. L.; Chapman, J.; Khestanova, E.; Waters, J.; Grigorieva, I. V., Superconductivity in Potassium-Doped Metallic Polymorphs of MoS_2. *Nano Lett* **2016,** *16* (1), 629-36.
50. Leng, K.; Chen, Z.; Zhao, X.; Tang, W.; Tian, B.; Nai, C. T.; Zhou, W.; Loh, K. P., Phase Restructuring in Transition Metal Dichalcogenides for Highly Stable Energy Storage. *ACS Nano* **2016**.
51. Kopnov, F.; Feldman, Y.; Popovitz-Biro, R.; Vilan, A.; Cohen, H.; Zak, A.; Tenne, R., Intercalation of Alkali Meteral in WS_2 Nanoparticles, Revisited. *Chem. Mater.* **2008,** *20*, 4099-4105.
52. Acerce, M.; Voiry, D.; Chhowalla, M., Metallic 1T phase MoS_2 nanosheets as supercapacitor electrode materials.*Nature Nanotechnology* **2015,** *10* (4), 313-318.
53. Zak, A.; Feldman, Y.; Lyakhovitskaya, V.; Leitus, G.; Popovitz-Biro, R.; Wachtel, E.; Cohen, H.; Reich, S.; Tenne, R., Alkali Metal Intercalated Fullerene-Like MS_2 (M = W, Mo) Nanoparticles and Their Properties. *Journal of the American Chemical Society* **2002,** *124* (17), 4747-4758.
54. A. Schellenberger, R. S., T. Mayer, E. Holub-Krappe, C. Pettenkofer, W. Jaegermann, U.A. Ditzinger, H. Neddermeyer, Na adsorption on the layer semiconductors SnS_2 and WSe_2. *Surface Science Letters* **1991,** *241*, L25-L29.
55. Papageorgopoulos, C. A.; Jaegermann, W., Li intercalation across and along the van der Waals surfaces of MoS_2(0001). *Surface Science* **1995,** *338* (1-3), 83-93.
56. Wang, X.; Shen, X.; Wang, Z.; Yu, R.; Chen, L., Atomic-Scale Clarification of Structural Transition of MoS_2 upon Sodium Intercalation. *ACS Nano* **2014,** *8* (11), 11394-11400.
57. Hinnemann, B.; Moses, P. G.; Bonde, J.; Jørgensen, K. P.; Nielsen, J. H.; Horch, S.; Chorkendorff, I.; Nørskov, J. K., Biomimetic Hydrogen Evolution: MoS_2 Nanoparticles as Catalyst for Hydrogen Evolution. *Journal of the American Chemical Society* **2005,** *127* (15), 5308-5309.
58. Trasatti, S., Work function, electronegativity, and electrochemical behaviour of metals: III. Electrolytic hydrogen evolution in acid solutions. *Journal of Electroanalytical Chemistry and Interfacial Electrochemistry* **1972,** *39* (1), 163-184.

59. Tsai, C.; Chan, K.; Abild-Pedersen, F.; Norskov, J. K., Active edge sites in $MoSe_2$ and WSe_2 catalysts for the hydrogen evolution reaction: a density functional study. *Physical Chemistry Chemical Physics* **2014,** *16* (26), 13156-13164.
60. Yu, Y.; Huang, S. Y.; Li, Y.; Steinmann, S. N.; Yang, W.; Cao, L., Layer-dependent electrocatalysis of MoS_2 for hydrogen evolution. *Nano Lett* **2014,** *14* (2), 553-8.
61. Zoski, C. G., *Handbook of Electrochemistry*. Elsevier: Amsterdam, 2007.
62. Bueno, P. R.; Benites, T. A.; Góes, M. S.; Davis, J. J., A Facile Measurement of Heterogeneous Electron Transfer Kinetics. *Analytical Chemistry* **2013,** *85* (22), 10920-10926.
63. Wilson, J.; Yoffe, A., The transition metal dichalcogenides discussion and interpretation of the observed optical, electrical and structural properties. *Advances in Physics* **1969,** *18* (73), 193-335.
64. Friend, R. H.; Yoffe, A. D., Electronic properties of intercalation complexes of the transition metal dichalcogenides. *Advances in Physics* **1987,** *36* (1), 1-94.
65. Zou, M.; Chen, J.; Xiao, L.; Zhu, H.; Yang, T.; Zhang, M.; Du, M., WSe_2 and $W(Se_xS_{1-x})_2$ nanoflakes grown on carbon nanofibers for the electrocatalytic hydrogen evolution reaction. *Journal of Materials Chemistry A* **2015,** *3* (35), 18090-18097.
66. Kim, H.; Hong, J.; Park, K.-Y.; Kim, H.; Kim, S.-W.; Kang, K., Aqueous rechargeable Li and Na ion batteries. *Chemical Reviews* **2014,** *114* (23), 11788-11827.
67. Yu, H.; Liu, Y.; Brock, S. L., Synthesis of discrete and dispersible MoS_2 nanocrystals. *Inorganic chemistry* **2008,** *47* (5), 1428-1434.
68. Pu, C.; Zhou, J.; Lai, R.; Niu, Y.; Nan, W.; Peng, X., Highly reactive, flexible yet green Se precursor for metal selenide nanocrystals: Se-octadecene suspension (Se-SUS). *Nano research* **2013,** *6* (9), 652-670.
69. Bard, A. J.; Faulkner, L. R.; Leddy, J.; Zoski, C. G., *Electrochemical methods: fundamentals and applications*. wiley New York: 1980; Vol. 2.
70. Gerhardt, G.; Adams, R. N., Determination of diffusion coefficients by flow injection analysis. *Analytical chemistry* **1982,** *54* (14), 2618-2620.